Z-Shaped Polycyclic Aromatic Hydrocarbons with Embedded Five-Membered Rings and their Application in Organic Thin-Film Transistors

Sven M. Elbert,[a] Evelin Bolgert,[a] Owen T. A. Paine,[a] Farhad Ghalami,[b] Wen-Shan Zhang,[a] Ute Zschieschang,[c] Frank Rominger,[a] Dennis Popp,[a] Hagen Klauk,[c] Marcus Elstner,[b] Michael Mastalerz*[a]

a. Institute of Organic Chemistry, Ruprecht-Karls-University Heidelberg, Im Neuenheimer Feld 270, 69120 Heidelberg, Germany; E-mail: michael.mastalerz@oci.uni-heidelberg.de
b.   Institute of Physical Chemistry and Theoretical Chemical Chemistry, Karlsruhe Institute of Technology, Kaiserstraße 12, D-76131, Karlsruhe, Germany
c. Max Planck Institute for Solid State Research, Heisenbergstr.1, 70569 Stuttgart, Germany

Supporting Information

Table of Contents

1. General Remarks

Materials: All used reagents, solvents and materials were purchased from Acros Organics, BLDPharm, Carbolution, Fisher Scientific/Thermo Fisher, Honeywell, Sigma-Aldrich, Grüssing, Merck or VWR Chemicals and used without further purification, if not mentioned otherwise. Compounds **1**,[S1] **2**[S2] and **4**[S3-5] were synthesized according to literature known procedures Anhydrous dichloromethane (DCM), tetrahydrofuran (THF) and toluene were dispensed from the solvent purification system MB SPS-800. Solvents were degassed by bubbling argon through it for at least 15 min. If not mentioned otherwise, all reactions were performed under standard conditions (25 °C, 1013 mbar).

Thin layer and flash column chromatography: Analytical thin layer chromatography was performed using fluorescent-labeled silica coated aluminum plates (TLC silica gel 60 F254, Merck). Detection was accomplished by using UV-light (λ_{Ex} = 254 nm).

For flash column chromatography silica gel with a particle size of 0.040–0.063 (Macherey-Nagel) and for coating 63–200 ppm (Sigma-Aldrich) was used. For chromatography, the following eluents were used: light petroleum ether (PE), ethyl acetate (EtOAc) and DCM or their mixtures.

Nuclear Magnetic Resonance Spectroscopy (NMR): NMR spectra were recorded using a Bruker Avance III 400 (^{1}H: 400 MHz, ^{13}C: 101 MHz), a Bruker Avance III 600 (^{1}H: 600 MHz, ^{13}C: 151 MHz) or a Bruker Avance Neo 700 (^{1}H: 700 MHz, ^{13}C: 171 MHz) spectrometer at 298 K unless otherwise stated. Abbreviations: s = singlet, d = doublet, t = triplet, quart = quartet, m = multiplet. Chemical shifts (δ) are given/expressed in parts per million (ppm) relative to traces of protonated solvent in CDCl$_3$ (δ_H = 7.26 ppm, δ_C = 77.2 ppm), THF-d_8 (δ_H = 3.58 ppm, δ_C = 65.6 ppm) or oDCB-d_4 (δ_H = 6.93 ppm, δ_C = 132.6 ppm), the coupling constants J are given in Hertz (Hz).

Melting points (M.p.): Melting points were measured using a Büchi M-565 melting point apparatus with a heating rate of 2.5 °C/min and are reported uncorrected.

Mass Spectrometry (MS): MS experiments were performed on a Bruker AutoFlex Speed time-of-flight spectrometer (MALDI-TOF-MS), DCTB (trans-2-[3-(4-*tert*-Butylphenyl)-2-methyl-propenylidene)malononitrile) was used as matrix.

Fourier-Transformation Infrared (FTIR) Spectroscopy: IR spectra were recorded using a Bruker Lumos Fourier transformation spectrometer with a Zn/Se ATR crystal. The signal intensities were described as followed: s (strong), m (medium), w (weak) and br (broad).

UV-Vis and fluorescence spectroscopy: UV-vis absorption spectra have been recorded using a Jasco V-730 spectrophotometer. Molar extinction coefficients (ε) were calculated by absorption measurements of five different concentrated solutions prepared by standard addition method. Fluorescence spectroscopy was done using a Jasco FP-8300 fluoro spectrometer and fluorescence quantum yield were determined applying direct methods[S6] using a Jasco FP-8500 Fluorescence Spectrometer with a Jasco ILF-835 (100 mm) integrating sphere. The data obtained was interpreted with Spectra Manager from Jasco.

Elemental Analysis (EA): Elemental analyses were measured in the Microanalytical Laboratory of the University of Heidelberg using an Elementar *vario MICRO cube* Element Analyzer.

Single crystal X-ray diffraction analysis: The crystal structures was measured on a Bruker APEX II (λ_{Mo}-K_α = 0.71073 Å) or a STOE Stadivari (λ_{Cu}-K_α = 1.54178 Å) diffractometer and a PILATUS detector. Data processing and absorption correction (X-Area LANA 1.83.8.0) was done by standard methods.[S7] The structures were solved with SHELXT-2014[S8] and refined using the SHELXL-2018/3[S9, 10] software.

Electrochemical Investigations: Cyclovoltammetry (CV) and Differential Pulse Voltammetry (DPV) spectra were recorded on a Metrohm Autolab PGSTAT101 potentiostat using a Pt working electrode (0.78 mm^2), a Pt counter electrode and an Ag/Ag+ pseudo reference electrode in degassed HPLC-grade CH_2Cl_2. Ferrocene was used as an internal standard for calibration. Cyclic voltammograms (CV) were obtained at a scan rate of 0.1 Vs^{-1} and differential pulse voltammograms (DPV) were obtained with a step size of 0.005 V, a modulation amplitude of 0.025 V a modulation time of 0.05 s and an interval time of 0.5 s.

GIWAXS: Grazing-Incidence Wide-Angle X-ray Scattering (GIWAXS) was performed on Rigaku SmartLab diffractometer operated at 9 kW and equipped with a HyPix-3000 detector. Visualization and data evaluation was accomplished using the Rigaku SmartLab Studio II software.

2. Synthetic Procedures
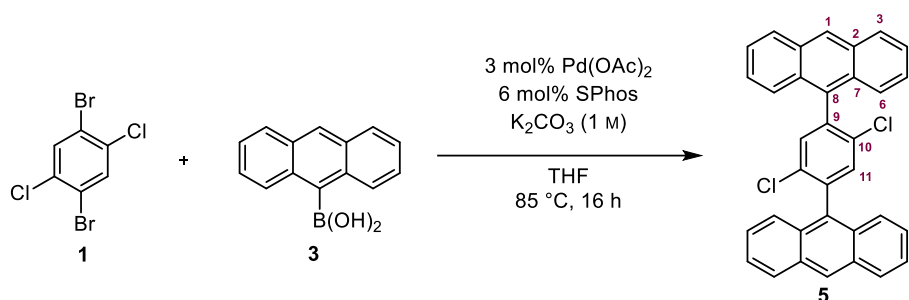
A screw-capped vial was charged with 1,4-dibromo-2,5-dichlorobenzene **1**[S1] (610 mg, 2.0 mmol) and 9-anthracene boronic acid **3** (1.78 g, 8.0 mmol) and purged with argon. Degassed tetrahydrofuran (8 mL) and a degassed aqueous K_2CO_3 solution (1 M, 8 mL) were added and the reaction mixture stirred. Pd(OAc)$_2$ (13.5 mg, 60.0 μmol, 3 mol%) and SPhos (49.3 mg, 120.0 μmol, 6 mol%) were added, the vial was sealed, and the reaction mixture vigorously stirred at 85 °C overnight. After cooling to room temperature, the orange precipitate was separated by filtration, washed with hot methanol (50 mL) and recrystallized from 1,2-dichlorobenzene (80 mL). The precipitate was isolated by filtration, rinsed with methanol and dried under airflow to give compound **5** as an off-white powder with a greenish tint in 80% yield (816 mg, 1.6 mmol).

M. p.: 380 °C (dec.).

^{1}H-NMR (400 MHz, *o*-DCB-*d*$_4$, 343 K): δ = 8.44 (s, 2H, H-1), 7.97 (d, *J* = 7.3 Hz, 4H, H-5), 7.81 (d, *J* = 8.3 Hz, 4H, H-4), 7.68 (s, 2H, H-11), 7.42-7.37 (m, 8H, H-3, 6). ppm.

^{13}C-NMR (101 MHz, *o*-DCB-*d*$_4$, 343 K): δ =134.3 (C$_{quart}$), 134.0 (C-11), 131.7 (C$_{quart}$), 128.9 (C-3), 128.2 (C-1), 125.8 (C-4,5,6), 125.5 (C-4,5,6) ppm.

Note: Due to the low solubility of compound **5**, the signal-to-noise ratio does not allow further assignment, especially due to overlap with dominant solvent signals (see Figure S2).

MS (HR-MALDI$^+$): *m/z* calculated for [M]$^+$: 498.094, found: 498.087.

FTIR (neat, ATR): $\tilde{\nu}$ = 3063 (w), 3003 (w), 2957 (w), 2918 (w), 2856 (w), 1954 (w), 1718 (w), 1610 (w), 1568 (w), 1520 (w), 1485 (w), 1441 (m), 1410 (w), 1379 (m), 1327 (w), 1238 (w), 1194 (w), 1148 (w), 1122 (w), 1082 (m), 1026 (w), 960 (w), 939 (m), 901 (w), 883 (w), 847 (m), 795 (w), 770 (vs), 704 (w), 687 (w), 667 (m), 613 (w) cm^{-1}.

UV-Vis (oDCB): λ_{abs} = 335, 351, 370, 391 nm.

Emission (DCM): $\lambda_{em}(\lambda_{ex})$ = 399 (351), 418 nm
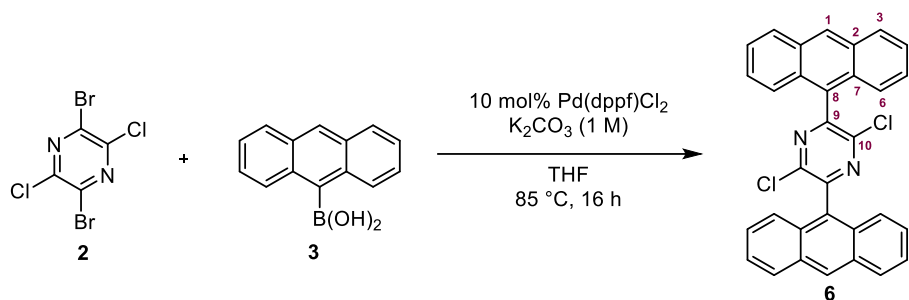
A screw-capped vial was charged with 2,5-dibromo-3,6-dichloropyrazine **2**[S2] (460 mg, 1.5 mmol) and 9-anthracene boronic acid **3** (1.33 g, 6.0 mmol) and purged with argon. Degassed tetrahydrofuran (6 mL) and a degassed aqueous solution of K_2CO_3 (1 M, 6 mL) were added and the mixture was stirred. $Pd(dppf)Cl_2$ (110 mg, 150.0 μmol, 10 mol%) was added against an argon flow, and the vial was sealed. The mixture was vigorously stirred at 85 ∘C overnight. After cooling to room temperature, the orange precipitate was isolated by filtration and washed with hot methanol (40 mL) before recrystallization from of 1,2-dichlorobenzene (45 mL). The solids were separated by filtration, rinsed with methanol, and dried under air flow to give **6** in 56% yield as a pale yellow crystalline powder (425 mg, 846.7 μmol).

M. p.: >400 °C (dec.).

1H-NMR (700 MHz, DMSO-d_6, 393 K): δ = 8.89 (s, 2H, H-1), 8.28 (d, J = 8.3 Hz, 4H, H-3), 7.81 (d, J = 8.5 Hz, 4H, H-6), 7.67 (m, 8H, H-4/5) ppm.

13C-NMR (171 MHz, DMSO-d_6, 393 K): δ = 150.7 (C-9), 147.1 (C-10), 130.3 (C-2), 129.0 (C-7), 128.7 (C-1), 128.2 (C-3), 127.5 (C-8), 126.7 (C-5), 125.0 (C-4), 124.2 (C-6) ppm.

MS (HR-MALDI⁺): m/z calculated for [M]⁺: 500.085, found: 500.121.

FTIR (neat, ATR): $\tilde{v}$ = 1622 (w), 1576(w), 1526 (w), 1506 (vw), 1431 (m), 1394 (w), 1362 (w), 1346 (w), 1286 (w), 1248 (w), 1221 (m), 1182 (w), 1159 (m), 1142 (s), 1099 (m), 1011 (m), 978 (w), 960 (w), 945 (w), 924 (m), 910 (w), 885 (m), 860 (m), 837 (w), 783 (s), 758 (m), 725 (vs), 692 (m), 669 (w), 631 (w), 609 (w) cm⁻¹.

UV-Vis (DCM): λ_{abs} (log(ε)) = 256 (5.21), 348 (3.80), 370 (4.00), 388 (4.02) nm.

Emission (DCM): $\lambda_{em}(\lambda_{ex})$ = 416 (255), 488, 530 (sh) nm

Elemental Analysis calculated for $C_{32}H_{18}Cl_2N_2 \cdot 1/2 H_2O$: C (75.30%), H (3.75%), N (5.49%), found: C (75.08%), H (3.71%), N (5.34%).
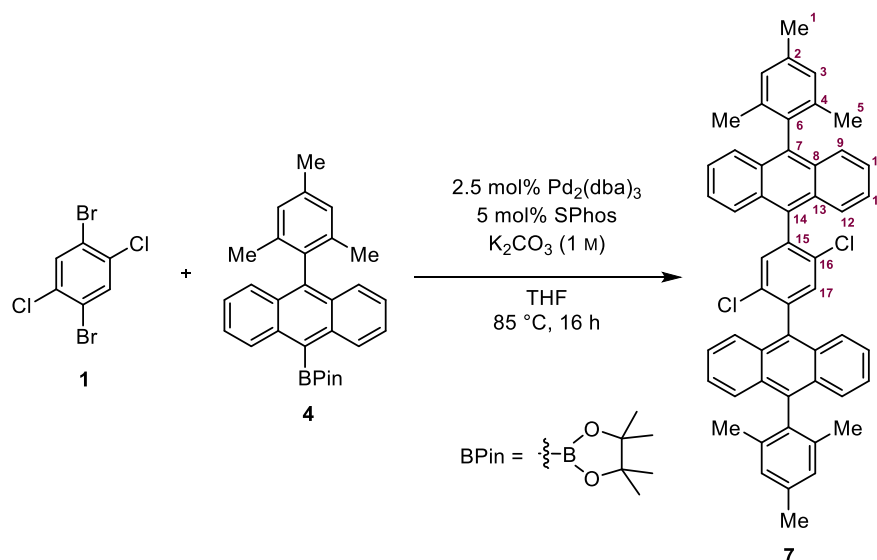
A screw-capped vial was charged with 1,4-dibromo-2,5-dichlorobenzene **1** (61.0 mg, 200 μmol), boronic acid ester **4**[S3-5] (338 mg, 800 μmol), Pd$_2$(dba)$_3$ (4.6 mg, 5.00 μmol, 2.5 mol%) and SPhos (8.2 mg, 20.0 μmol, 5 mol%) under argon atmosphere. Degassed THF (1 mL) and a degassed K$_2$CO$_3$ solution were added (aq, 1 M, 1mL) and the reaction mixture stirred at 85 °C for 16 h. After cooling to room temperature, DCM (10 mL) and water (5 mL) were added, the phases were separated, and the aqueous phase was extracted with DCM (3×5 mL). The combined organic phase was dried over MgSO$_4$, and the solvent was removed *in vacuo*. The crude product was washed with MeOH (20 mL) and filtered through a short plug of silica gel (5 cm) eluting with light petroleum ether first followed by a wash down of the product with DCM and a solvent removal under reduced pressure. The product was suspended in hot n-pentane (60 mL), filtered and dried on a Kugelrohr oven (150 °C, 3.2×10^{-2} mbar) overnight to give **7** in 34% yield as colorless powder (51.0 mg, 69.3 μmol).

M.p.: 385-388 °C (dec.).

¹H NMR (400 MHz, 323 K, CDCl₃): δ = 7.84 (s, 2H, H-17), 7.82 (d, *J* = 8.8 Hz, 4H, H-12), 7.63 (d, *J* = 8.7 Hz, 4H, H-9), 7.58-7.52 (m, 4H, H-11), 7.45-7.38 (m, 4H, H-10), 7.15 (s, 4H, H-3), 2.50 (s, 6H, H-1), 1.84 (s, 6H, H-5), 1.81 (s, 6H, H-5) ppm.

¹³C-NMR (101 MHz, 323K, CDCl₃): δ = 139.2 (C-15), 137.7 (C-2/4), 137.5 (C-2/4), 137.4 (C-7), 137.3 (C-2/4), 134.6 (C-6), 134.1 (C-16), 133.9 (C-17), 131.8 (C-14), 129.9 (C-13), 129.6 (C-8), 128.4 (C-3), 128.3 (C-3), 126.5 (C-9), 126.2 (C-12), 126.0 (C-11), 125.4 (C-10), 21.1 (C-1), 20.0 (C-5), 19.9 (C-5) ppm.

MS (HR-MALDI⁺, DCTB): *m/z* calculated for [M]⁺: 734.251, found: 734.235.

FTIR (neat, ATR): $\tilde{v}$ = 3063 (vw), 3007 (vw), 2959 (w), 2918 (w), 2856 (vw), 615 (w), 883 (w), 1379 (m), 1082 (m), 1026 (w), 1441 (w), 939 (w), 847 (m), 770 (vs), 687 (w), 669 (w), 1610 (w) cm^{-1}.

UV-Vis (DCM): λ_{abs} (log ε) = 258 (5.11), 338 (3.83), 357 (4.08), 376 (4.33), 397 nm (4.39).

Emission (DCM, 298 K): λ_{em} (λ_{ex}) = 405 (254), 427, 452 nm.
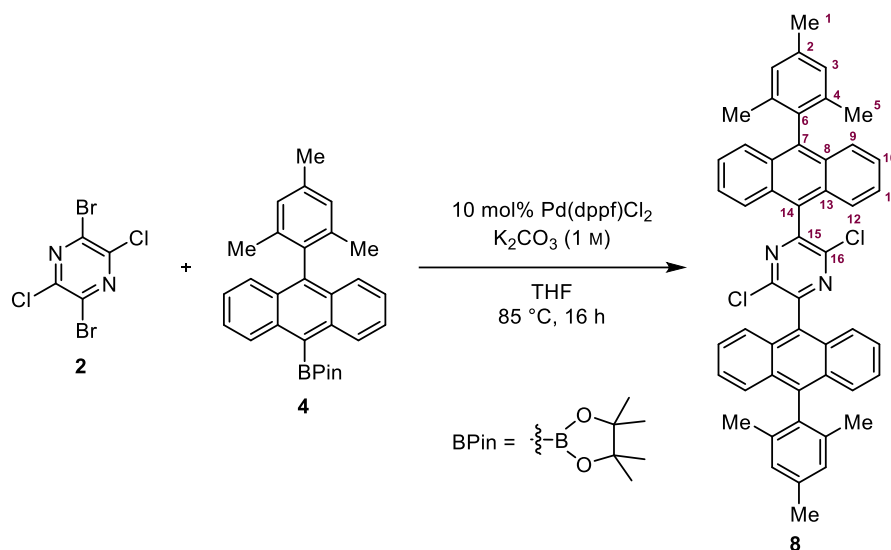
A screw-capped vial was charged with 1,4-dibromo-2,5-dichlorobenzene **2** (61.4 mg, 200 μmol) and boronic acid ester **4**[S3-5] (338 mg, 800 μmol), and purged with argon. Degassed tetrahydrofuran (1 mL) and a degassed potassium carbonate solution (1 M, 1 mL) were added and the mixture was stirred before Pd(dppf)Cl$_2$ (14.6 mg, 20 μmol, 10 mol%) was added against argon flow. The vial was sealed and stirred vigorously at 85 ∘C overnight. After cooling to room temperature, the solids formed were separated by filtration and washed with hot methanol (10 mL) before recrystallization from 1,2-dichlorobenzol (5 mL). The solids were separated by filtration, rinsed with methanol and dried under airflow to give **8** as an orange powder in 68% yield (100 mg, 136 μmol).

M.p.: 358 °C (dec.).

^{1}H NMR (400 MHz, 323 K, CDCl$_3$): δ = 7.68 (d, J = 8.1 Hz, 4H, H-12), 7.63 (d, J = 6.8 Hz, 4H, H-9), 7.60 (d, J = 16.4 Hz, 4H, H-11), 7.44 (d, J = 16.5 Hz, 4H, H-10), 7.15 (s, 4H, H-3), 2.50 (s, 6H, H-1), 1.82 (s, 12H, H-5) ppm.

^{13}C-NMR (101 MHz, 323 K, CDCl$_3$): δ = 152.6 (C-15), 149.0 (C-16), 139.5 (C-7), 137.8 (C-2/4), 137.8 (C-2/4), 137.7 (C-2, 4), 134.5 (C-6), 130.2 (C-13), 129.9 (C-8), 128.6 (C-3), 128.2 (C-14), 127.2 (C-9), 127.1 (C-9), 125.9 (C-10), 125.2 (C-12), 21.4 (C-1), 20.3 (C-5), 20.1 (C-5) ppm.

MS (HR-MALDI⁺, DCTB): *m/z* calculated for [M]⁺: 736.241, found: 736.291.

FTIR (neat, ATR): $\tilde{v}$ = 3061 (vw), 3015 (vw), 2962 (vw), 2916 (w), 2854 (vw), 1610 (w), 1564 (vw), 611 (w), 706 (w), 1290 (m), 889 (w), 760 (vs), 1107 (m), 1339 (w), 947 (m), 1022 (w), 845 (m), 1134 (m), 1269 (m), 662 (s), 1439 (w) cm^{-1}.

UV-Vis (DCM): λ_{abs} (log ε) = 255 (5.24), 355 (4.11), 374 (4.30), 396 nm (4.34).
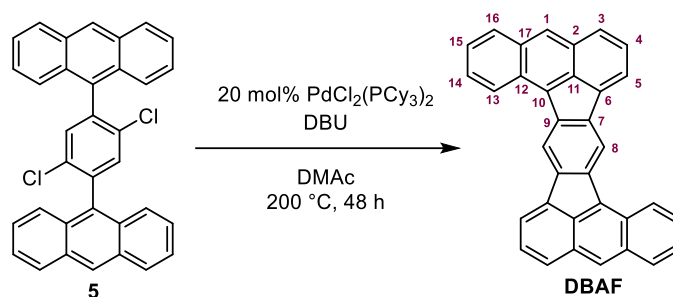
Dichloride **5** (99.9 mg, 200 µmol) and PdCl₂(PCy₃)₂ (29.5 mg, 40.0 µmol, 20 mol%) were suspended in degassed *N,N*-dimethylacetamide (DMAc) (2.5 mL) under argon atmosphere. DBU (0.48 mL, 3.22 mmol) was added dropwise to the solution and the reaction mixture was stirred for 48 h at 200 °C. After cooling the mixture to room temperature, MeOH (5 mL) was added. The suspension was filtered and the precipitate washed with MeOH (20 mL). The crude product was purified by recrystallization from *o*-DCB to give 81.9 mg (192 µmol, 96%) of **DBAF** as red crystals. For further purification **DBAF** can be sublimed at a Kugelrohr oven (<1×10^{-3} mbar, 300 °C) over several days.

M.p.: 365-368 °C (dec.).

¹H NMR (600 MHz, o-DCB-*d*₄, 323 K,): δ = 9.02 (s, 2H, H-8), 8.99 (d, *J* = 8.6 Hz, 2H, H-13), 8.32 (s, 2H, H-1), 8.10 (d, *J* = 6.6 Hz, 2H, H-5), 8.06 (d, *J* = 8.4 Hz, 2H, H-16), 7.94 (d, *J* = 8.3 Hz, 2H, H-3), 7.72-7.68 (m, 2H, H-14), 7.64 (dd, *J* = 8.3, 6.5 Hz, 2H, H-4), 7.50-7.46 (m, 2H, H-15). ppm.

¹³C-NMR (101 MHz, o-DCB-*d*₄, 323 K): δ = 139.6 (C$_{quart}$), 139.4 (C$_{quart}$), 137.6 (C$_{quart}$), 131.30 (C-16), 128.06 (C-14), 128.06 (C-1), 127.9 (C-3), 127.8 (C-4) 125.3 (C-15), 124.8 (C-13), 120.7 (C-5), 117.8 (C-8) ppm.

Note: Due to the low solubility of compound **DBAF**, the signal to noise ratio does not allow further signal assignment, especially due to overlap with dominant solvent signals (see Figure S26).

**MS (HR-MALDI⁺):** *m/z* calculated for [M]⁺: 426.141, found: 426.149.

FTIR (neat, ATR): $\tilde{v}$ = 3063 (w), 3036 (w), 1940 (vw), 1913 (w), 1892 (vw), 1855 (vw), 1799 (w), 1778 (vw), 1744 (w), 1707 (vw), 1676 (vw), 1624 (w), 1583 (w), 1526 (w), 1462 (m), 1439 (m),

1420 (m), 1375 (w), 1354 (w), 1331 (w), 1254 (w), 1217 (w), 1178 (w), 1157 (m), 1113 (w), 1078 (w), 1018 (w), 957 (w), 926 (w), 899 (w), 866 (vs), 833 (m), 798 (w), 773 (s), 744 (m), 729 (s), 708 (vs), 667 (m), 633 (w), 609 (w) cm^{-1}.

UV-Vis (DCM) λ_{abs} (log ε) = 340 (4.31), 350 (4.50), 378 (3.83), 460 (3.92), 495 (4.13), 520 (4.04), 556 (3.82, sh) nm.

Emission (DCM) λ_{em}(λ_{ex}) = 570 nm (351).

Elemental Analysis calculated for C$_{34}$H$_{18}$: C (95.86%), H (4.14%), found: C (95.70%), H (4.21%).
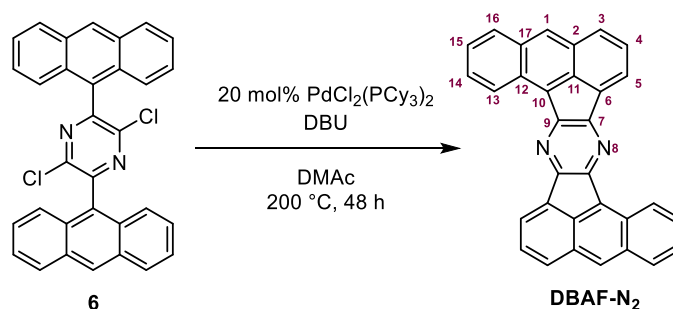
Dichloride **6** (100 mg, 200 µmol) and PdCl$_2$(PCy$_3$)$_2$ (30 mg, 40.0 µmol, 20 mol%) were suspended in degassed *N,N*-dimethylacetamide (DMAc) (2.5 mL) under argon atmosphere. DBU (0.48 mL, 3.22 mmol) was added dropwise to the solution and the reaction mixture was stirred for 48 h at 200 °C. After cooling to room temperature, MeOH (15 mL) was added to the solution and stirred until a precipitate formed. The precipitate was isolated by filtration and washed with MeOH (10 mL). The crude product was purified by recrystallization from *o*-DCB to give 47.0 mg (110 µmol, 55%) of **DBAF-N$_2$** as red crystals. For further purification **DBAF-N$_2$** can be sublimed at a Kugelrohr oven (<1×10^{-3} mbar, 300 °C) over several days.

M.p.: >400 °C.

^{1}H NMR (*o*-DCB-*d$_4$*, 700 MHz, 393 K): δ = 9.79 (d, *J* = 8.47 Hz, 2H), 8.47 (d, *J* = 6.58 Hz, 2H), 8.44 (s, 2H, H-1), 8.04 (t, *J* = 7.74 Hz, 4H), 7.72 (t, *J* = 7.46 Hz, 2H), 7.69 (t, *J* = 7.46 Hz, 2H), 7.49 (t, *J* = 7.49 Hz, 2H) ppm.

^{13}C NMR (*o*-DCB-*d$_4$*, 171 MHz, 393 K): δ = 151.9, 150.8, 134.5, 133.3, 130.6, 129.2, 127.9, 125.9, 125.5, 123.2 ppm.

Note: Due to the low solubility of compound **DBAF-N$_2$** , the signal to noise ratio does not allow further assign carbon nuclei even at 171 MHz and 10240 scans, especially due to overlap with dominant solvent signals (see Figure S32).

MS (HRMALDI+) *m/z* calculated for M+: 428.131, found: 428.219;

FTIR (neat, ATR) $\tilde{v}$ = 1454 (w), 1443 (w), 1313 (w), 1271 (m), 1259 (m), 1134 (w), 1109 (m), 1013 (w), 947 (w), 883 (w), 841 (w), 783 (m), 731 (vs), 702 (w), 677 (w), 629 (w).

UV-Vis (DCM) λ_{abs} (log ε) =375 (4.28), 400 (4.22), 468 (3.77) nm.

Emission (DCM) λ_{em}(λ_{ex}) 577 nm (374).

Elemental Analysis calculated for $C_{32}H_{16}N_2 \cdot H_2O$: C (86.28%), H (4.06%), N (6.27%), found: C (86.33%), H (3.94%), N (6.31%)
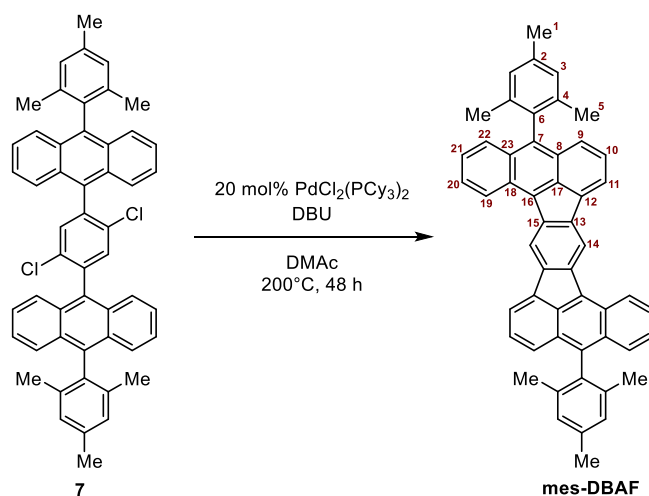
Dichloride **7** (39.8 mg, 50.0 µmol) and PdCl$_2$(PCy$_3$)$_2$ (7.4 mg, 10.0 µmol, 20 mol%) were dissolved in degassed *N,N*-dimethylacetamide (DMAc) (2 mL) under argon atmosphere. DBU (0.12 mL, 806 µmol) was added dropwise to the solution and the reaction mixture was stirred for 48 h at 200 °C. After cooling to room temperature, DCM (100 mL) was added, the phases separated and the organic phase washed with water (2×100 mL) and brine (2×100 mL) and dried over MgSO$_4$. The solvent was removed under reduced pressure. The crude product was purified by column chromatography (SiO$_2$, PE/DCM 15:1, R_f = 0.43, 0.34 (**mes-DBAF**), 0.00).and washed with warm n-pentane (60 mL). Drying on a Kugelrohr oven (150 °C, 1.5×10^{-1} mbar) over night gave **mes-DBAF** (11.0 mg, 16.6 µmol, 33%) as a red solid.

M.p.: 379-382 °C (dec.).

^{1}H NMR (400 MHz, 323 K, CDCl$_3$): δ = 9.07-9.03 (m, 4H, H-14/H-19), 8.25 (dd, *J* = 6.5, 0.7 Hz, 2H, H-11), 7.78-7.74 (m, 2H, H-20), 7.74-7.71 (m, 2H, H-22), 7.63-7.60 (m, 2H, H-10), 7.53 (d, *J* = 8.5 Hz, 2H, H-9), 7.46-7.41 (m, 2H, H-21), 7.13 (s, 4H, H-3), 2.49 (s, 6H, H-1), 1.83 (s, 12H, H-5) ppm.

^{13}C-NMR (101 MHz, 323 K, CDCl$_3$): δ = 139.2 (C$_{quart}$), 139.1 (C$_{quart}$), 138.4 (C-7), 137.8 (C$_{quart}$), 137.7 (C$_{quart}$), 137.4 (C$_{quart}$), 134.0 (C-6), 132.5 (C-23), 131.3 (C-17), 131.1 (C$_{quart}$), 129.4 (C$_{quart}$), 128.1 (C-3/22), 128.1 (C-3/22), 127.4 (C-10), 127.2 (C-20), 127.0 (C-), 126.0 (C-9), 125.1 (C-21), 124.8 (C-19), 120.1 (C-11), 117.2 (C-14), 21.1 (C-1), 20.2 (C-5) ppm.

Note: Due to overlapping signals in 2-dimensional NMR measurements, the quaternary carbon nuclei could not be further assigned.

MS (HR-MALDI$^+$, DCTB): *m/z* calculated for [M]$^+$: 662.297, found: 662.258.

IR (neat, ATR): $\tilde{v}$ = 2986 (m), 2972 (m), 2908 (m), 1462 (m), 1439 (m), 1379 (m), 1076 (s), 1030 (m), 878 (m), 852 (m), 812 (m), 781 (s), 760 (s), 712 (s), 681 (vs) cm^{-1}.

UV-Vis (DCM): λ_{abs} (log ε) = 248 (4.84), 350 (4.55), 493 (4.23), 526 (4.21), 563 (4.09) nm.

Emission (DCM, 298 K): λ_{em} (λ_{ex}) = 588 , 630 (493) nm.
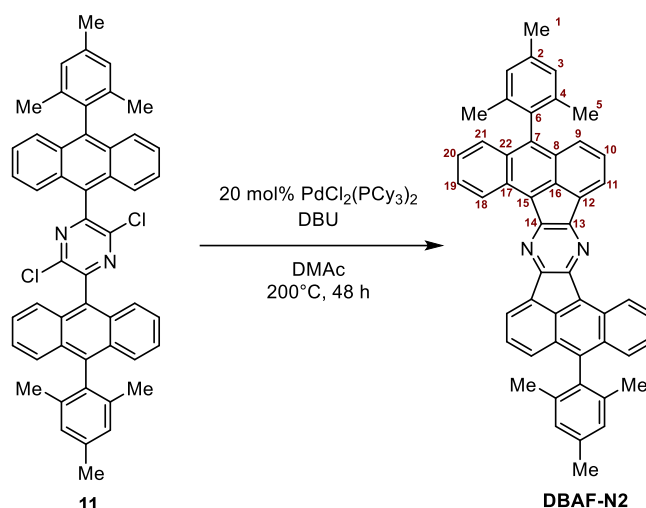
Dichloropyrazine **11** (73.7 mg, 100 µmol) and PdCl$_2$(PCy$_3$)$_2$ (14.8 mg, 20.0 µmol, 20 mol%) were dissolved in degassed *N,N*-dimethylacetamide (DMAc) (1 mL) under argon atmosphere. DBU (0.24 mL, 1.61 mmol) was added dropwise to the solution and the reaction mixture was stirred for 48 h at 200 °C. After cooling the mixture to room temperature, the solution was diluted with DCM (100 mL), washed with water (2×100 mL) and brine (2×100 mL), dried over MgSO$_4$ and the solvent was removed under reduced pressure. The crude product was purified by column chromatography (SiO$_2$, PE/EA 20:1, R_f = 0.50, 0.26 (**DBAF-N2**), 0.19, 0.00) and dried on a Kugelrohr oven (150 °C, 1.6×10^{-3} mbar) for 6 h to give **DBAF-N2** in 69% yield (45.9 mg, 69 µmol) as a red solid.

M.p.: 380 °C (dec.).

¹H NMR (THF-d₈, 600MHz, 323 K): δ = 9.85 (d, J = 8.5 Hz, 2H, H-18), 8.60 (d, J = 6.4 Hz, H-11), 7.81 (ddd, J = 8.3, 6.4, 1.1 Hz, 2H, H-19), 7.77 (dd, J = 8.6, 6.4 Hz, 2H, H-10), 7.71 (t, J = 7.9 Hz, 4H, H-21/9), 7.51 (ddd, J = 8.8, 6.4, 1.3 Hz, 2H, H-20), 7.16 (s, 4H, H-3), 2.47 (s, 6H, H-1), 1.82 (s, 12H, H-5) ppm.

¹³C NMR (THF-d₈, 151MHz, 323 K): δ = 152.0 (Cq-14/16), 151.0 (Cq-12), 141.3 (Cq-7/8/22), 137.9 (Cq-2), 137.5 (Cq-6), 133.9 (Cq-13), 133.7 (Cq-4), 132.6 (Cq-17), 130.7 (Cq-7/8/22), 130.2 (Cq-15), 128.4 (C-3), 128.4 (C-21/9), 128.3 (C-19), 128.0 (C-10), 127.4 (C-21/9), 126.7 (Cq), 126.7 (Cq), 126.4 (C-18), 126.4 (C-20), 123.2 (C-11), 20.6 (C-1), 19.7 (C-5) ppm.

MS (HR-MALDI⁺, DCTB): *m/z* calculated for [M]⁺: 664.288, found: 664.272.

IR (neat, ATR): $\tilde{v}$ = 3061 (w), 2988 (m), 2970 (m), 2914 (m), 2860 (w), 1610 (w), 1379 (m), 1433 (s), 1416 (m), 638 (m), 1171 (m), 1269 (w), 725 (vs), 1157 (s), 1128 (m), 1302 (m), 1022 (m), 986 (m), 928 (m), 849 (s), 816 (m), 781 (s), 760 (s), 1215 (m), 681 (s), 1572 (m) cm⁻¹.

UV-Vis (DCM): λ_{abs} (log ε) = 251 nm (4.83), 372 (4.50), 400 (4.52), 468 (4.06), 528 (4.01), 565 (3.88) nm.

Emission: (DCM, 298 K) λ_{em} (λ_{ex}) = 594, 642 (400) nm.

3. NMR Spectroscopy
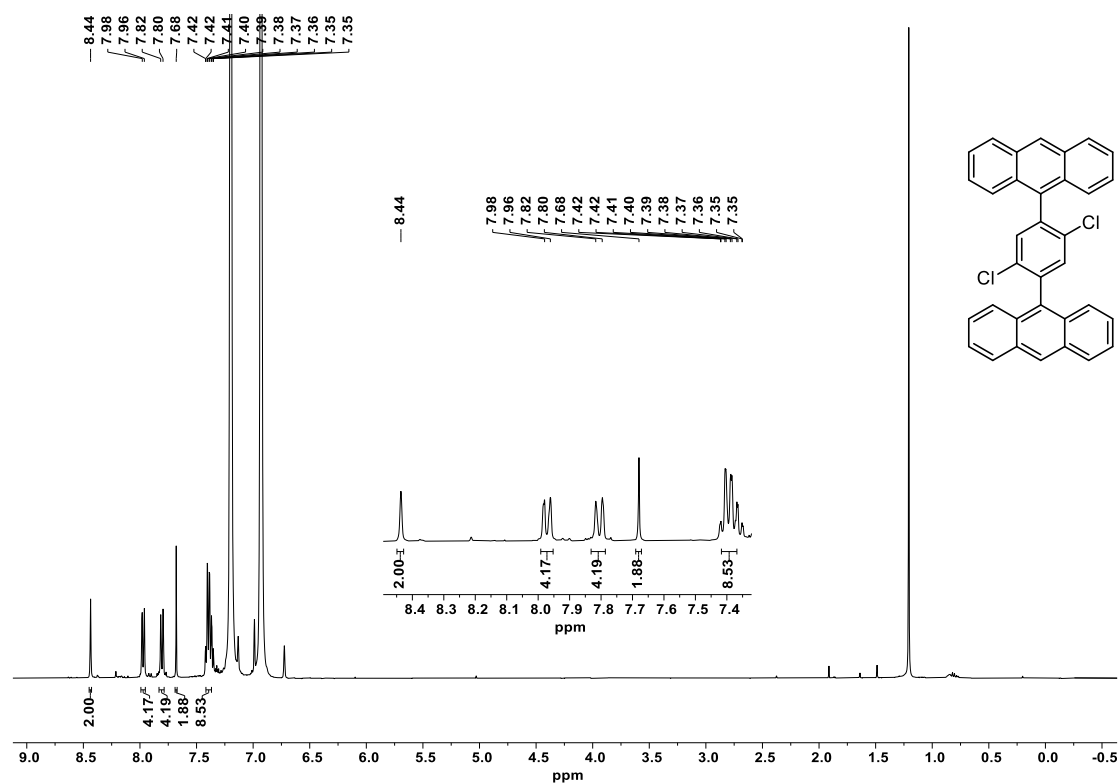
Figure S1: ^{1}H NMR spectrum of compound **5** (400 MHz, 343 K, *o*-DCB-*d*$_4$).
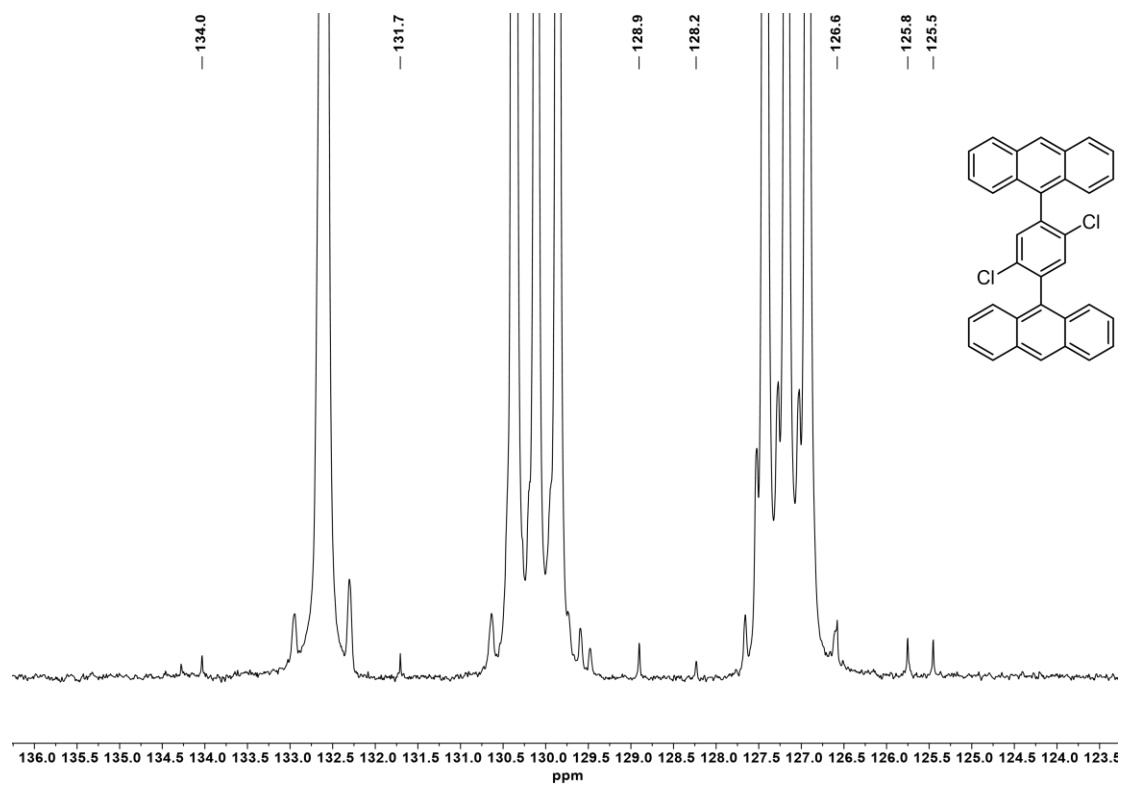
Figure S2: ^{13}C NMR spectrum of compound **5** (101 MHz, 343 K, *o*-DCB-*d*$_4$).
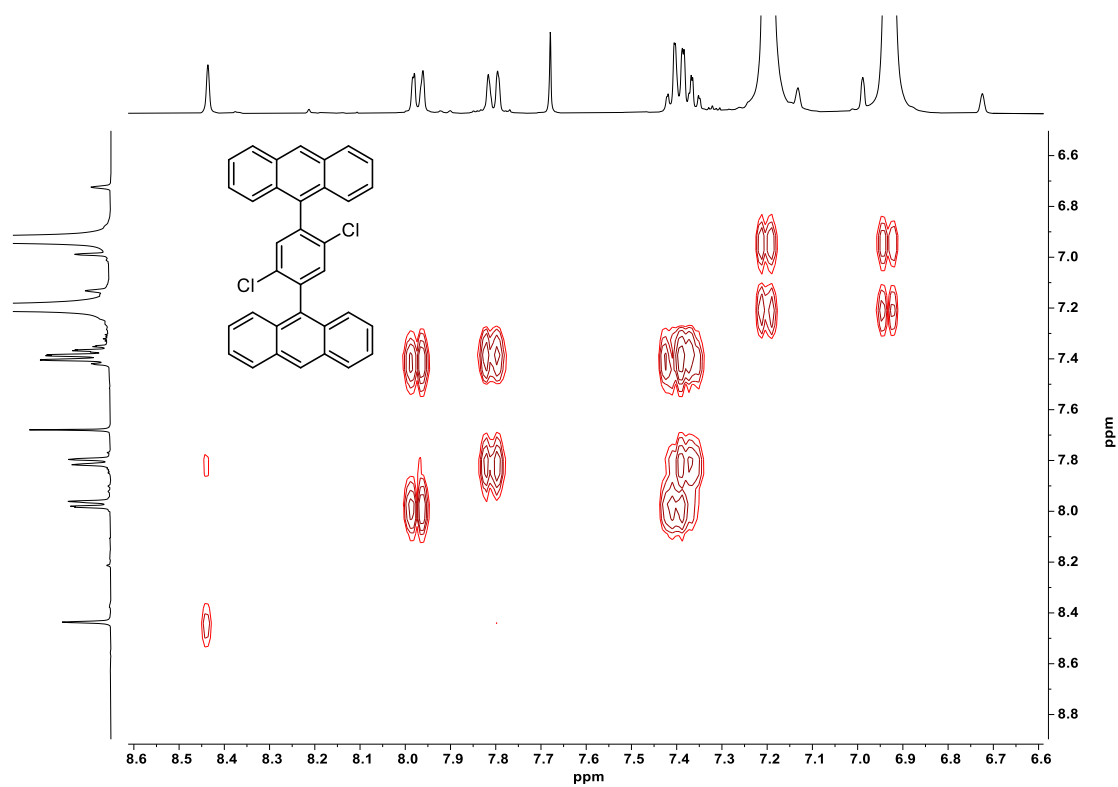
Figure S3: ^{1}H,^{1}H COSY NMR spectrum of compound **5** (400/400 MHz, 343 K, *o*-DCB-*d*$_4$).
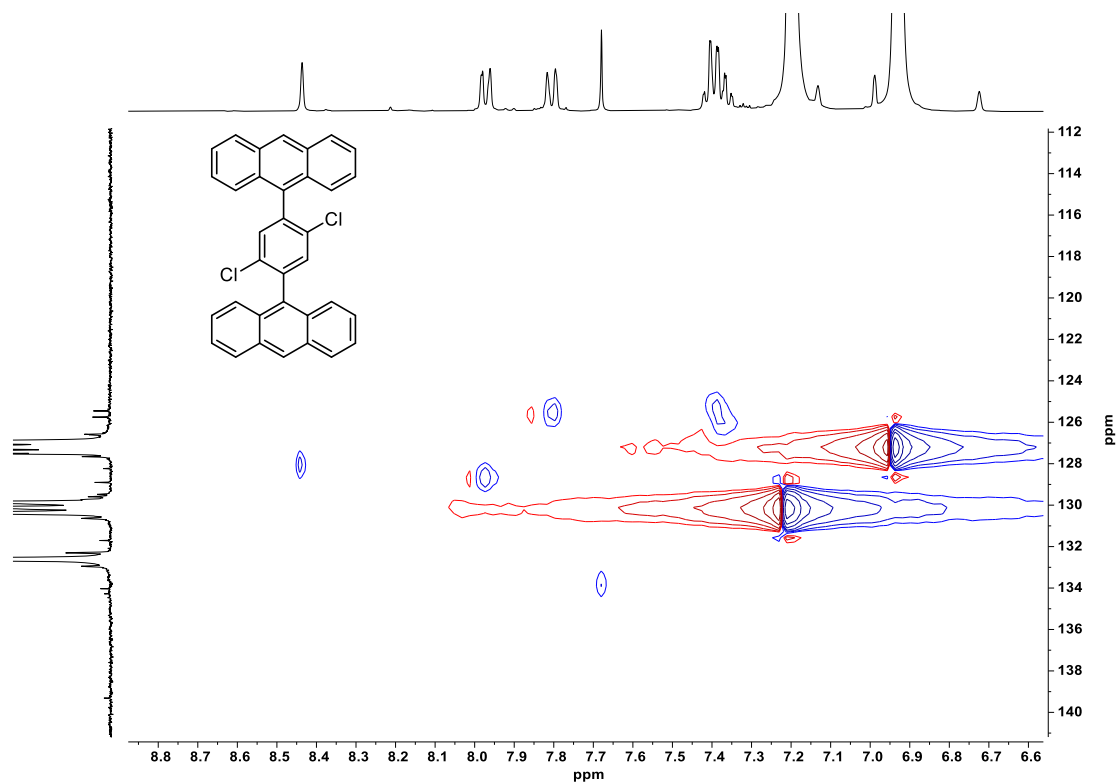
Figure S4: ^{1}H,^{13}C-HSQC NMR spectrum of compound **5** (400/101 MHz, 343 K, *o*-DCB-*d*$_4$).
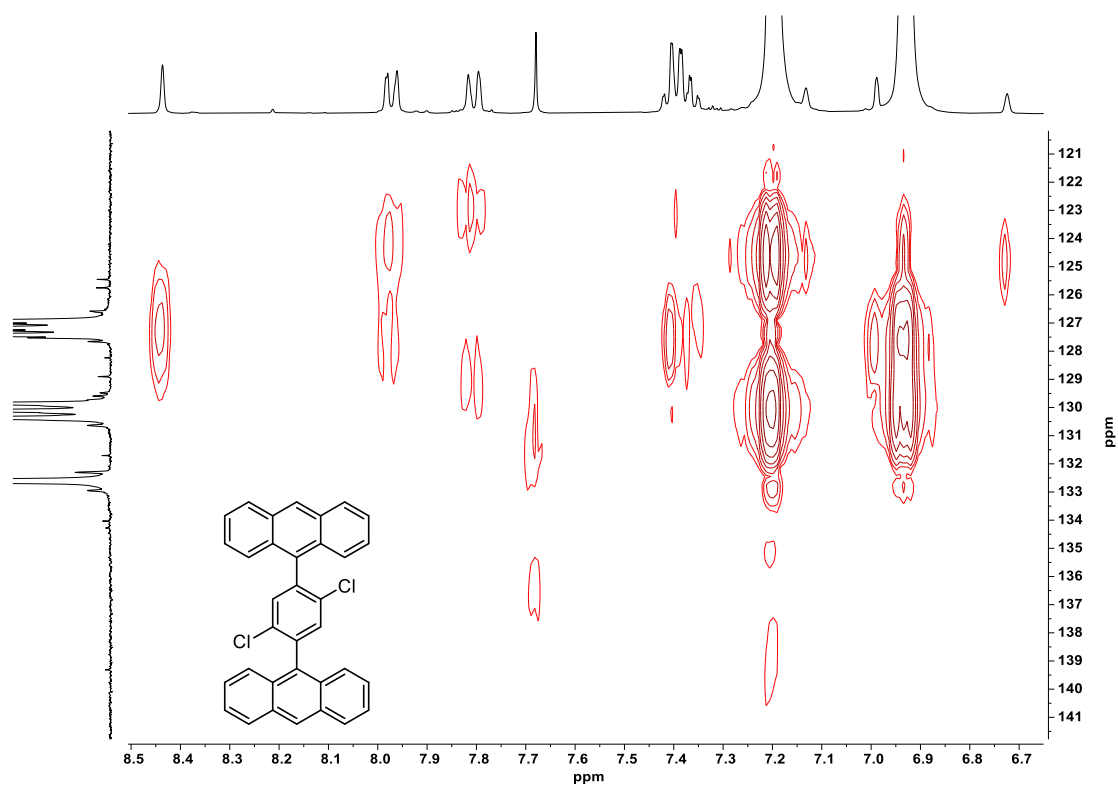
Figure S5: ^{1}H,^{13}C-HMBC NMR spectrum of compound **5** (400/101 MHz, 343 K, *o*-DCB-*d*$_4$).
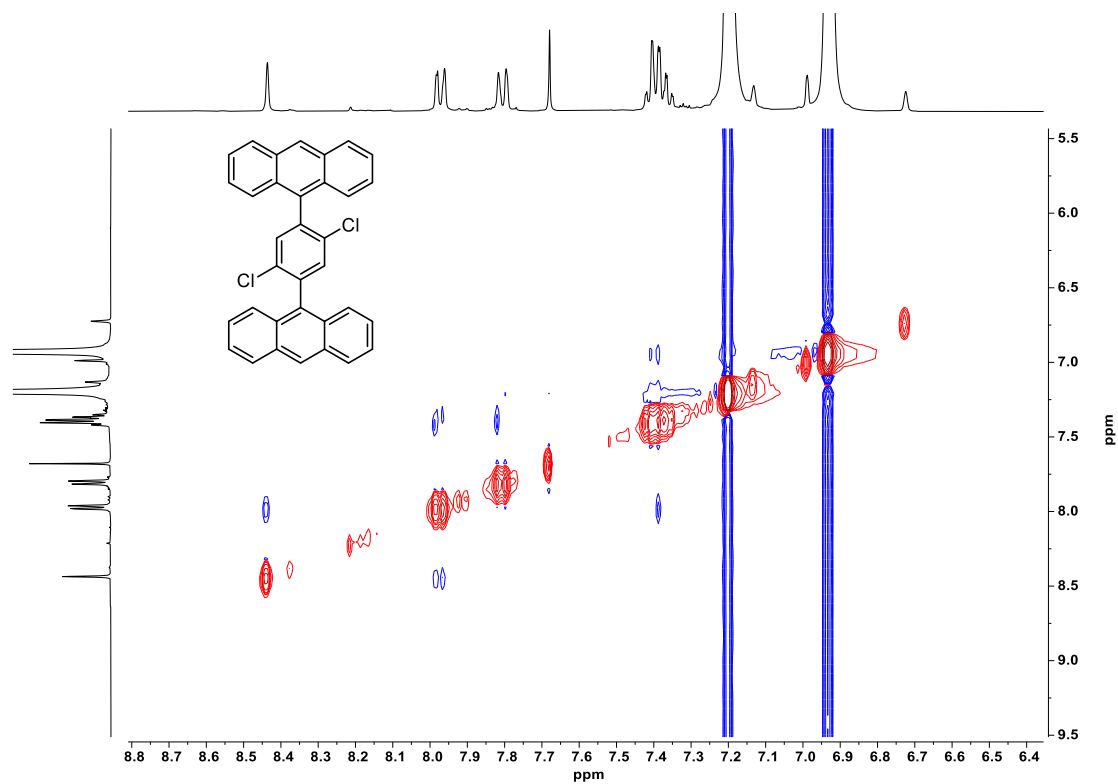
Figure S6: ^{1}H,^{1}H-NOESY NMR spectrum of compound **5** (400/400 MHz, 343 K, *o*-DCB-*d*$_4$).
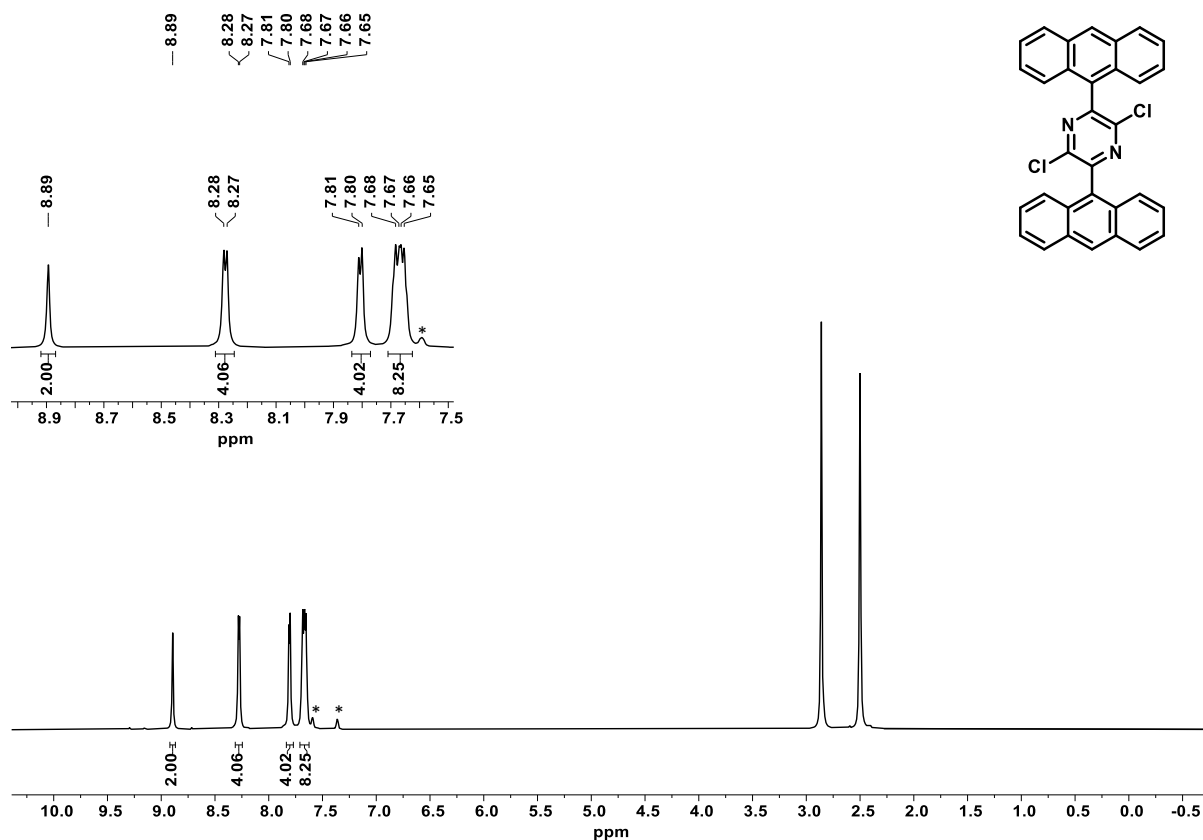
Figure S7: ^{1}H-NMR spectrum of compound **6** (700 MHz, 393 K, DMSO-d_6). The asterisks mark an unidentified impurity.
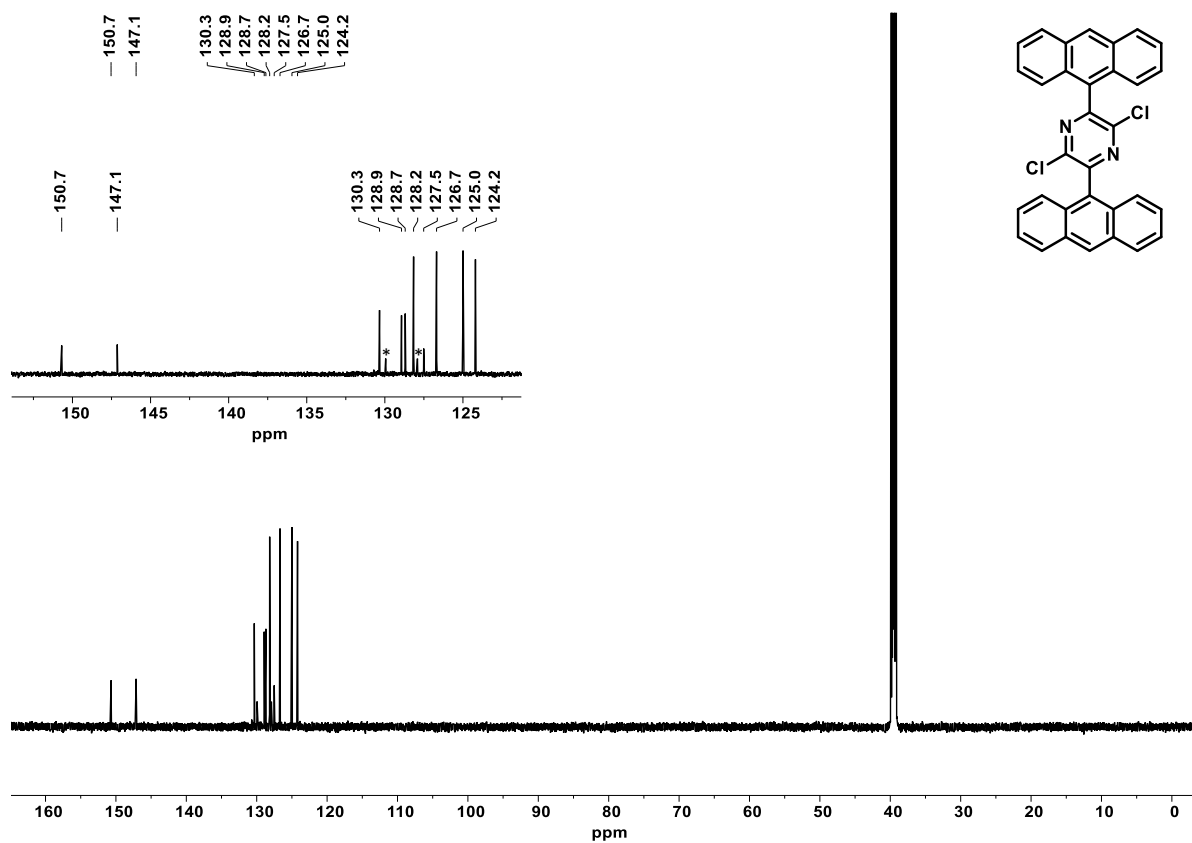
Figure S8: ^{13}C-NMR spectrum of compound **6** (171 MHz, 393 K, DMSO-d_6). The asterisks mark an unidentified impurity.

Figure S9: ^{1}H,^{1}H COSY NMR spectrum of compound **6** (700/700 MHz, 393 K, DMSO-d_6).

Figure S10: ^{1}H,^{13}C-HSQC NMR spectrum of compound **6** (700/171 MHz, 393 K, DMSO-d_6).
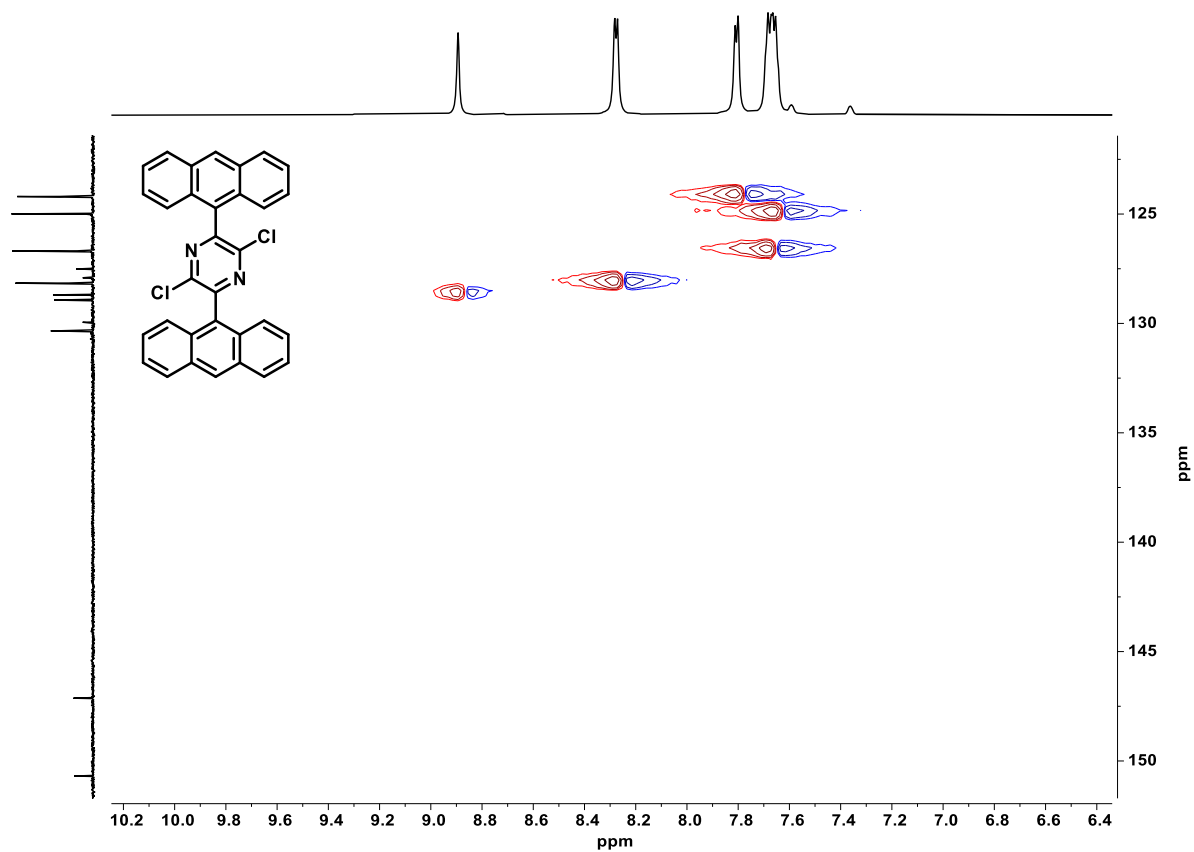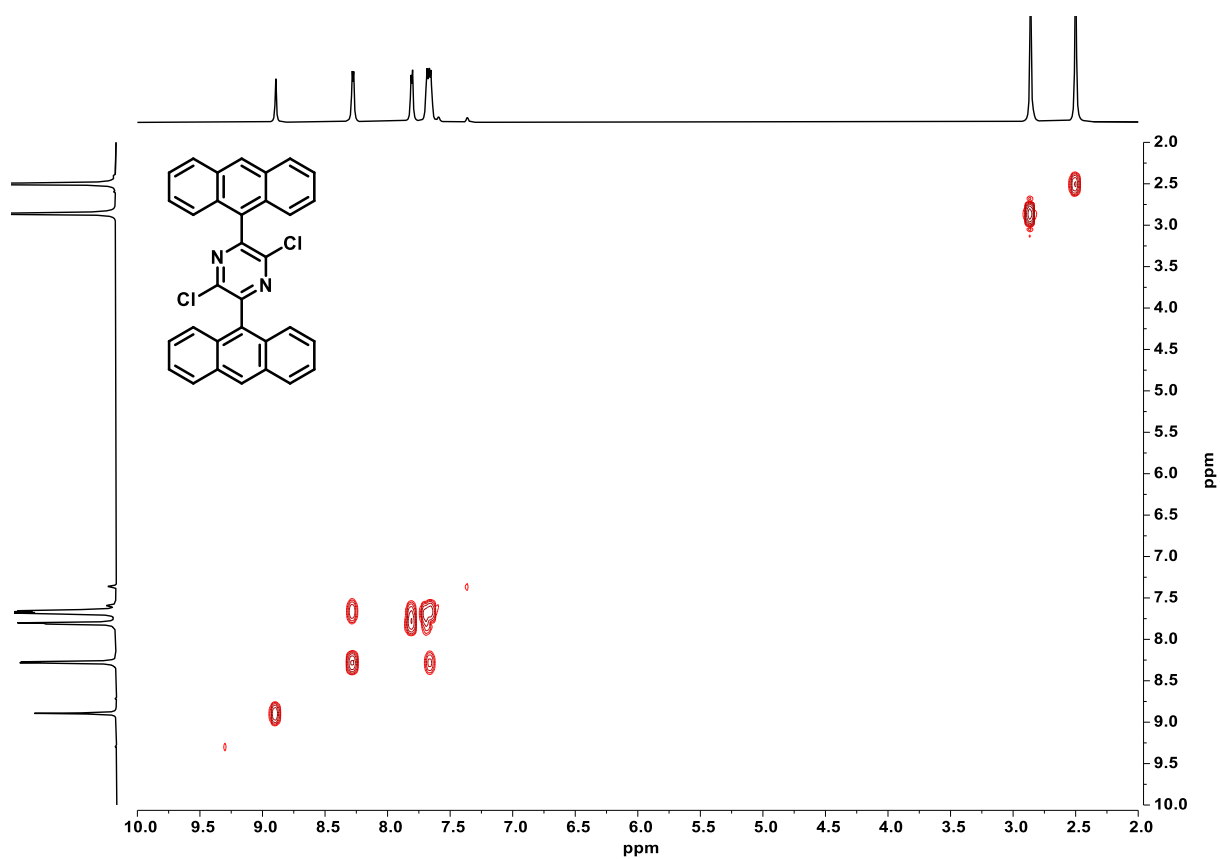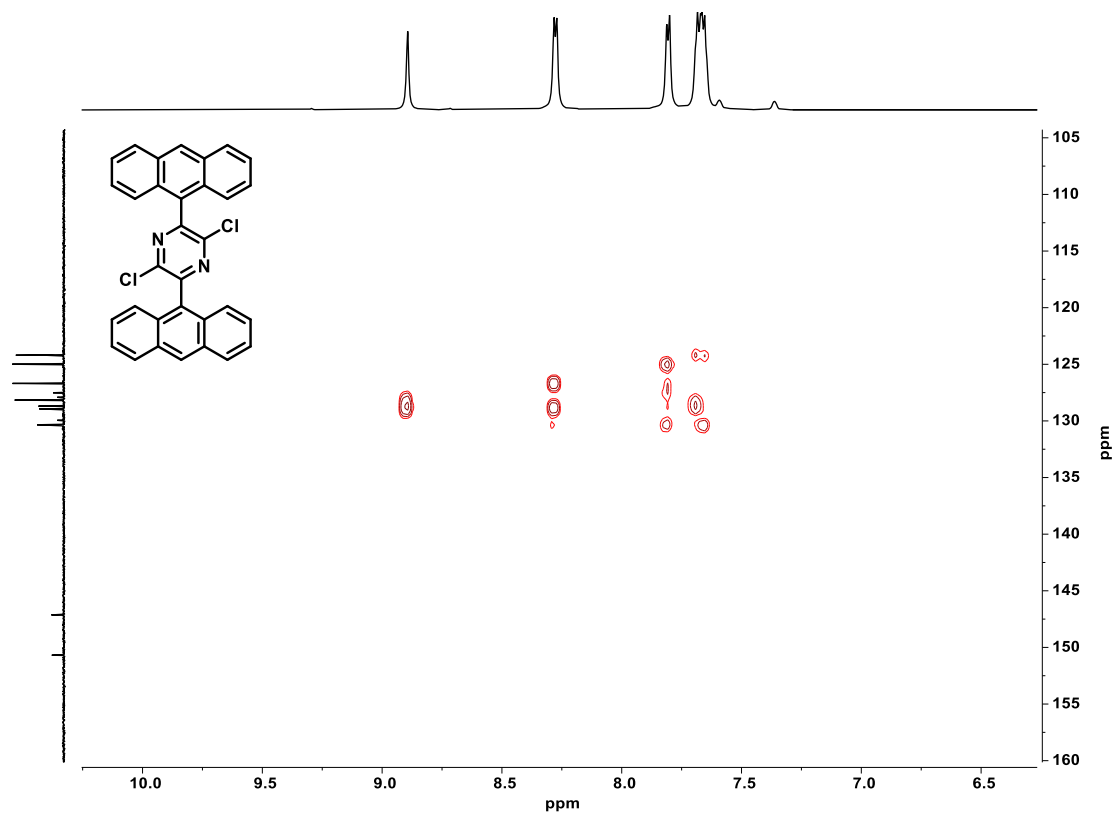
Figure S11: ^{1}H,^{13}C-HMBC NMR spectrum of compound **6** (700/171 MHz, 393 K, DMSO-d_6).
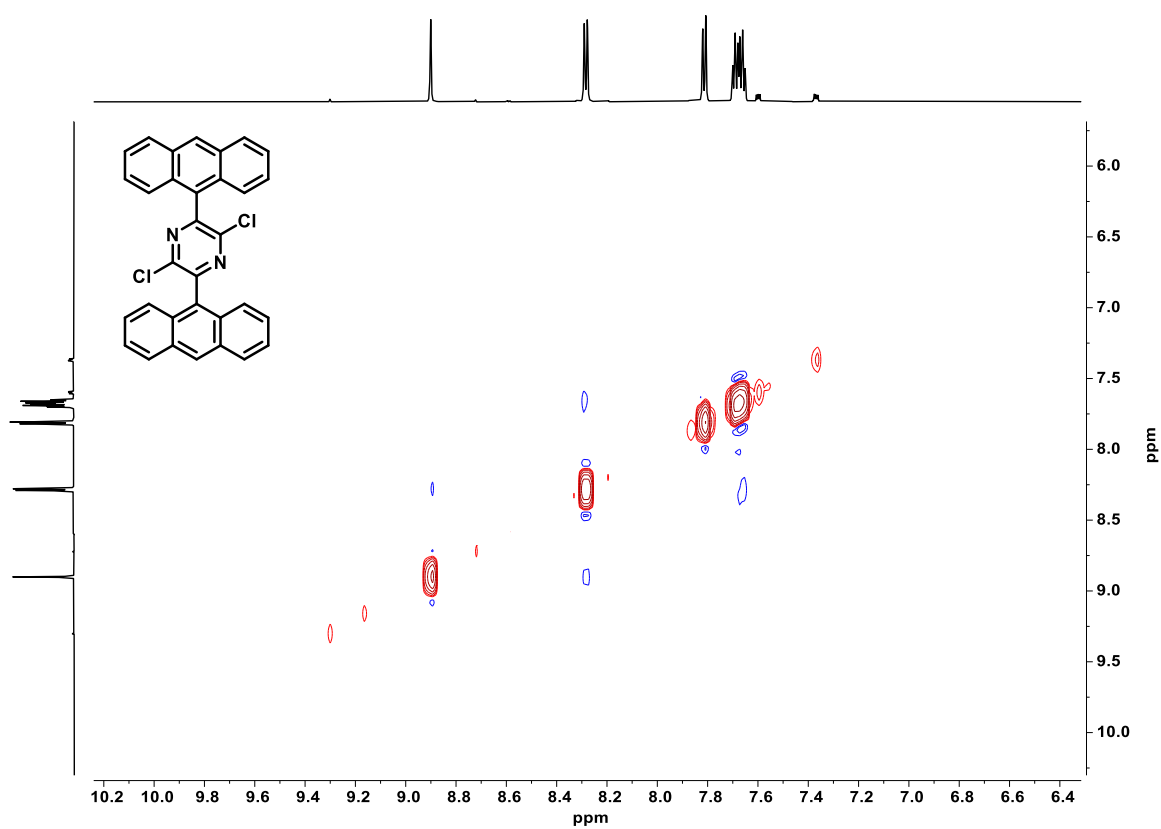
Figure S12: ^{1}H,^{1}H-NOESY NMR spectrum of compound **6** (700/700 MHz, 393 K, DMSO-d_6).
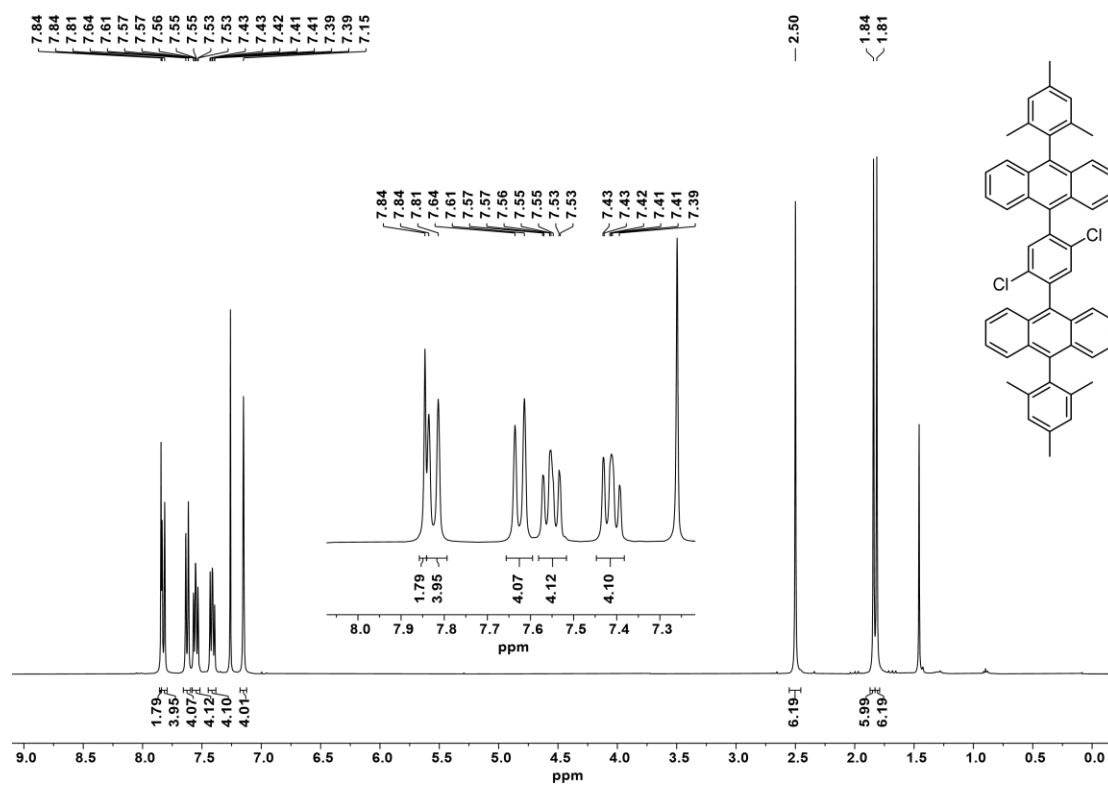
Figure S13: ^{1}H-NMR spectrum of compound **7** (400 MHz, 323 K, CDCl$_3$).
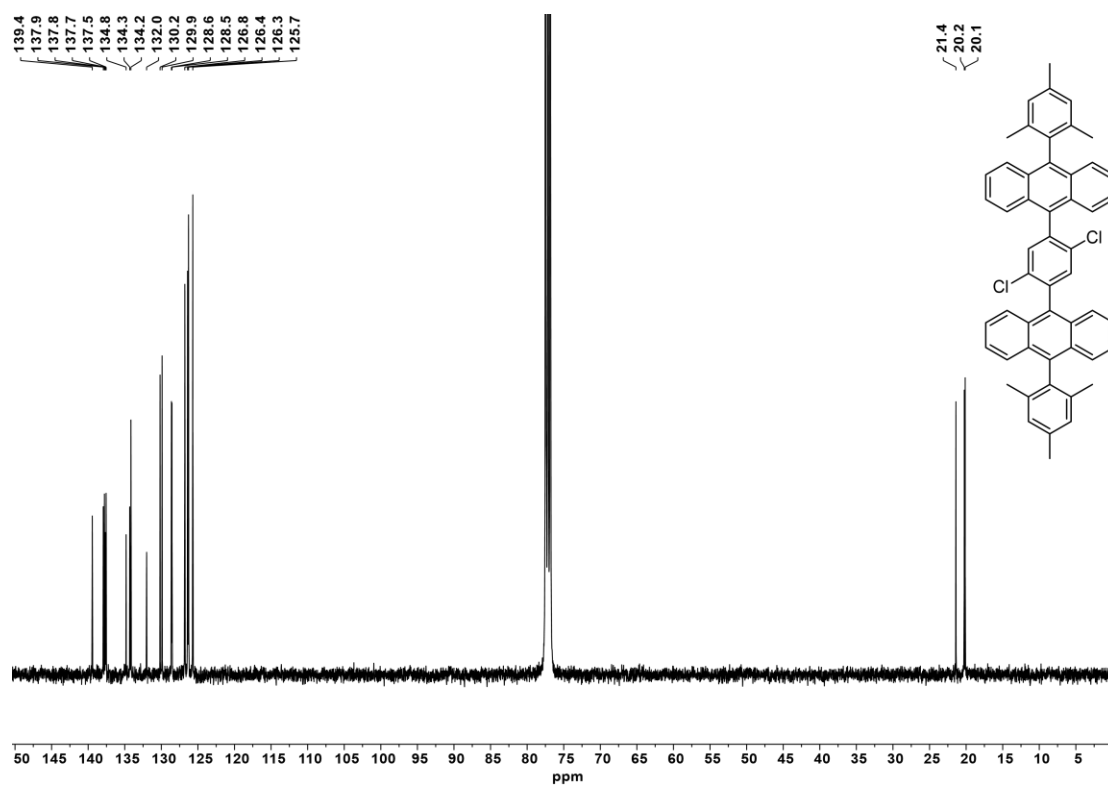
Figure S14: ^{13}C-NMR spectrum of compound **7** (101 MHz, 323 K, CDCl$_3$).
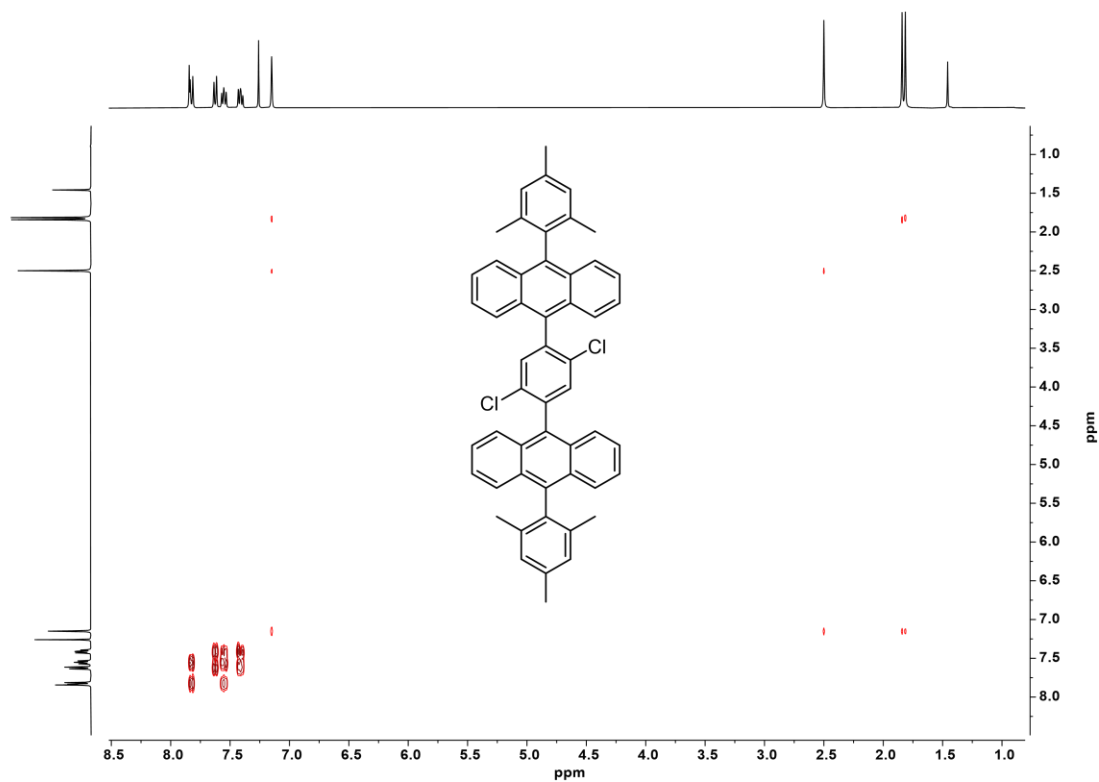
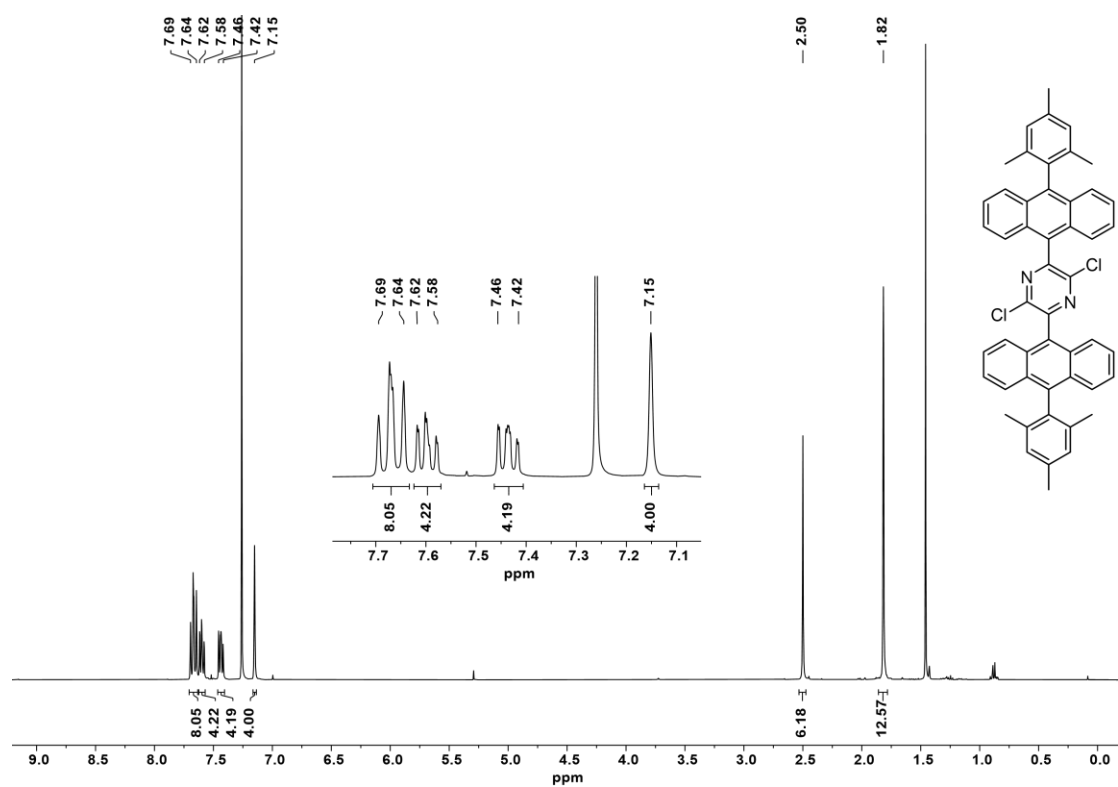**Figure S15:** ^{1}H,^{1}H-COSY NMR spectrum of compound **7** (400/400 MHz, 323 K, CDCl$_3$).
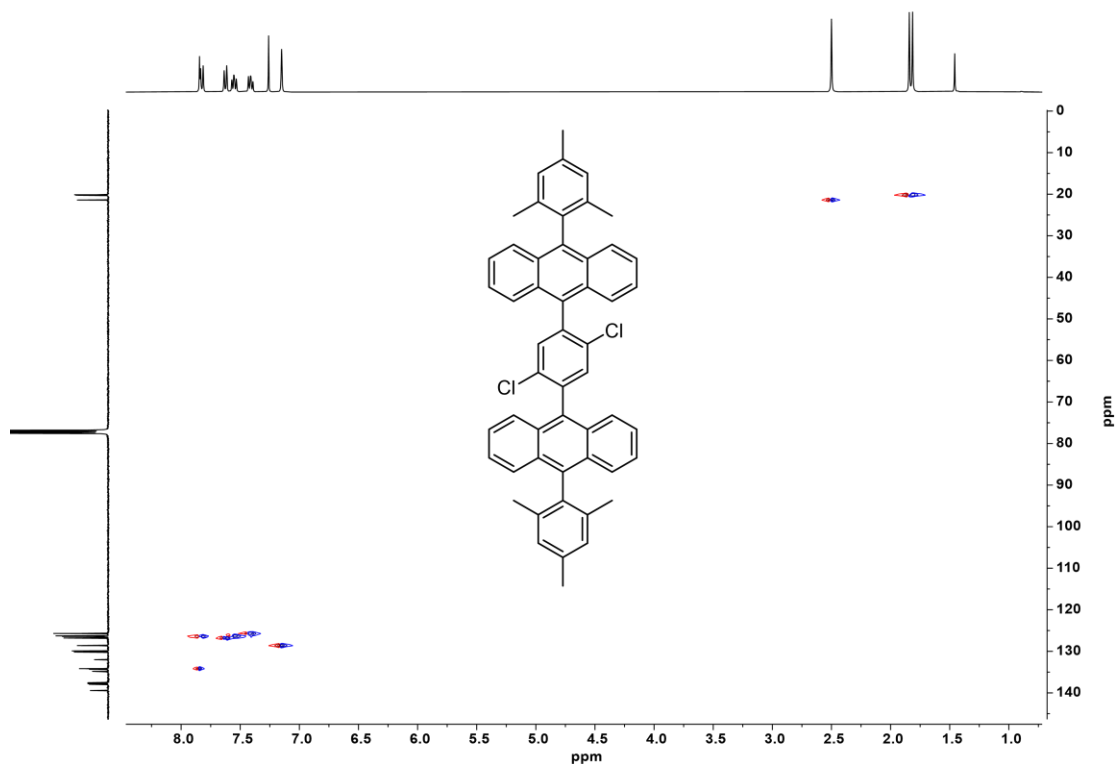
Figure S16: ^{1}H,^{13}C-HSQC NMR spectrum of compound **7** (400/101 MHz, 323 K, CDCl$_3$).
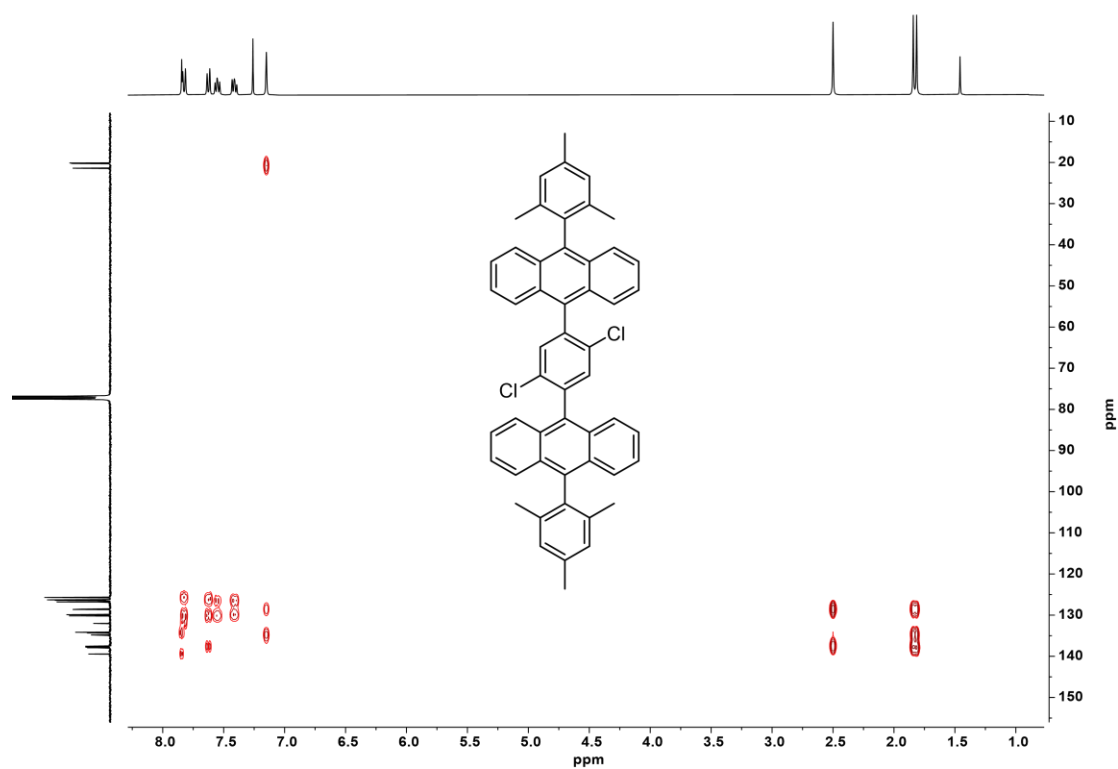
Figure S17: ^{1}H,^{13}C-HSQC NMR spectrum of compound **7** (400/101 MHz, 323 K, CDCl$_3$).
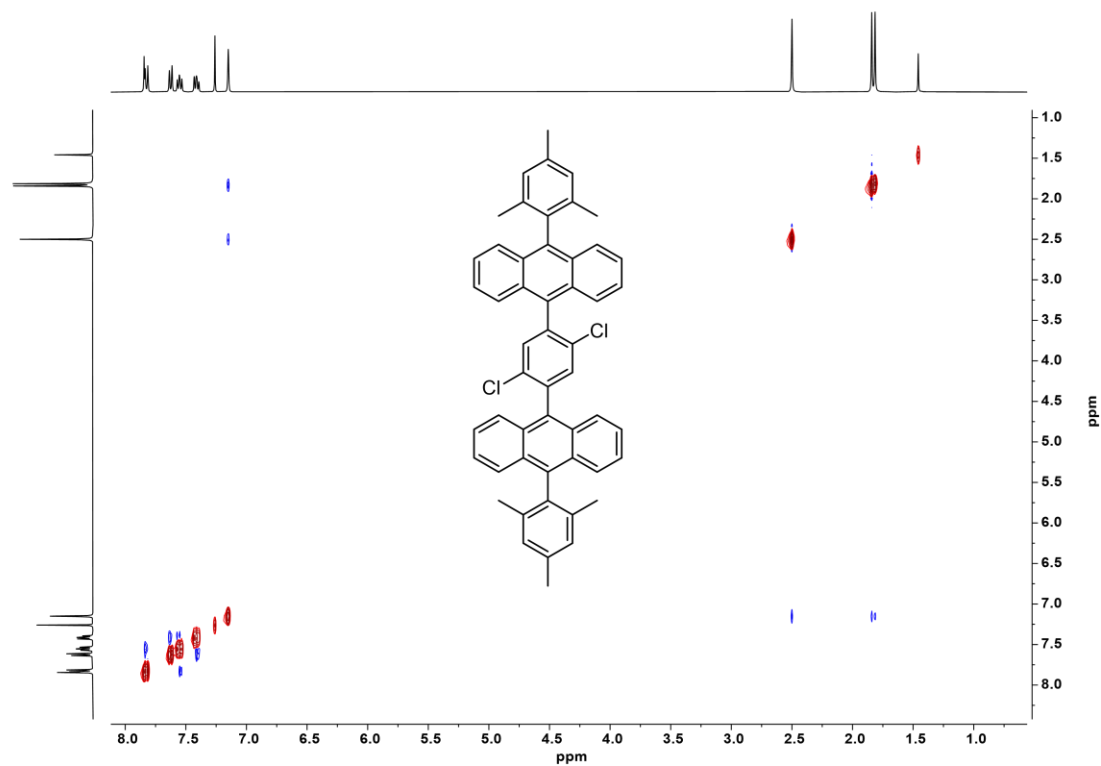
Figure S18: ^{1}H,^{1}H-NOESY NMR spectrum of compound **7** (400/400 MHz, 323 K, CDCl$_3$).

Figure S19: ^{1}H NMR spectrum of compound **8** (400 MHz, 323 K, CDCl$_3$).
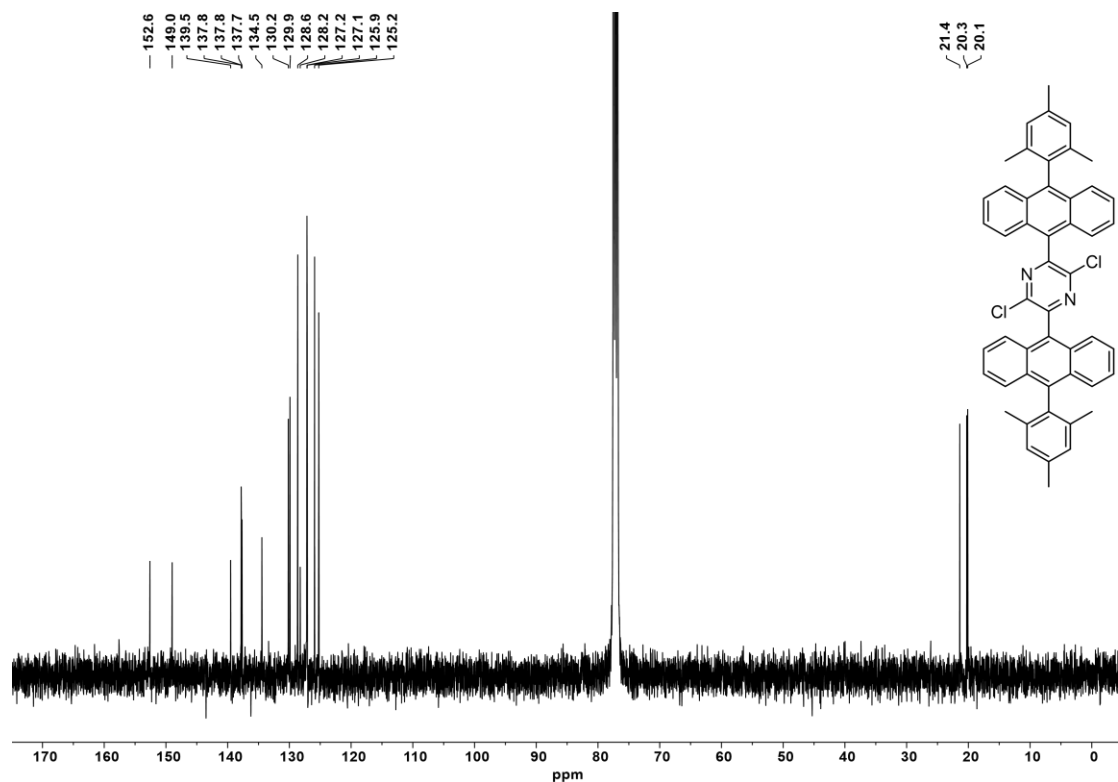
Figure S20: ^{13}C NMR spectrum of compound **8** (101 MHz, 323 K, CDCl$_3$).
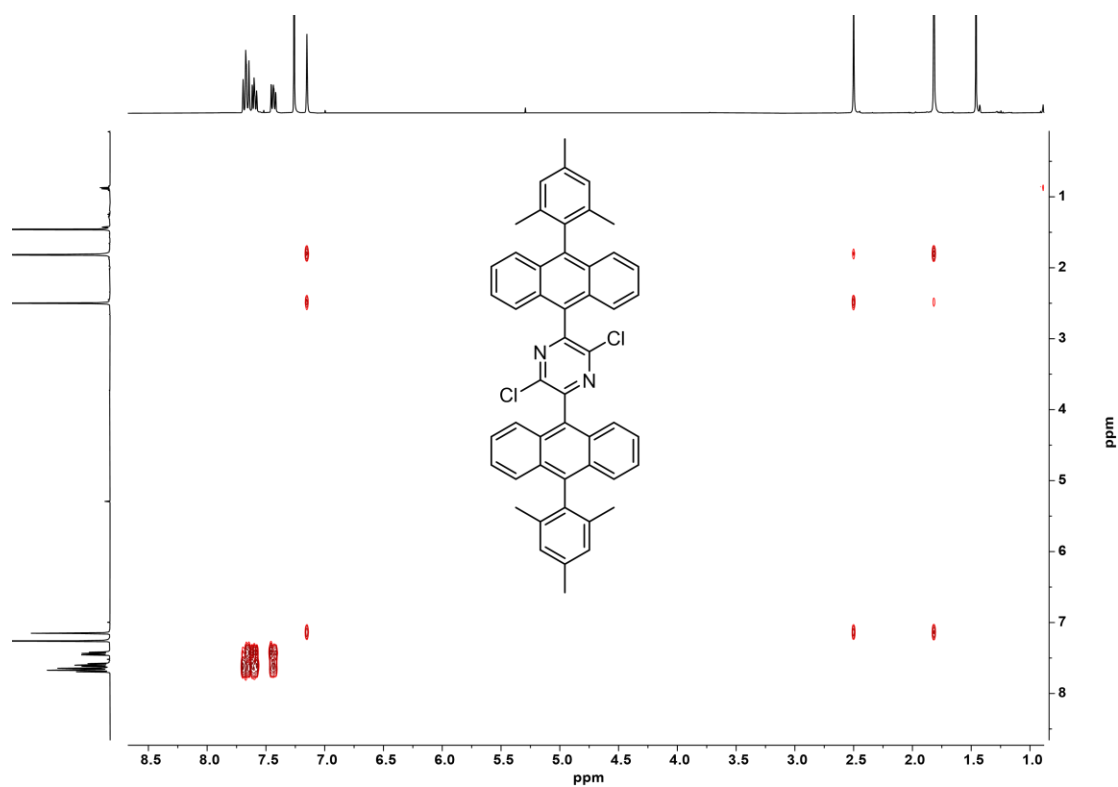
Figure S21: ^{1}H,^{1}H-COSY NMR spectrum of compound **8** (400/400 MHz, 323 K, CDCl$_3$).
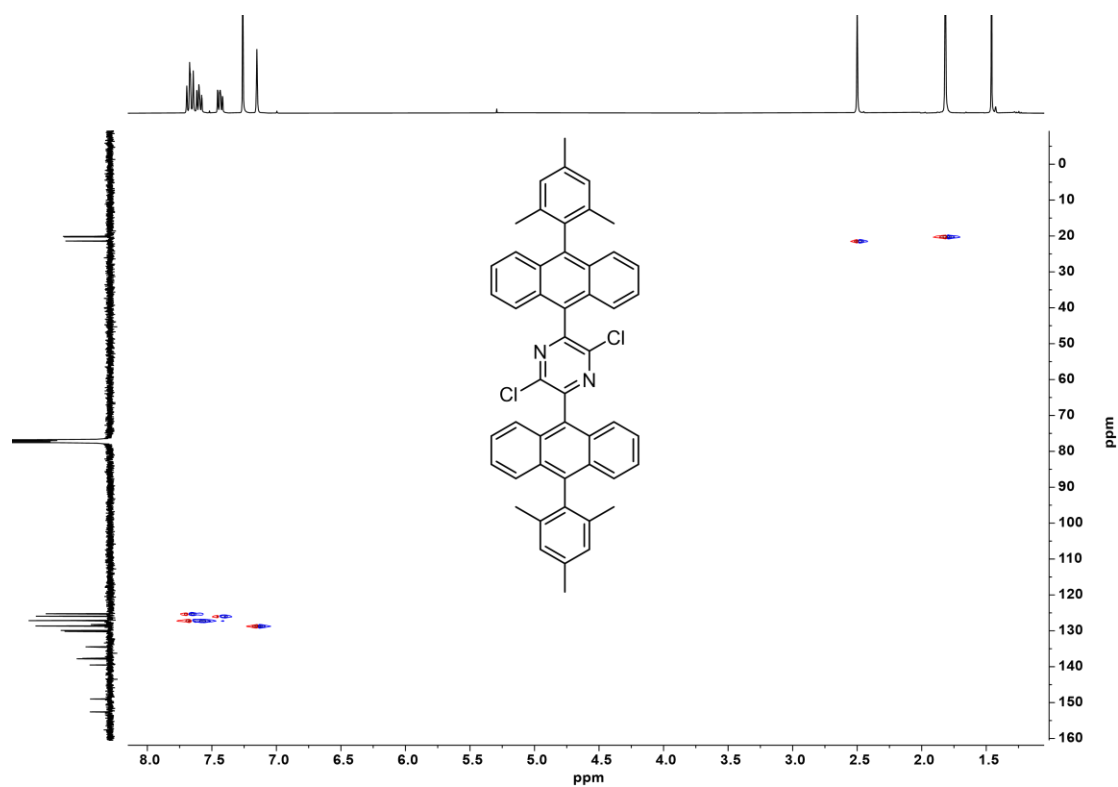
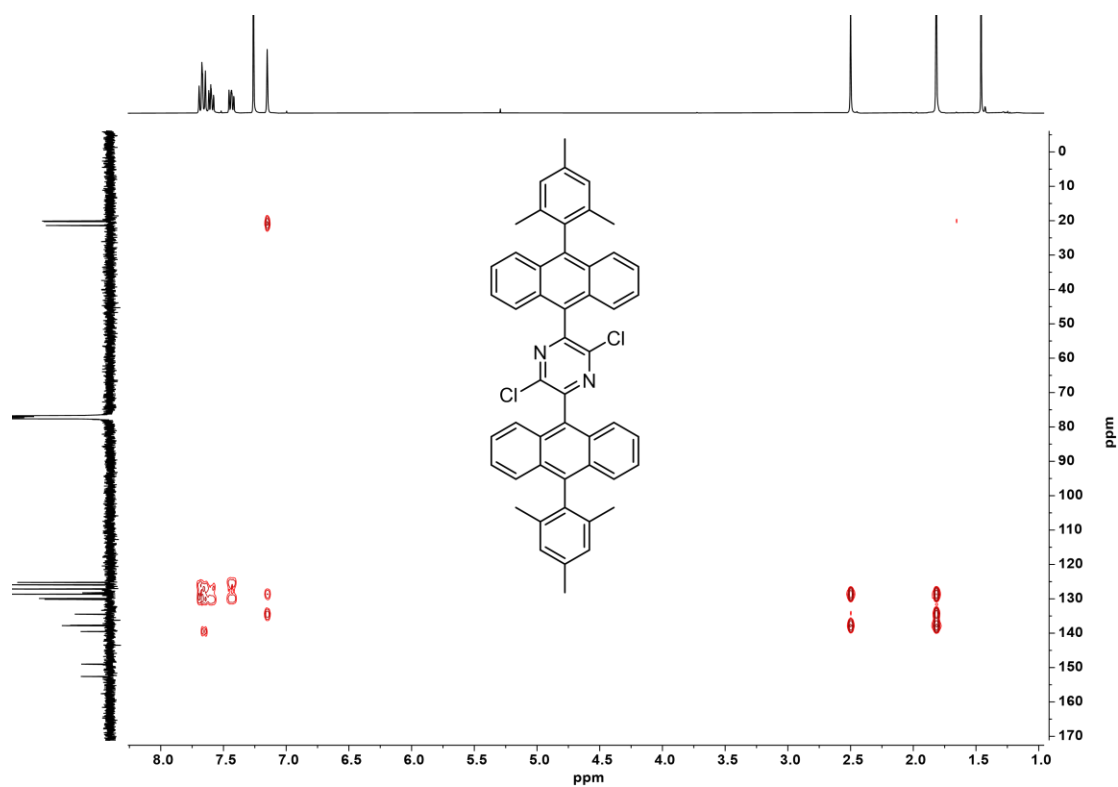**Figure S22:** ^{1}H,^{13}C-HSQC NMR spectrum of compound **8** (400/101 MHz, 323 K, CDCl$_3$).

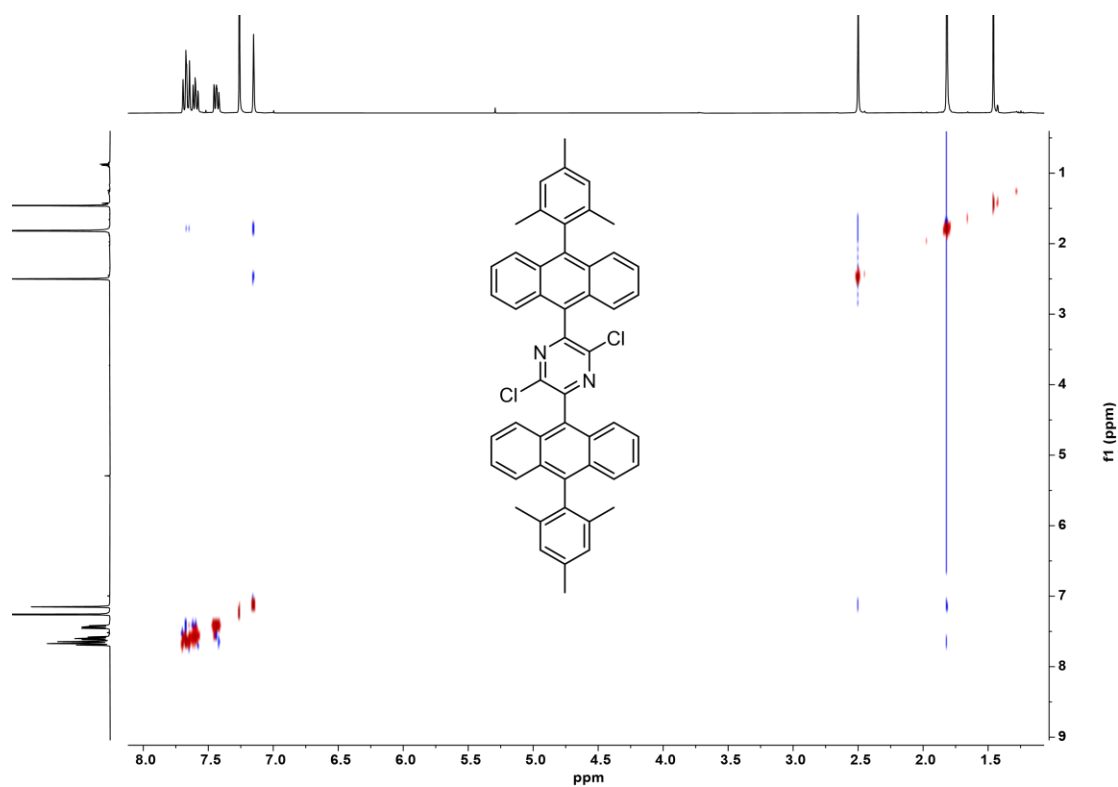**Figure S23:** ^{1}H,^{13}C-HMBC NMR spectrum of compound **8** (400/101 MHz, 323 K, CDCl$_3$).

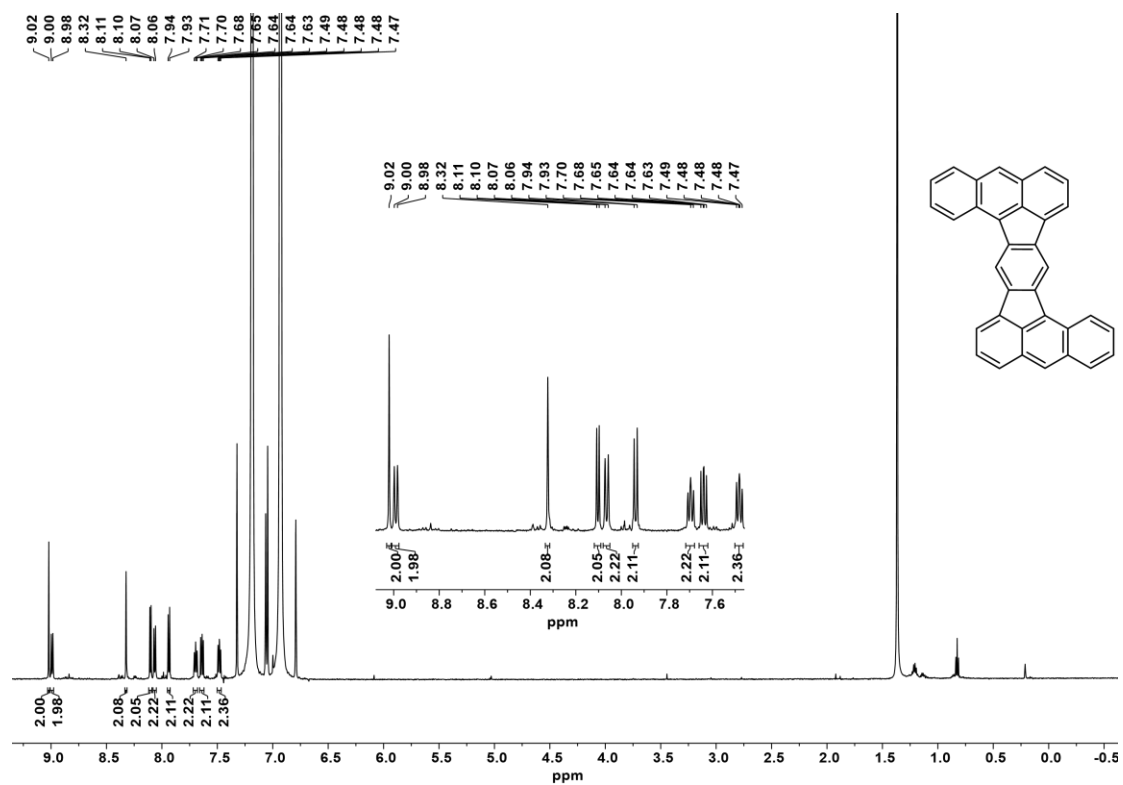**Figure S24:** ^{1}H,^{1}H-NOESY NMR spectrum of compound **8** (400/400 MHz, 323 K, CDCl$_3$).

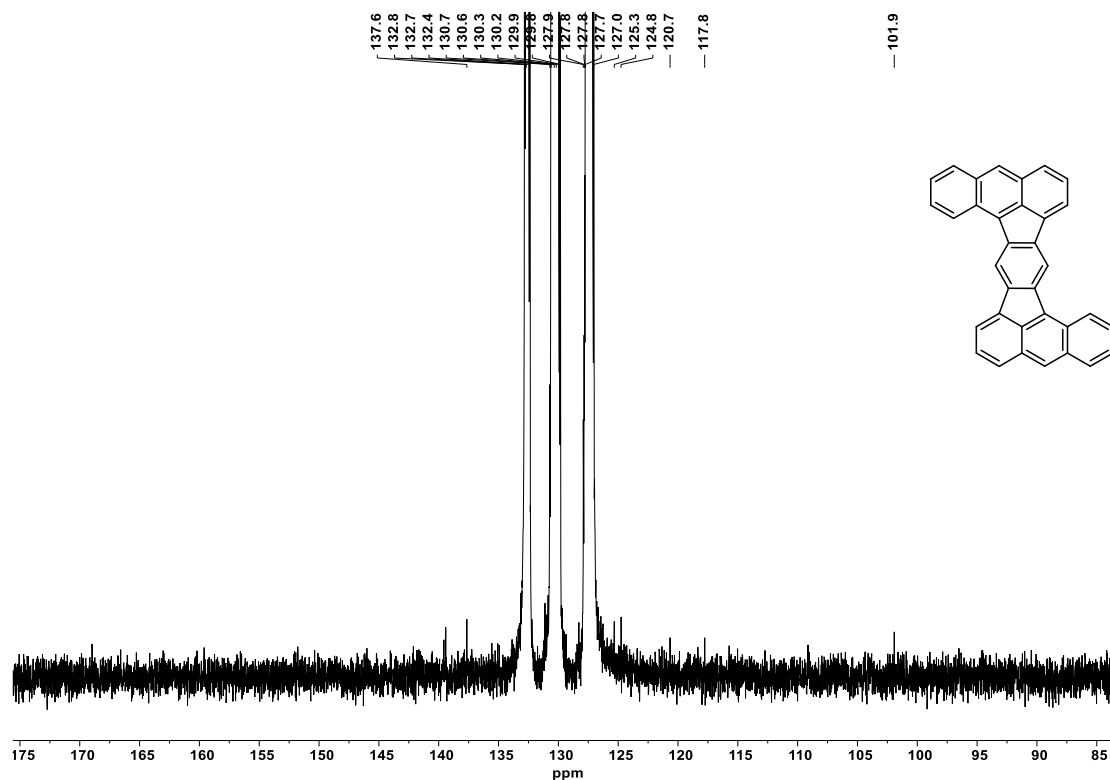**Figure S25:** ^{1}H NMR spectrum of compound **DBAF** (600 MHz, *o*-DCB-*d*$_4$).

Figure S26: ^{13}C-NMR spectrum of compound **DBAF** (151 MHz, *o*-DCB-*d*$_4$).
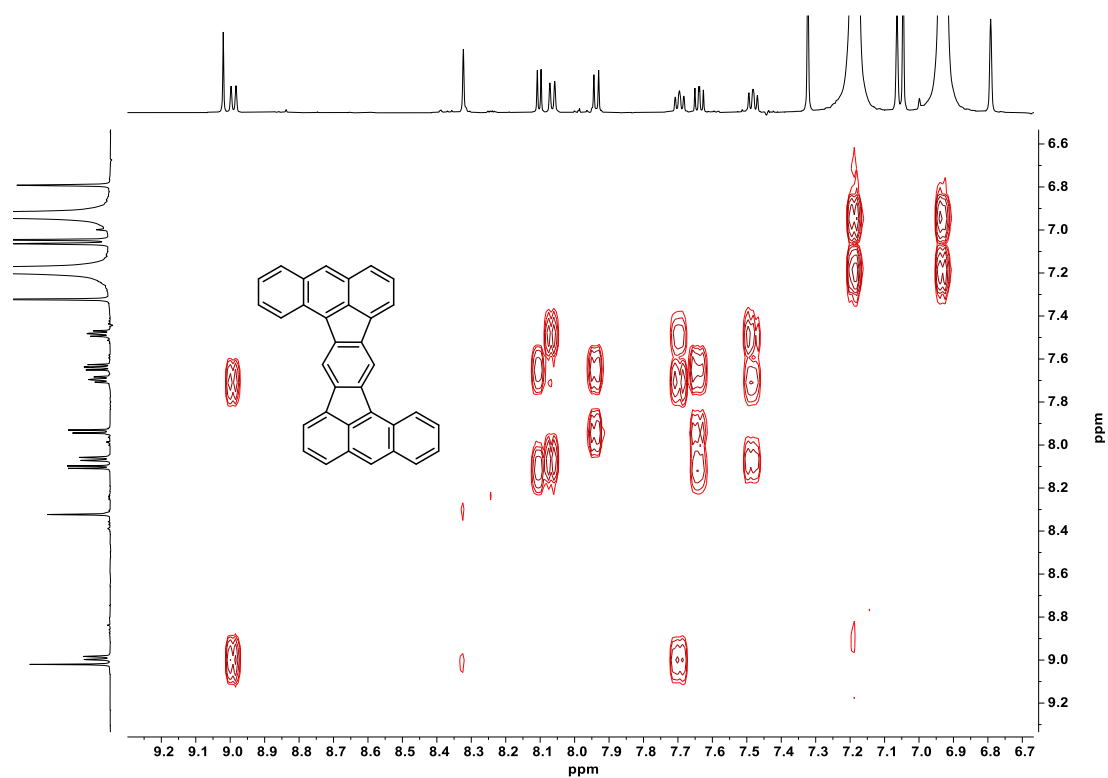
Figure S27:: ^{1}H,^{1}H-COSY NMR spectrum of compound **DBAF** (600/600 MHz, *o*-DCB-*d*4).
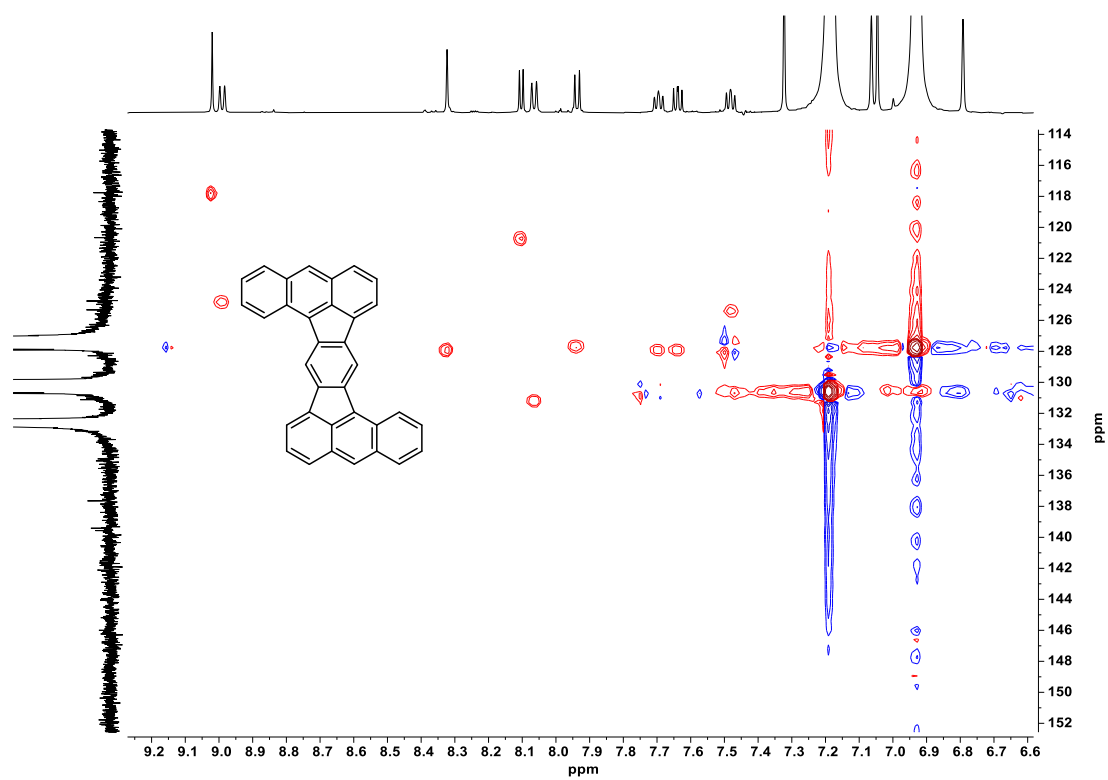

Figure S28: ^{1}H,^{13}C-HSQC NMR spectrum of compound **DBAF** (600/151 MHz, *o*-DCB-*d*4).
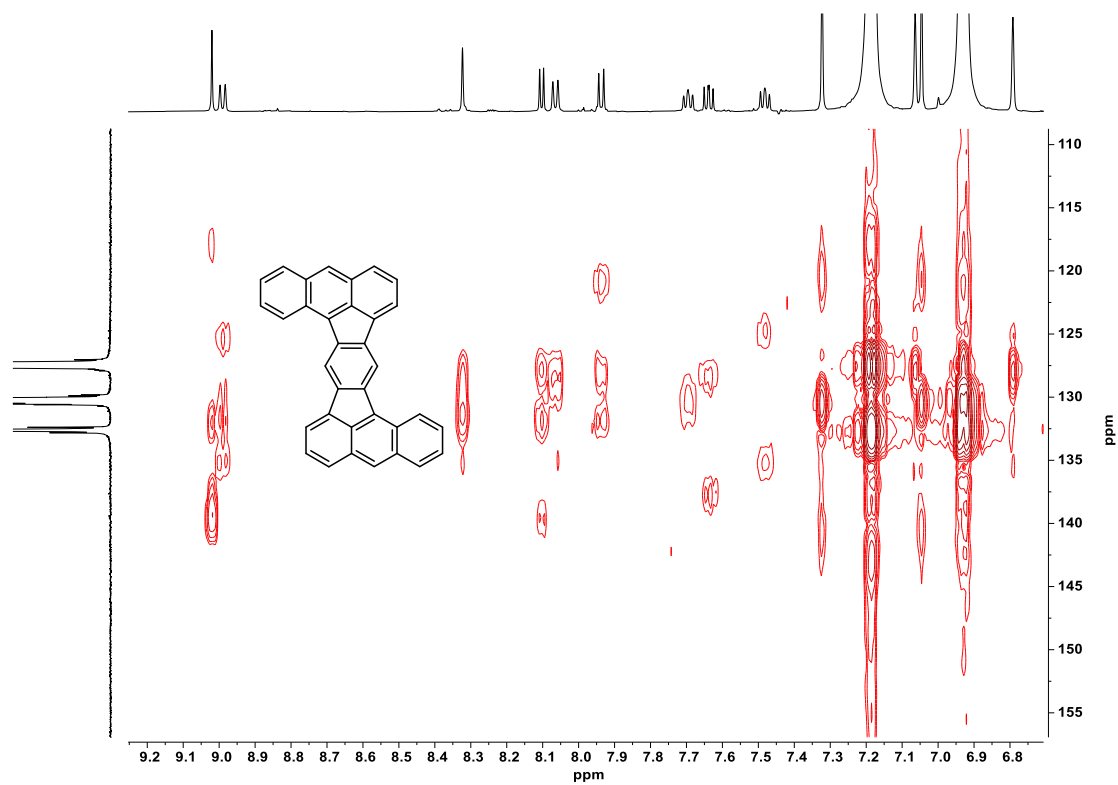
Figure S29: ^{1}H,^{13}C-HMBC NMR spectrum of compound **DBAF** (600/151 MHz, *o*-DCB-*d*$_4$).
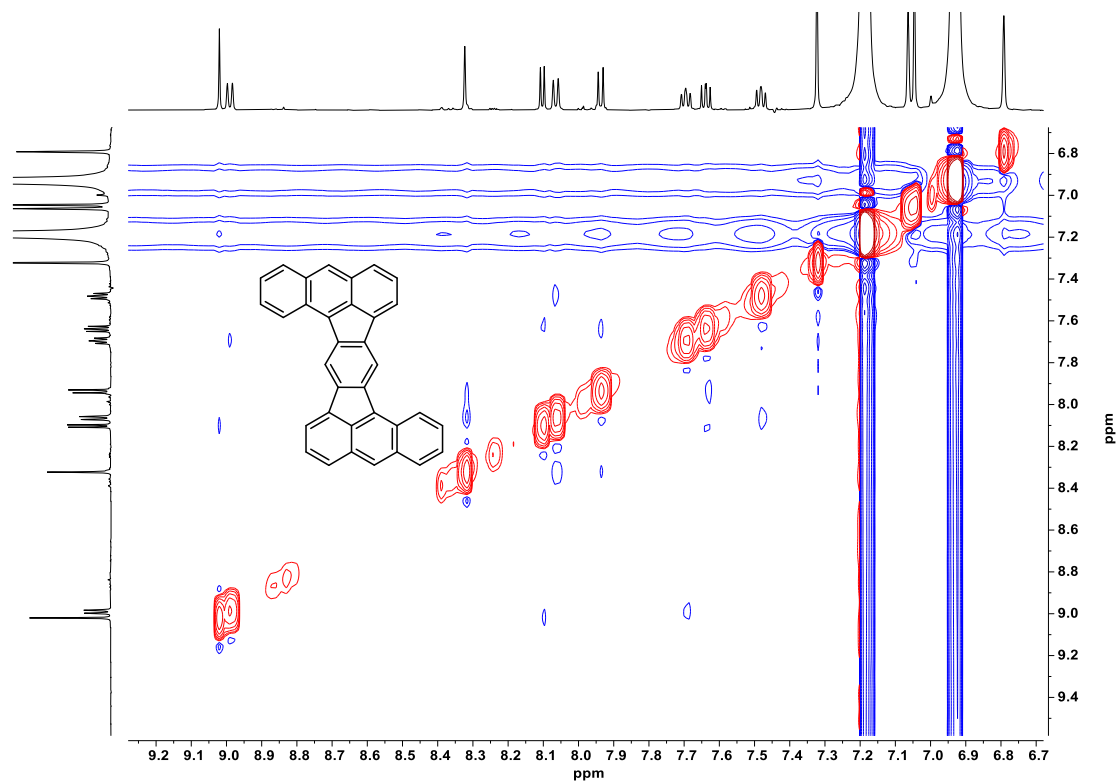

Figure S30: ^{1}H,^{1}H-NOESY NMR spectrum of compound **DBAF** (600/600 MHz, *o*-DCB-*d*$_4$).
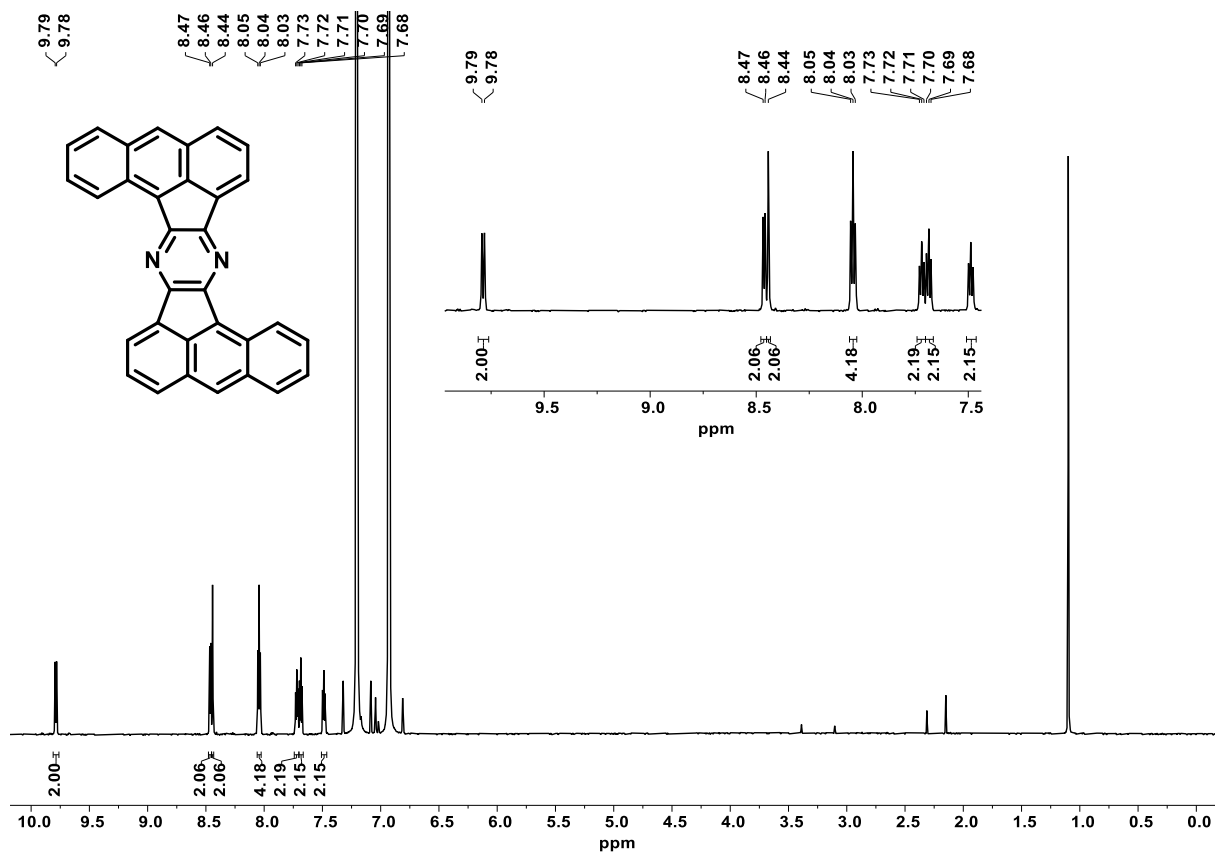
Figure S31: ^{1}H NMR spectrum of compound **DBAF-N$_2$** (700 MHz, o-DCB-d_4, 393 K).
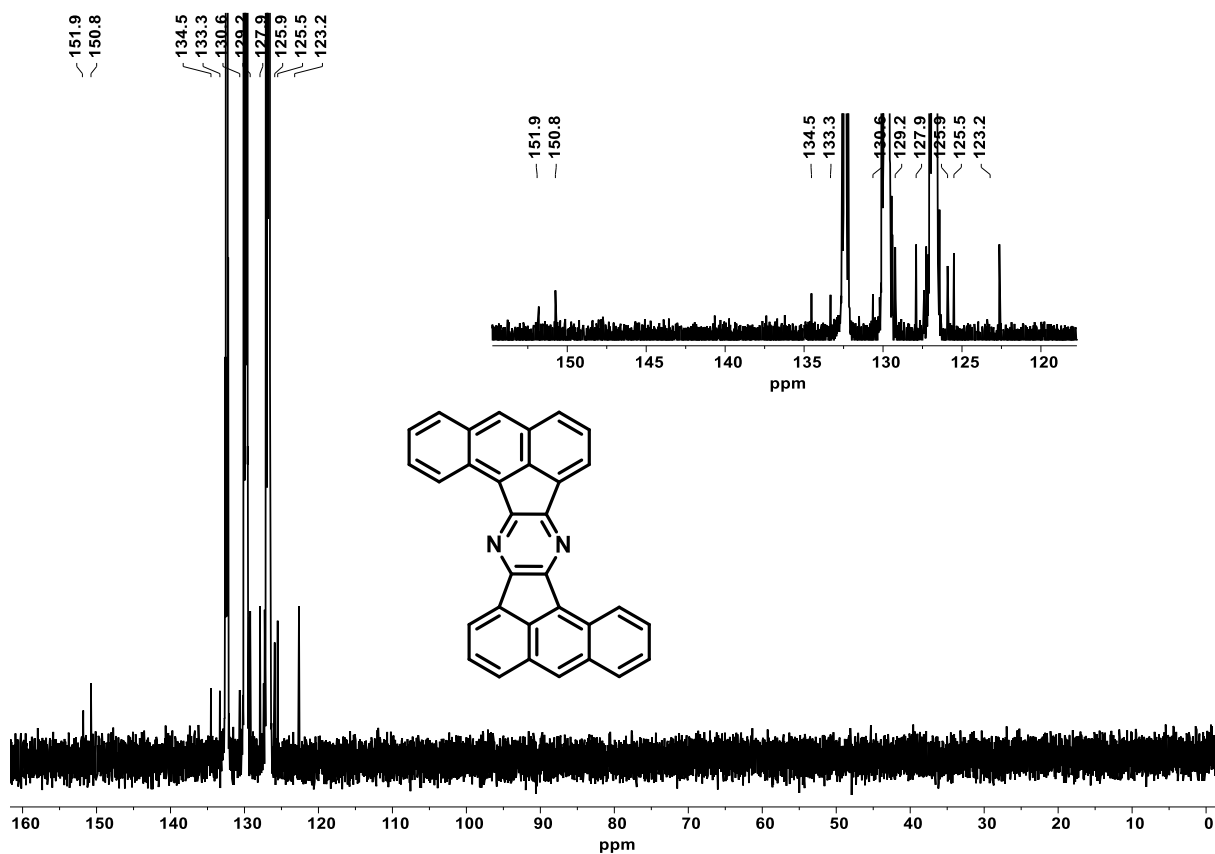
Figure S32: ^{13}C-NMR spectrum of compound **DBAF-N$_2$** (171 MHz, o-DCB-d_4, 393 K, 10240 scans).
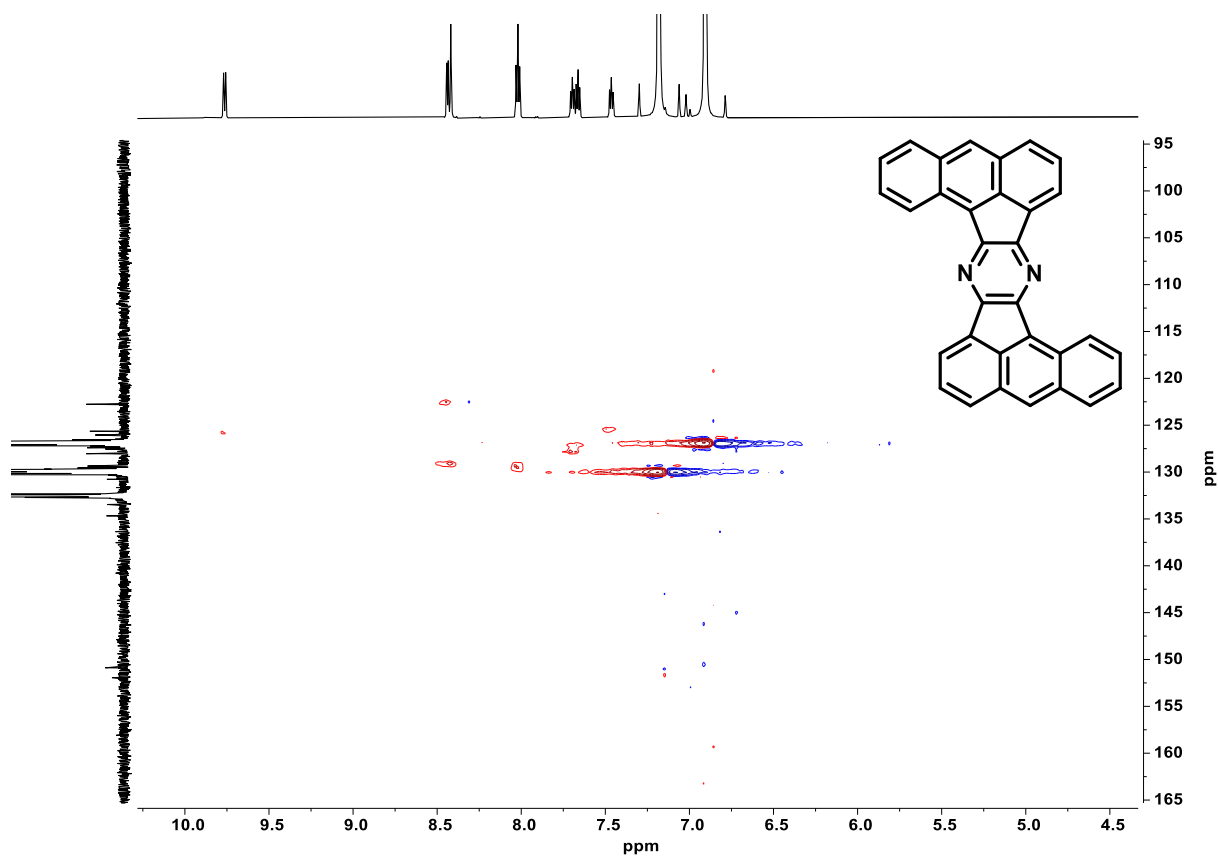
Figure S33: ^{1}H,^{1}H-COSY NMR spectrum of compound **DBAF-N₂** (600/600 MHz, *o*-DCB-*d₄*, 393 K).
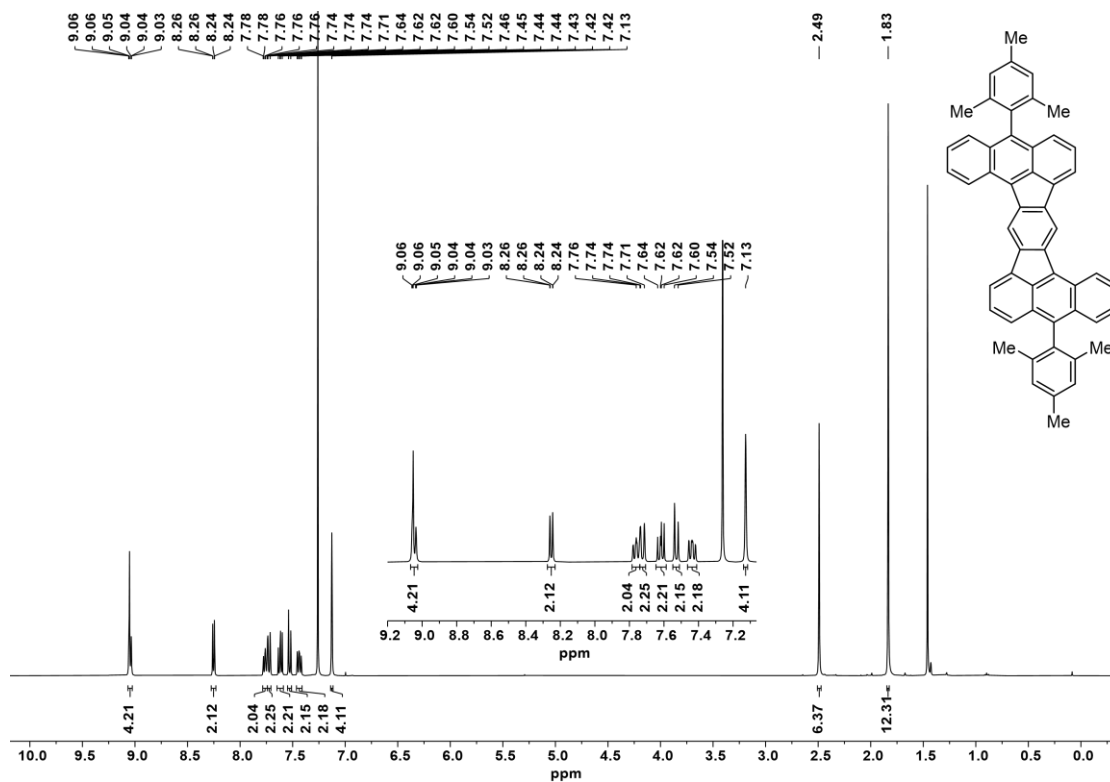
Figure S34: ^{1}H NMR spectrum of compound **mes-DBAF** (400 MHz, 323 K, CDCl₃).
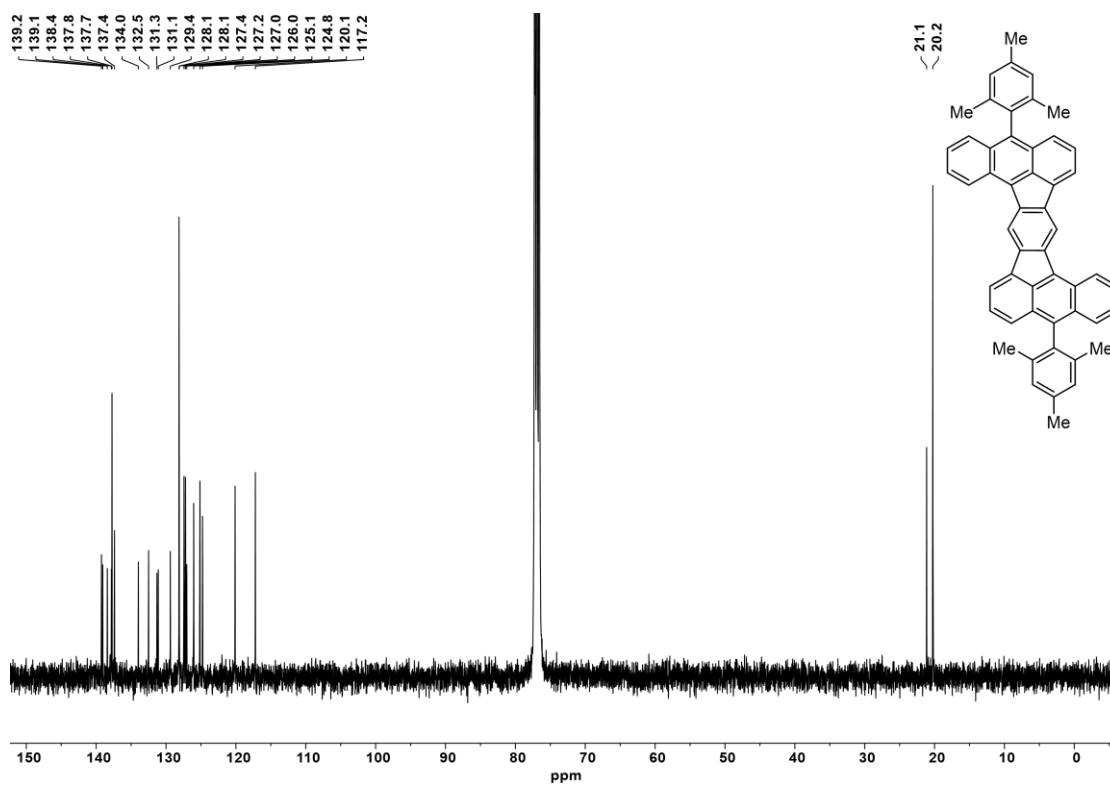
Figure S35: ^{13}C NMR spectrum of compound **mes-DBAF** (101 MHz, 323 K, CDCl₃).
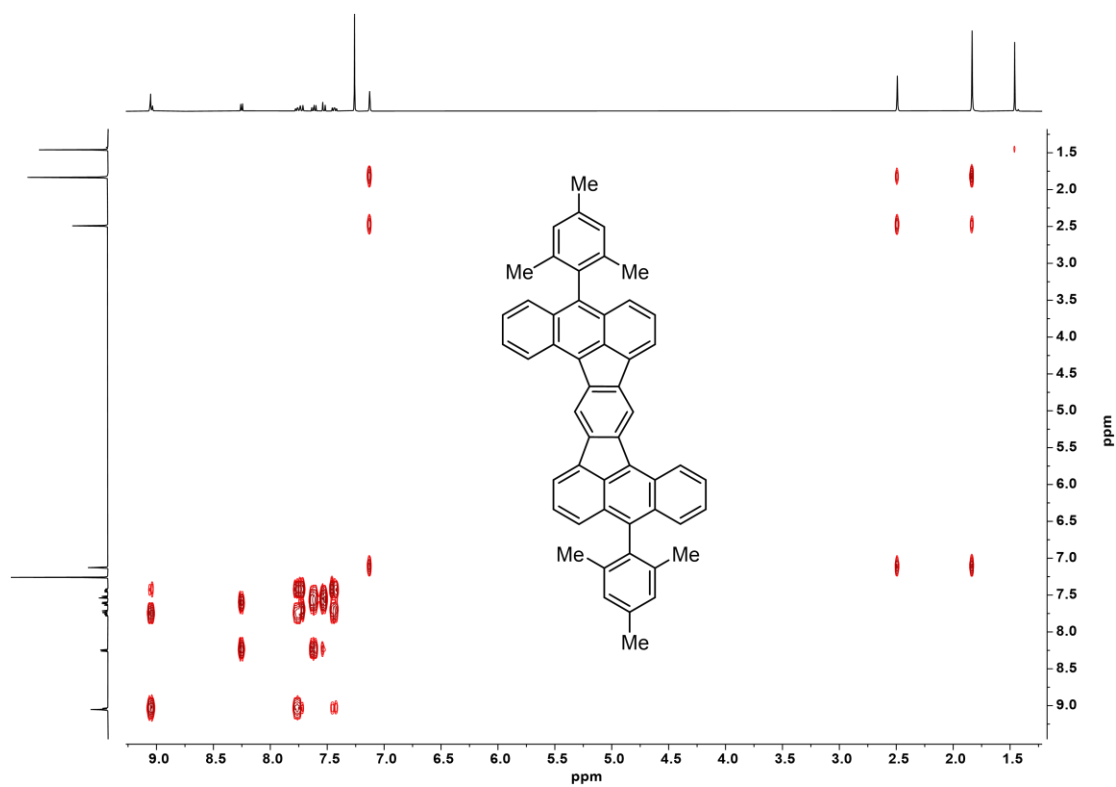
Figure S36: ^{1}H,^{1}H-COSY NMR spectrum of compound **mes-DBAF** (400/400 MHz, 323 K, CDCl₃).
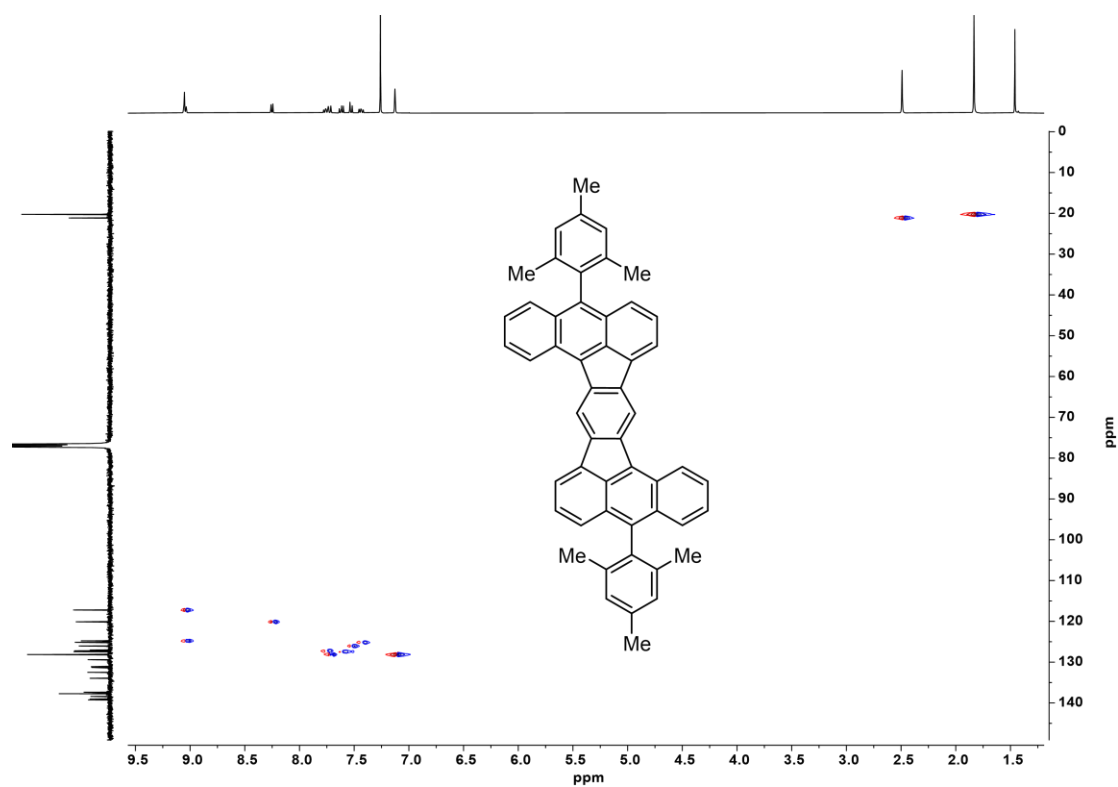
Figure S37: ¹H,¹³C-HSQC spectrum of compound **mes-DBAF** (400/101 MHz, 323 K, CDCl₃).
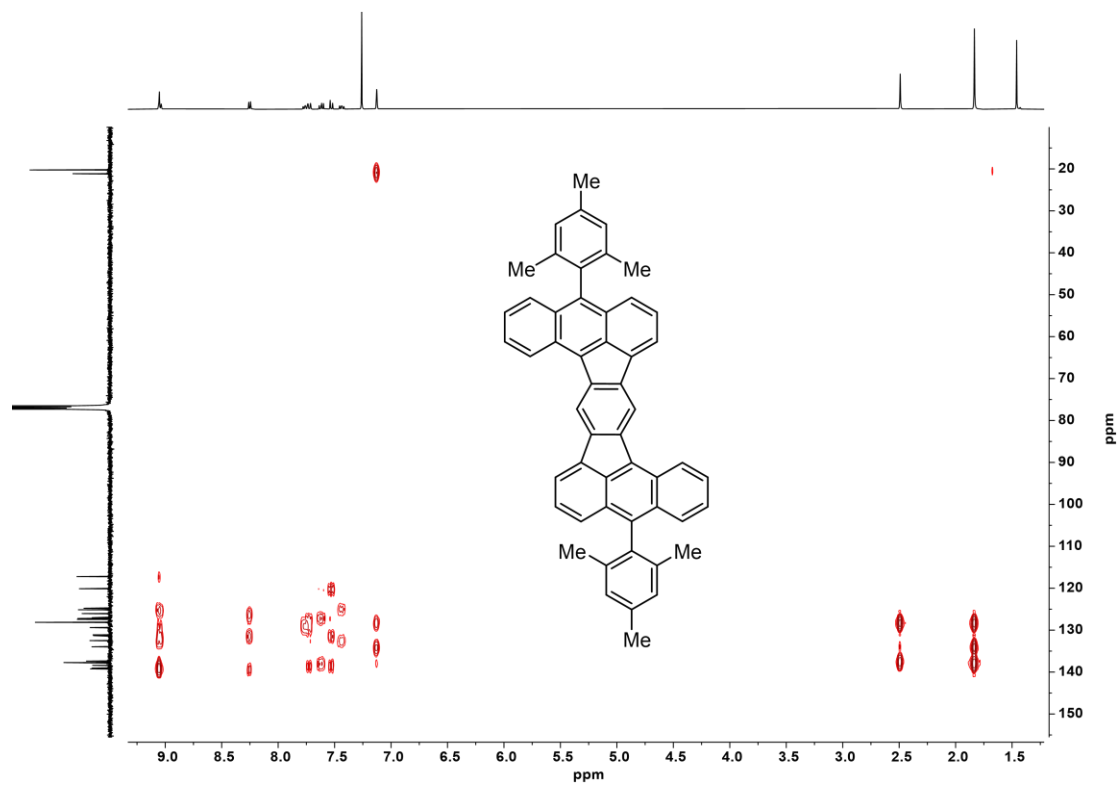
Figure S38: ¹H,¹³C-HMBC NMR spectrum of compound **mes-DBAF** (400/101 MHz, 323 K, CDCl₃).
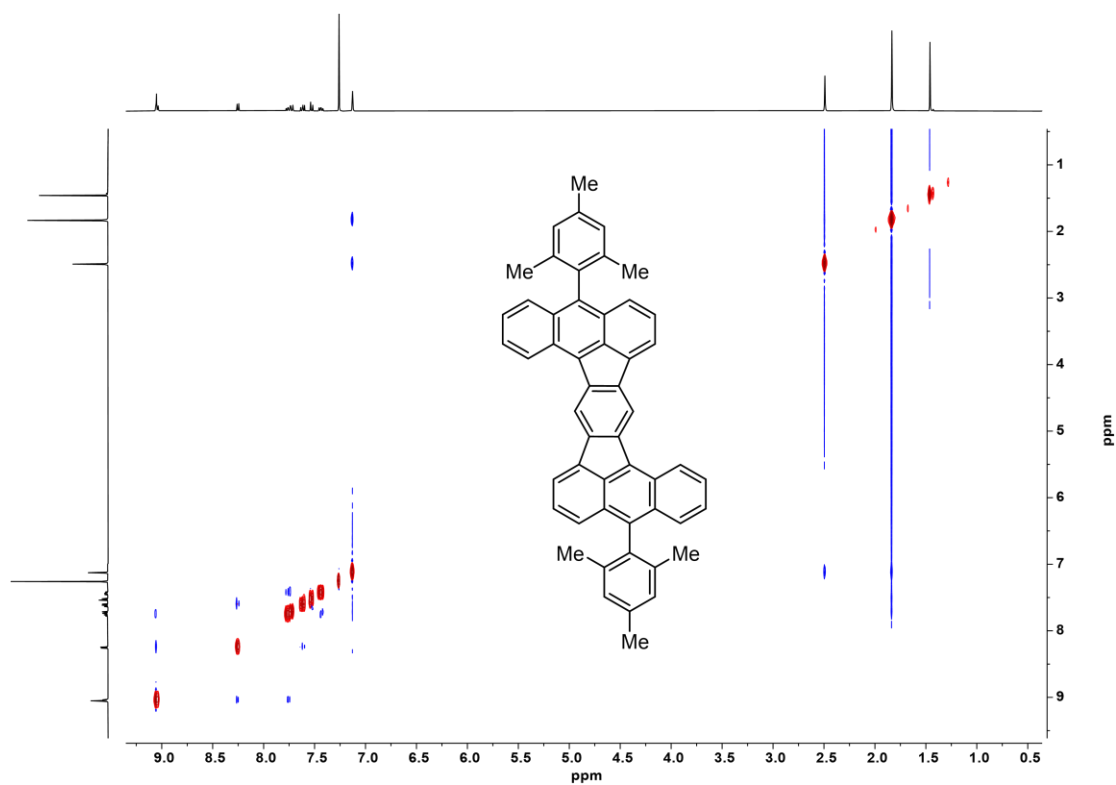
Figure S39: ^{1}H,^{1}H-NOESY NMR spectrum of compound **mes-DBAF** (400/400 MHz, 323 K, CDCl$_3$).
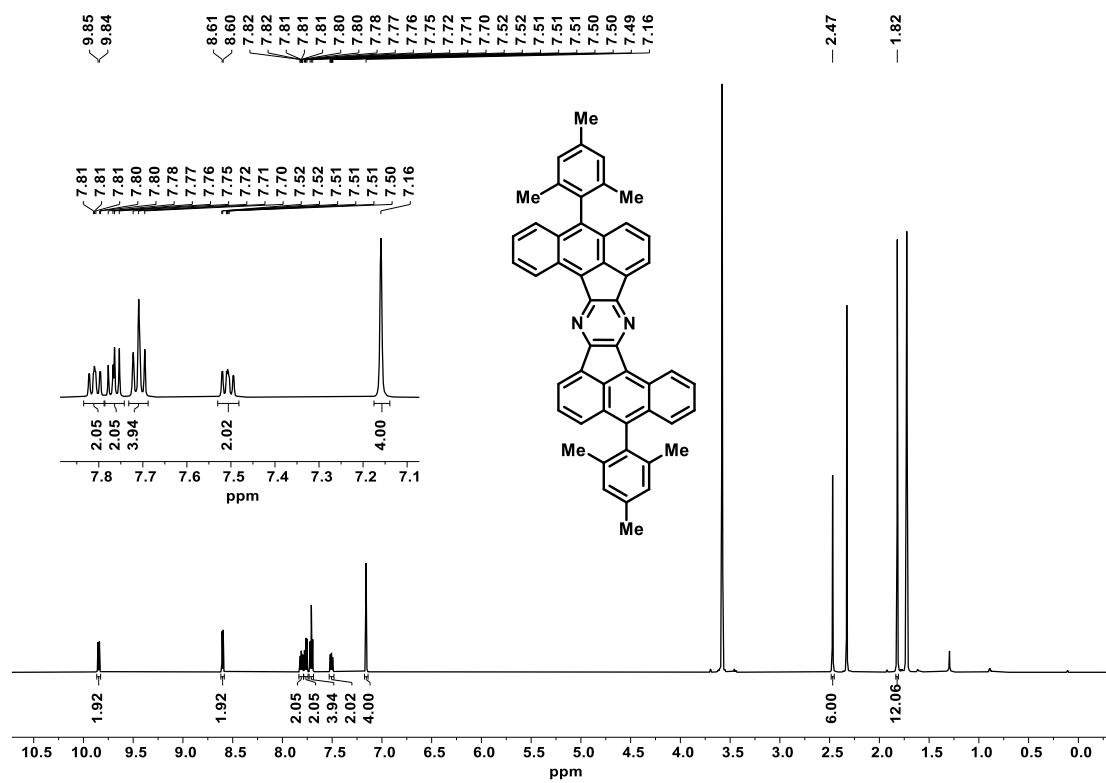
Figure S40: ^{1}H NMR spectrum of **mes-DBAF-N$_2$** (600 MHz, 323 K, THF-d_8).
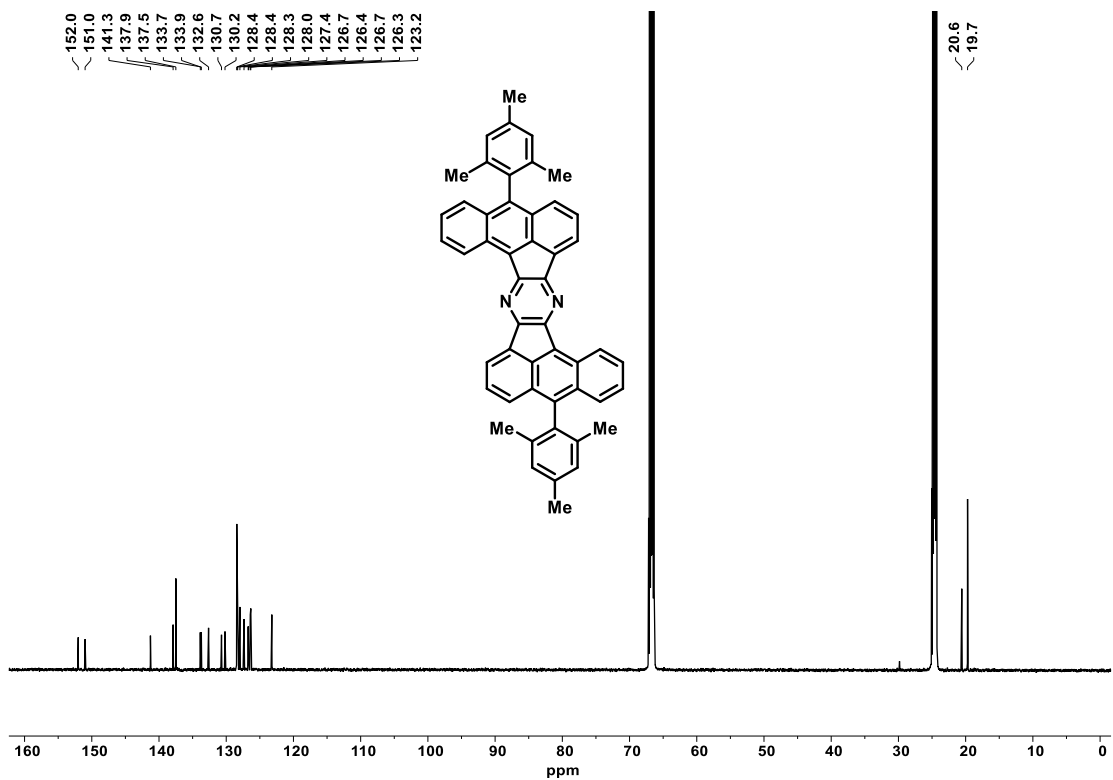
Figure S41: ^{13}C NMR spectrum of **mes-DBAF-N₂** (151 MHz, 323 K, THF-d_8).
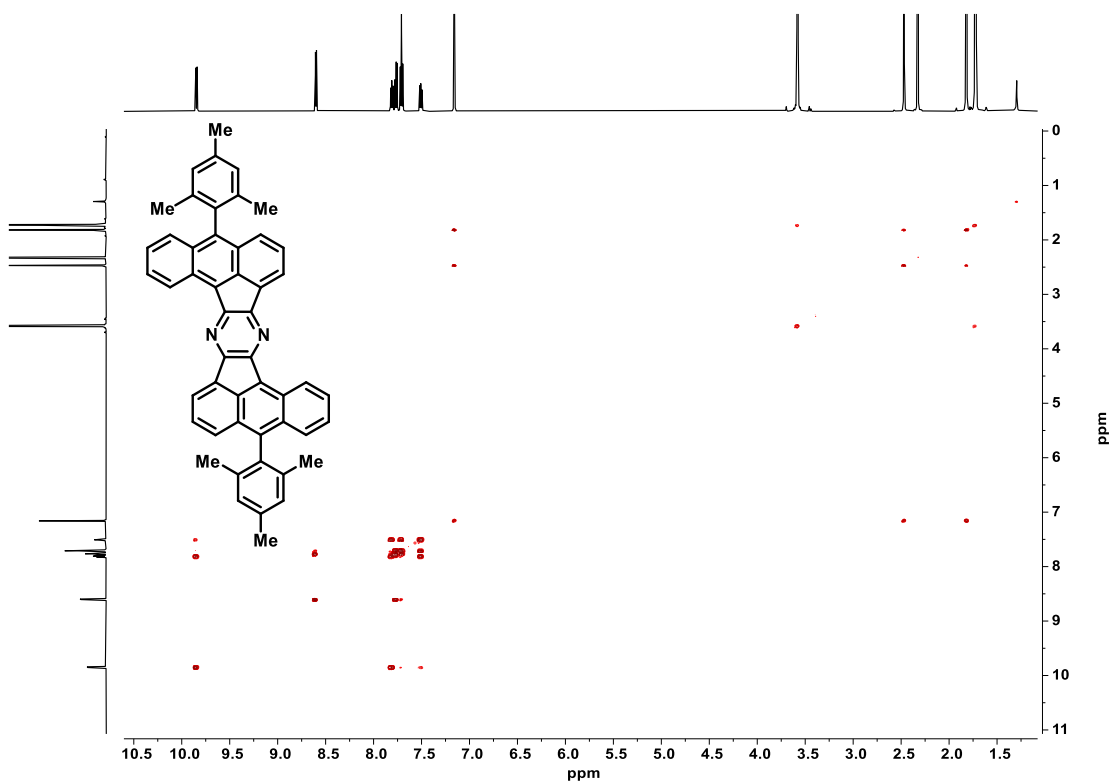
Figure S42: $^{1}H,^{1}H$ NMR spectrum of **mes-DBAF-N₂** (600/600 MHz, 323 K, THF-d_8).
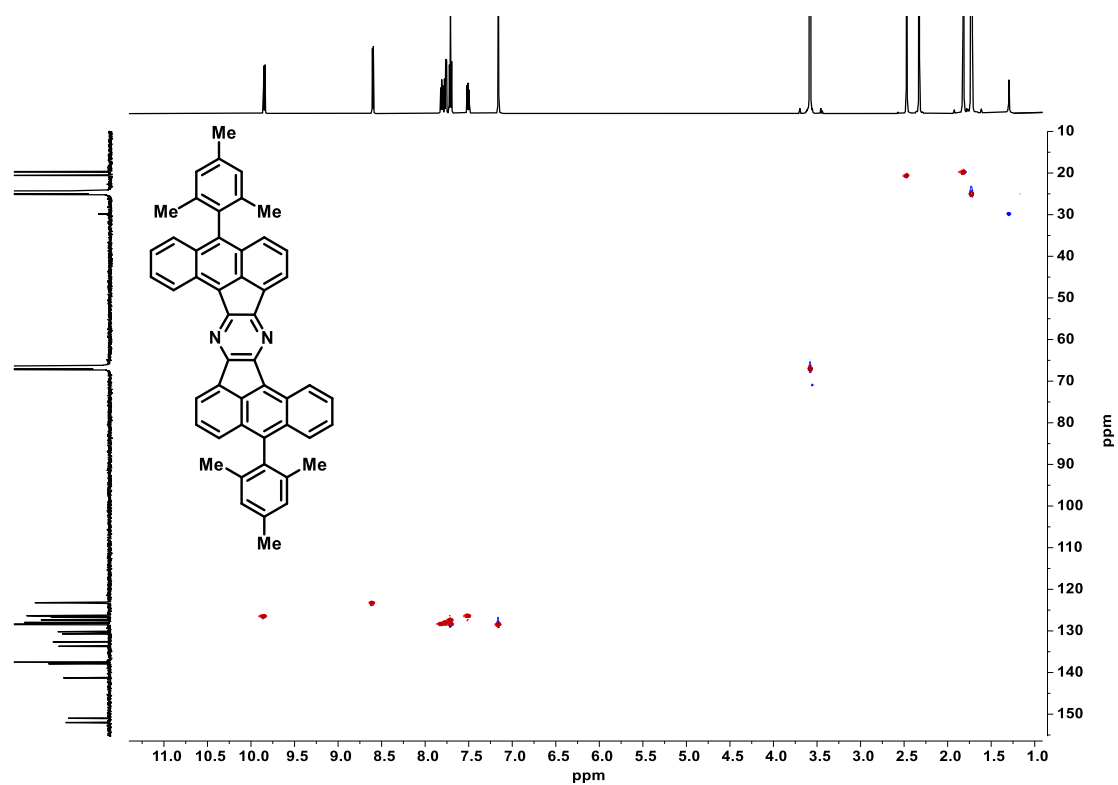
Figure S43: ^{1}H,^{13}C-HSQC NMR spectrum of **mes-DBAF-N$_2$** (600/151 MHz, 323 K, THF-d_8).
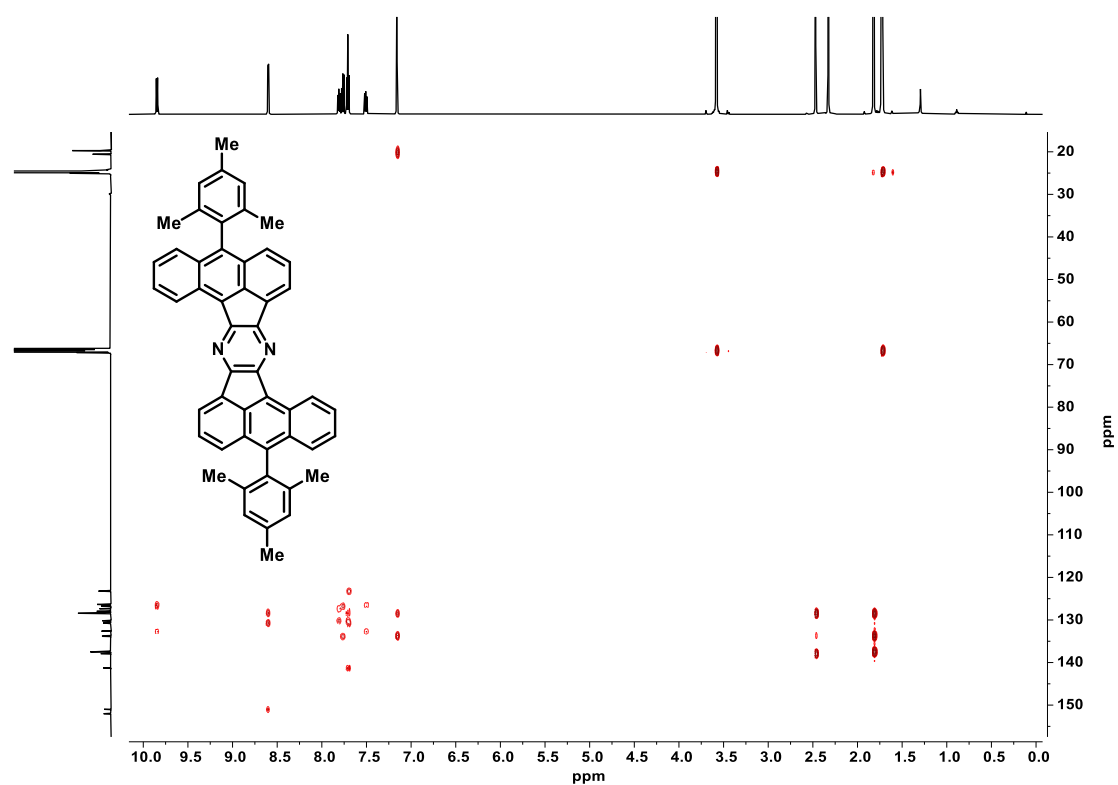
Figure S44: ^{1}H,^{13}C-HMBC NMR spectrum of **mes-DBAF-N$_2$** (600/151 MHz, 323 K, THF-d_8).
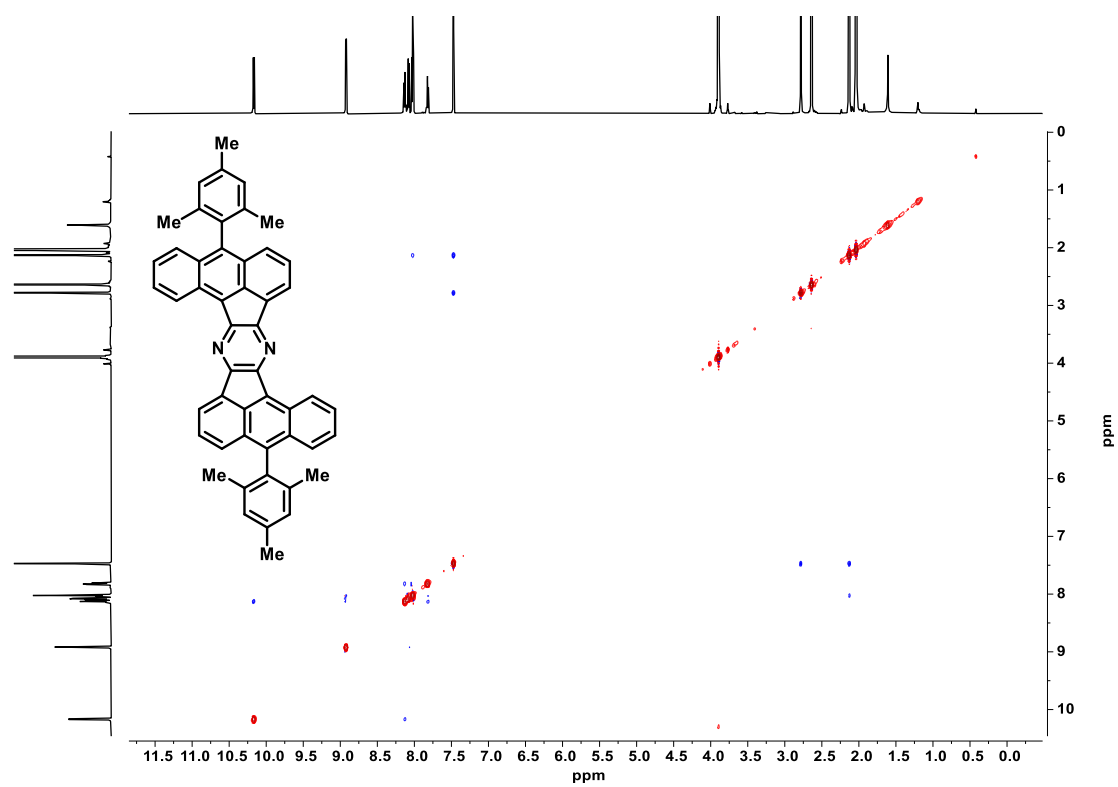
Figure S45: ^{1}H,^{1}H-NOESY NMR spectrum of **mes-DBAF-N$_2$** (600/600 MHz, 323 K, THF-*d$_8$*).

4. FTIR Spectroscopy
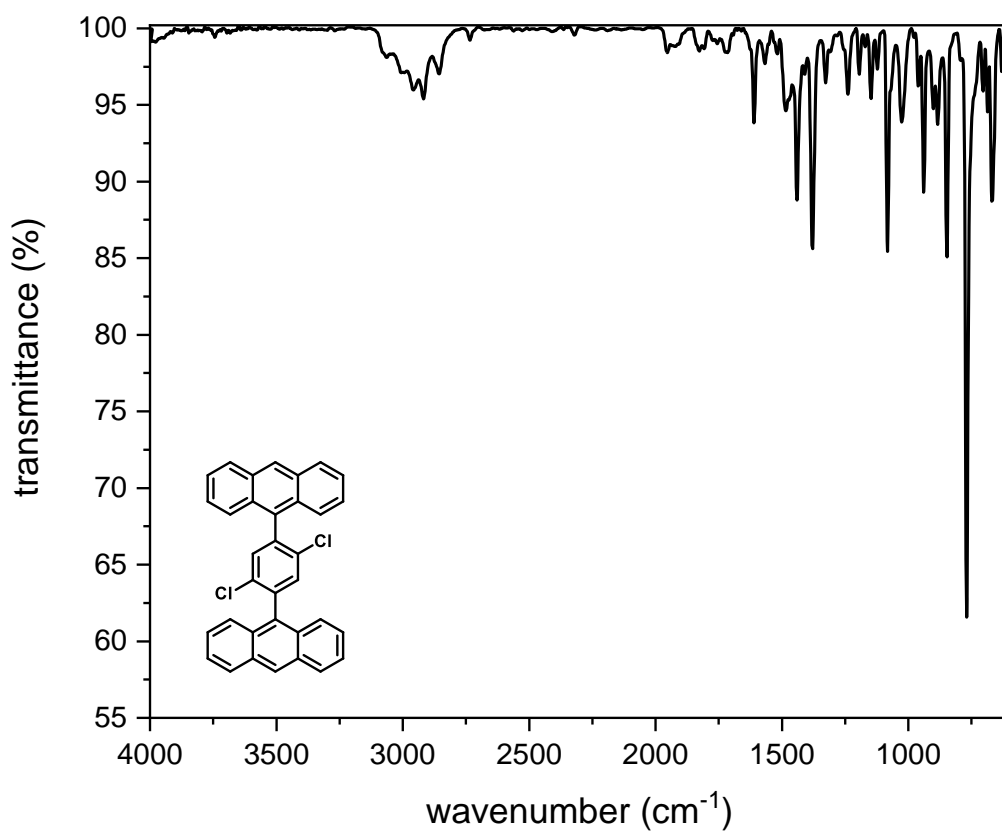
Figure S46: FT-IR spectrum of compound **5** (ATR, ZnSe).
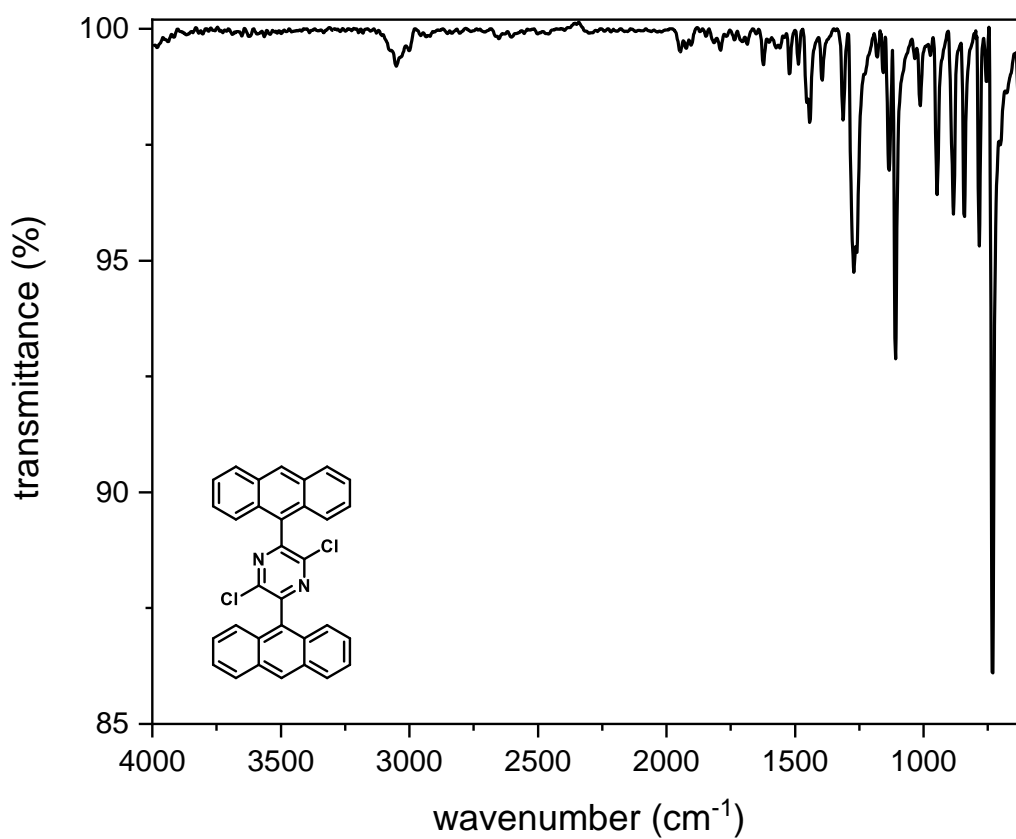
Figure S47: FT-IR spectrum of compound **6** (ATR, ZnSe).
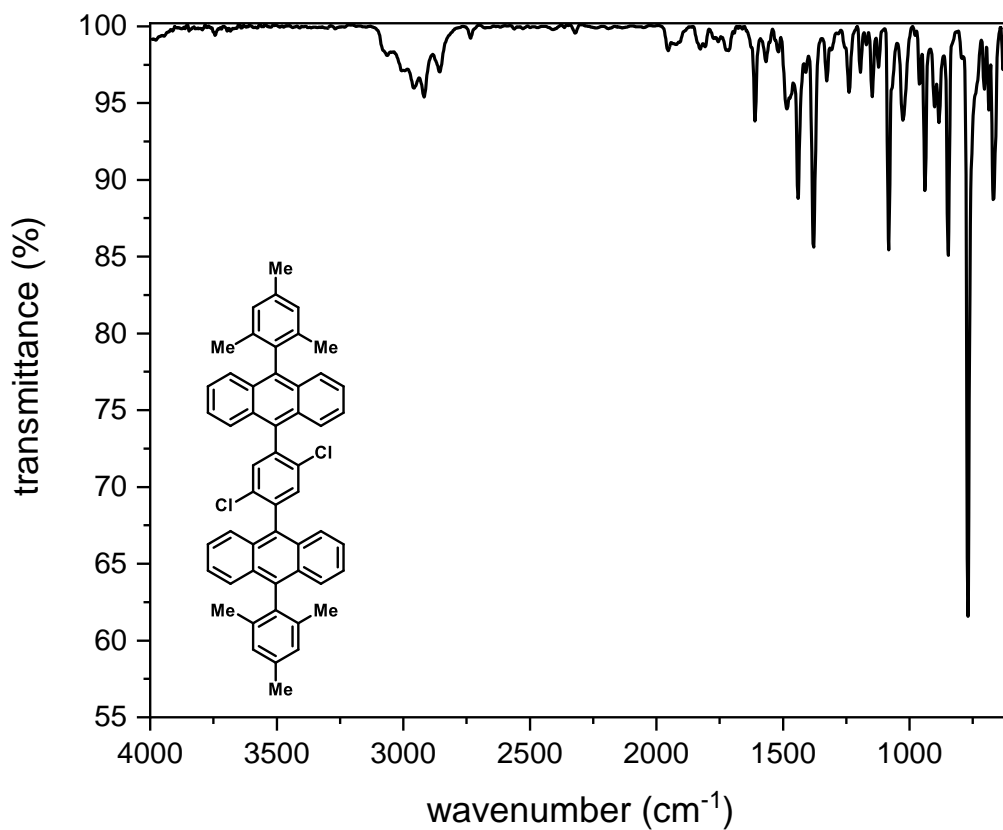
Figure S48: FT-IR spectrum of compound **7** (ATR, ZnSe).
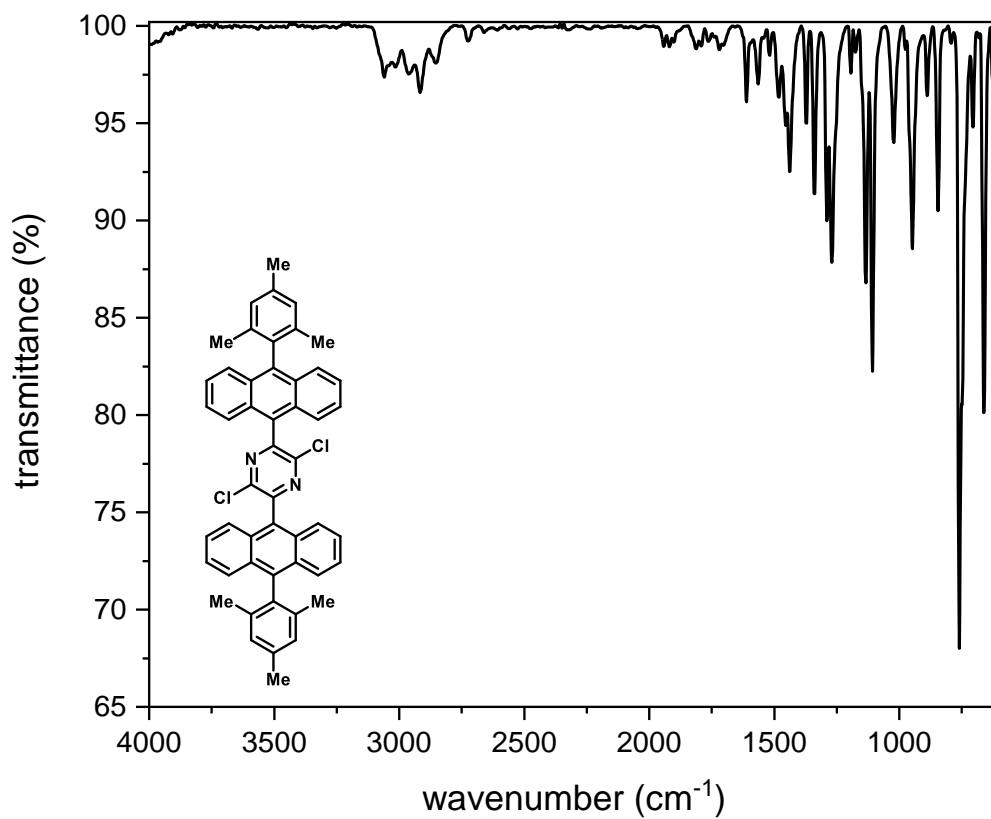
Figure S49: FT-IR spectrum of compound **8** (ATR, ZnSe).
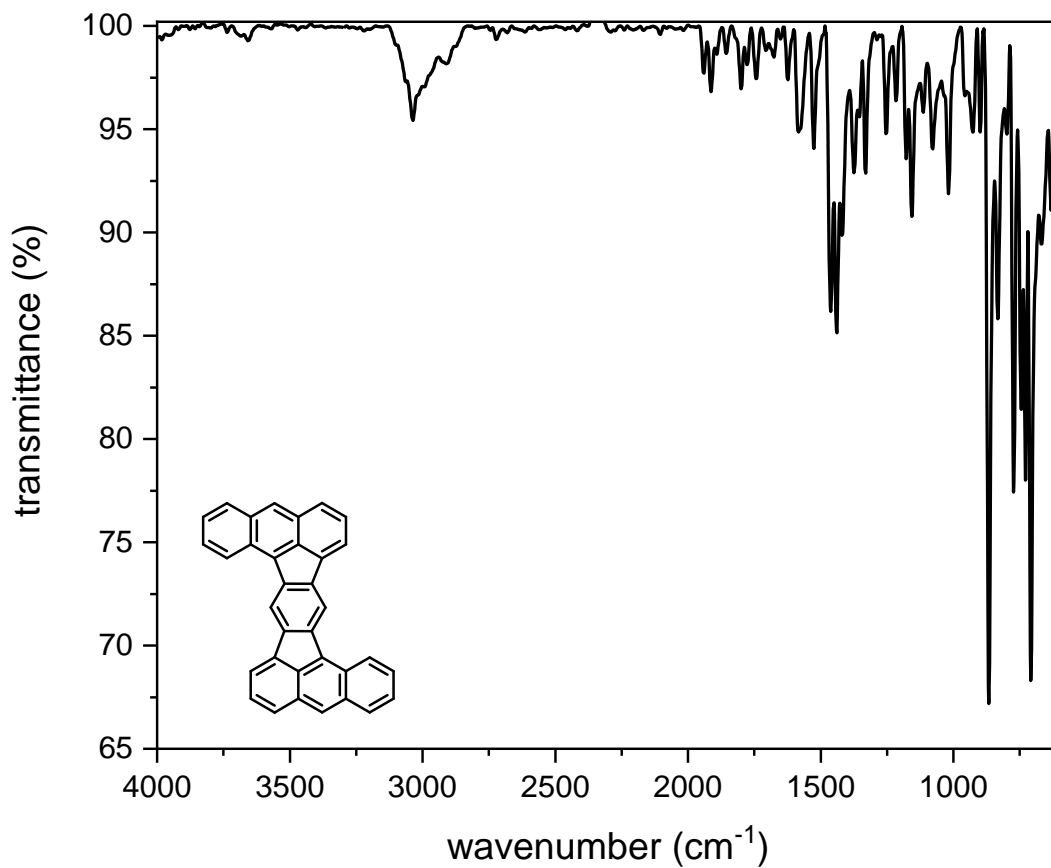
Figure S50: FT-IR spectrum of **DBAF** (ATR, ZnSe).
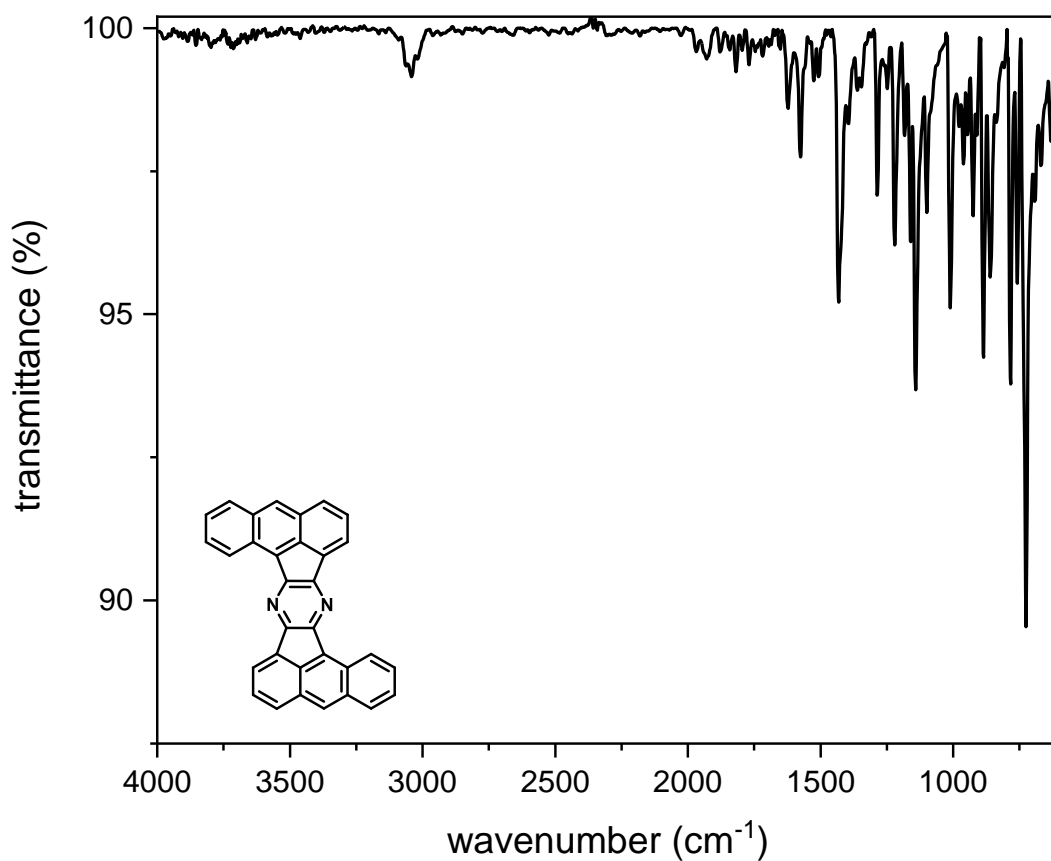
Figure S51: FT-IR spectrum of **DBAF-N$_2$** (ATR, ZnSe).
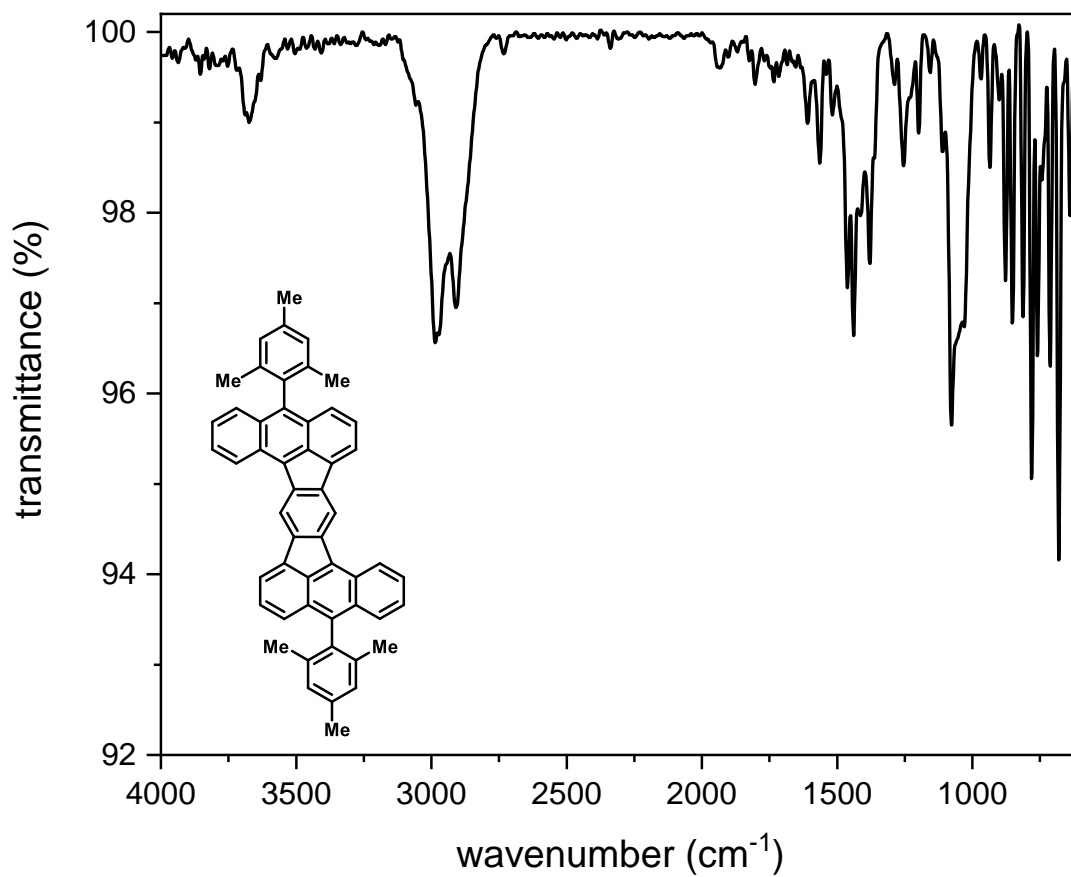
Figure S52: FT-IR spectrum of **mes-DBAF** (ATR, ZnSe).
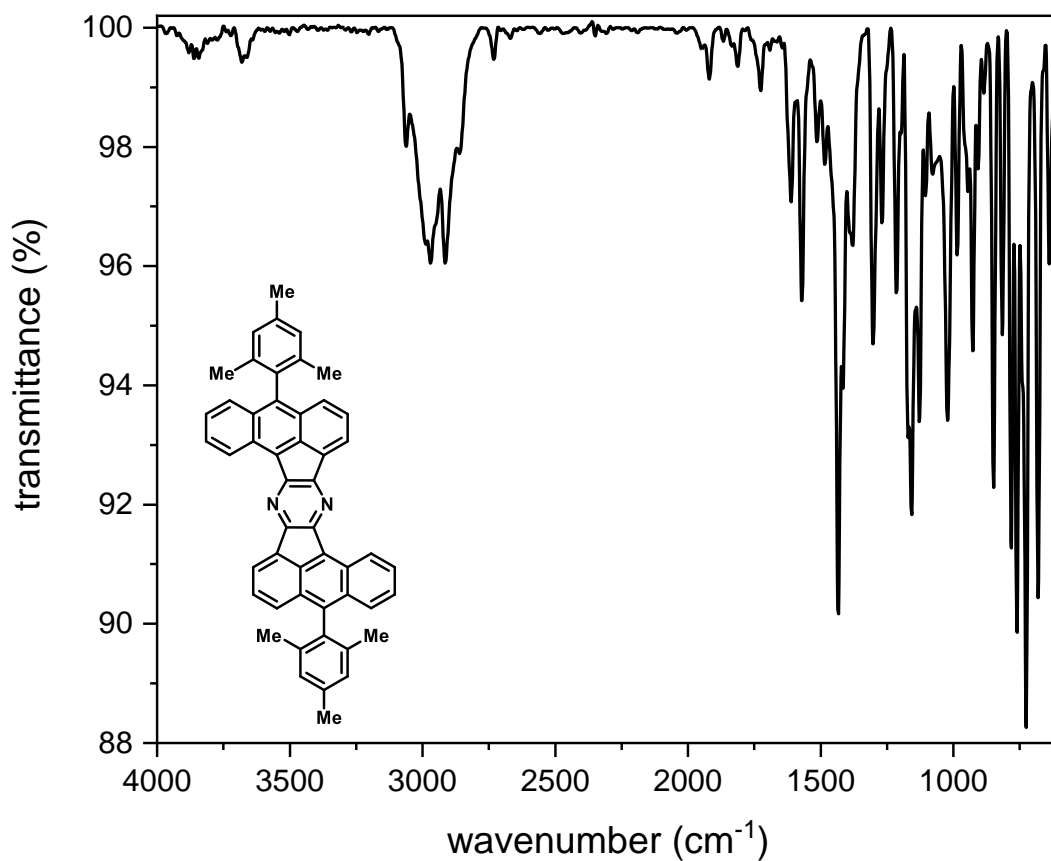
Figure S53: FT-IR spectrum of **mes-DBAF-N$_2$** (ATR, ZnSe).

5. Mass Spectrometry
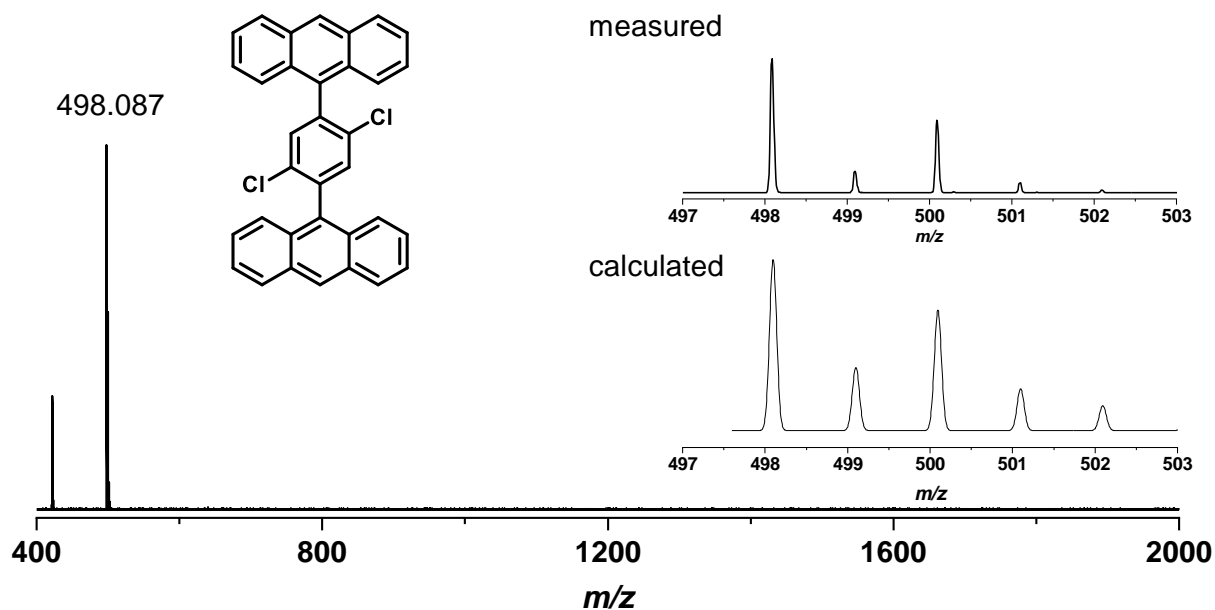
Figure S54: MALDI-TOF mass spectrum (pos. DCTB) of compound **5**.
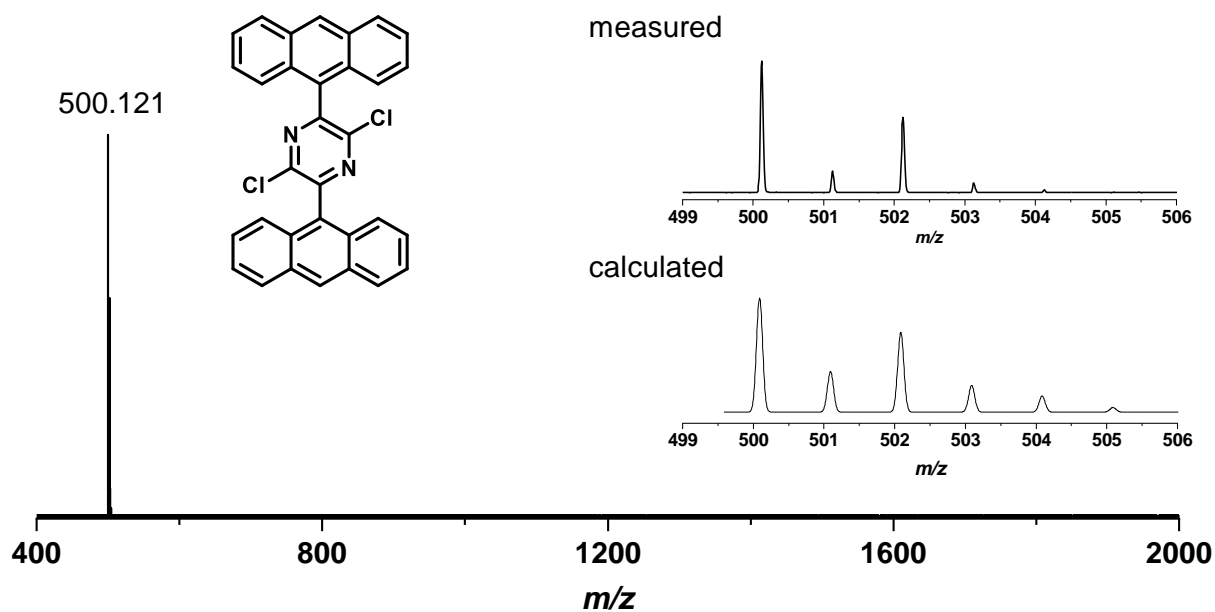
Figure S55: MALDI-TOF mass spectrum (pos. DCTB) of compound **6**.
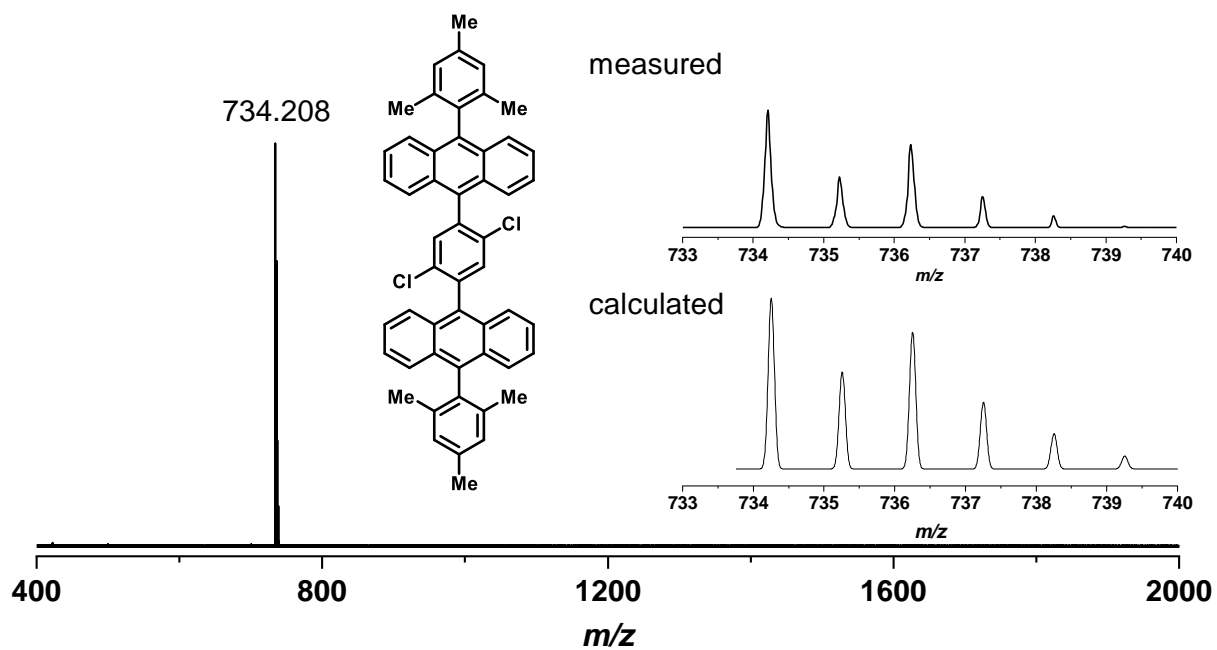
Figure S56: MALDI-TOF mass spectrum (pos. DCTB) of compound **7**.
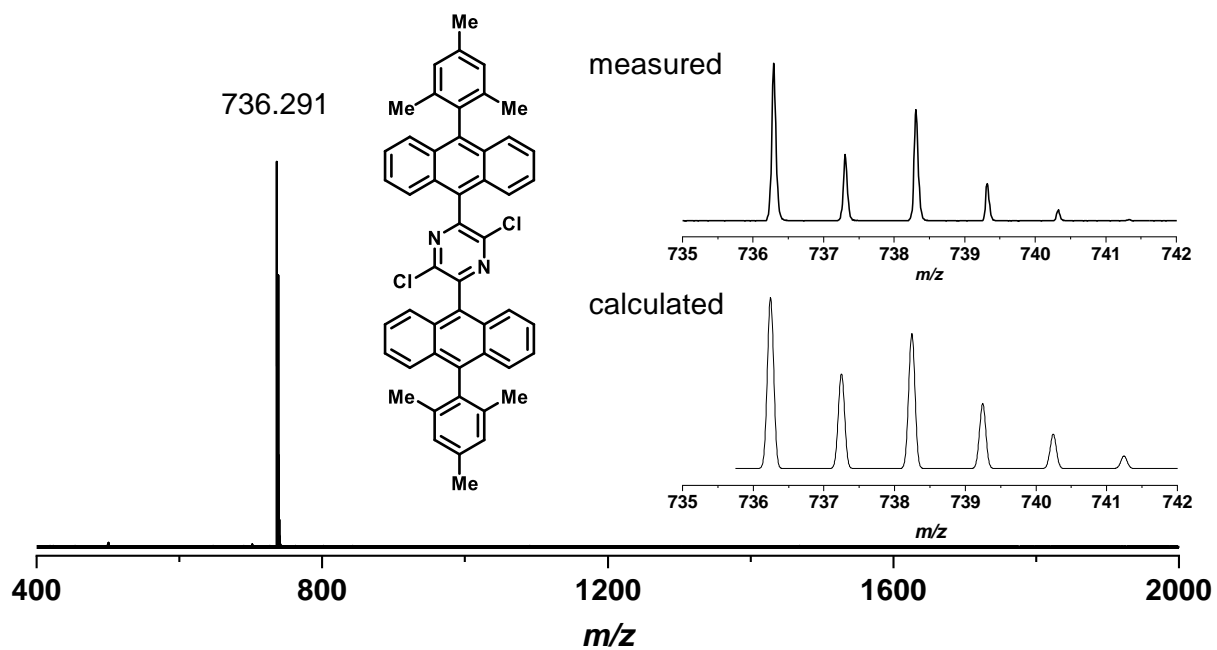
Figure S57: MALDI-TOF mass spectrum (pos. DCTB) of compound **8**.
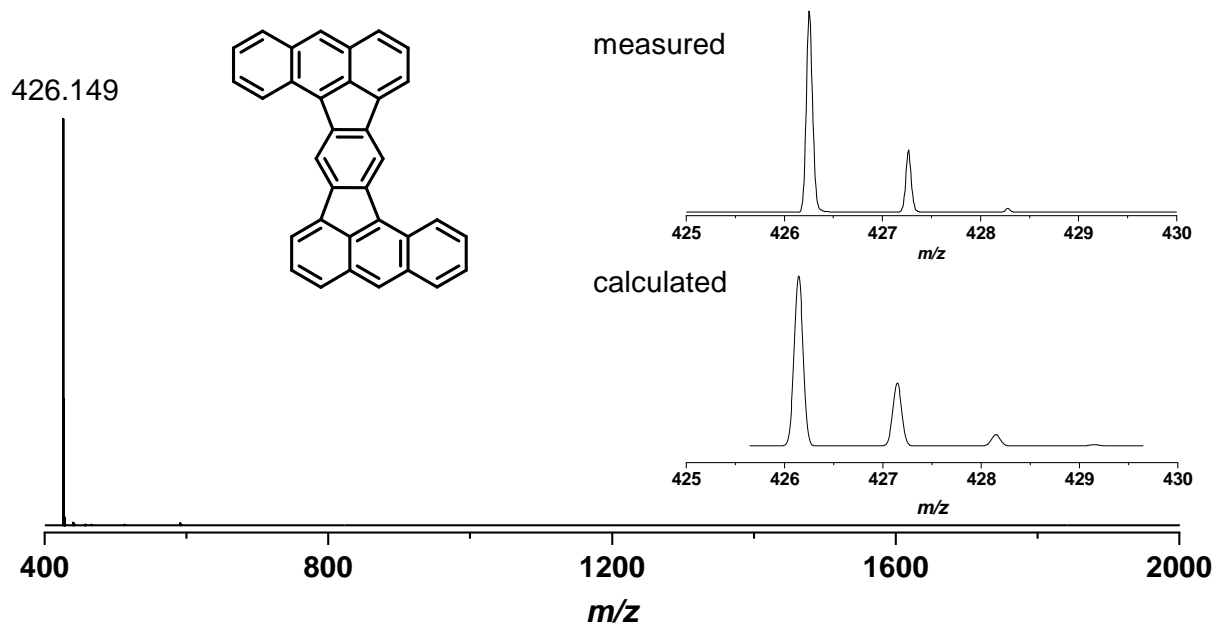
Figure S58: MALDI-TOF mass spectrum (pos. DCTB) of **DBAF**.
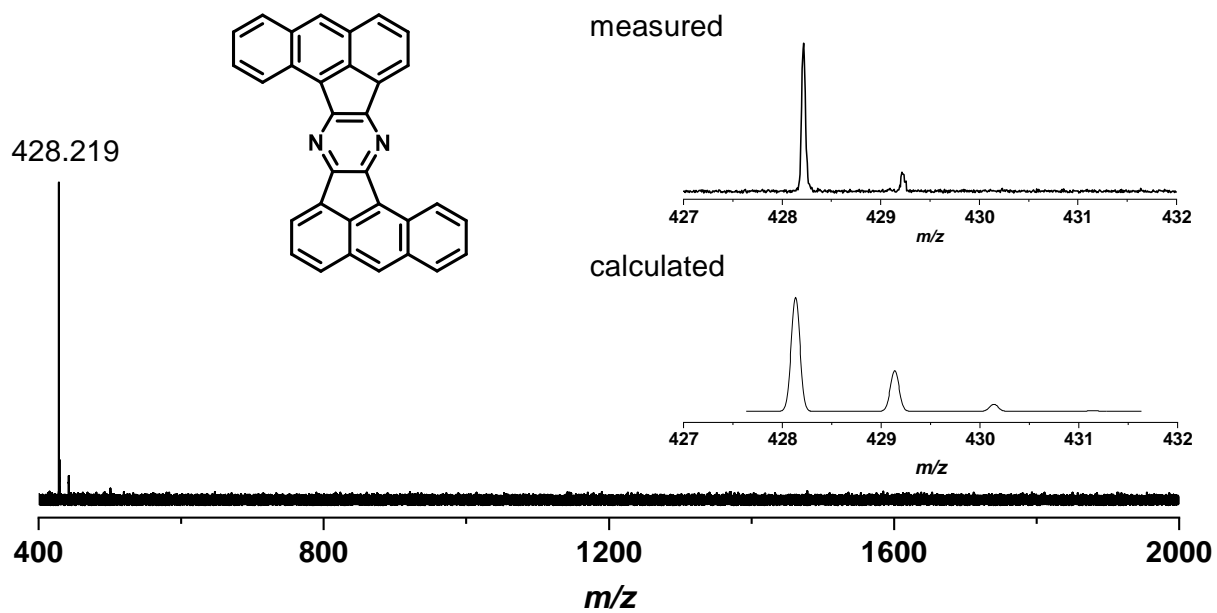
Figure S59: MALDI-TOF mass spectrum (pos. DCTB) of **DBAF-N$_2$**.
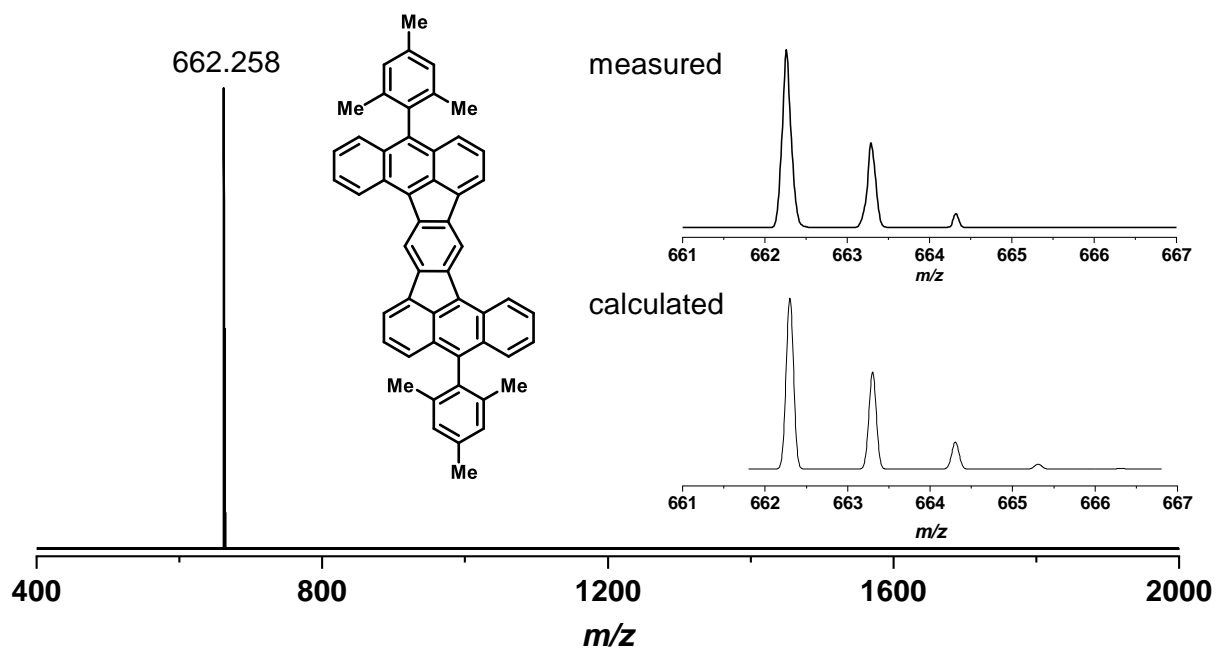
Figure S60: MALDI-TOF mass spectrum (pos. DCTB) of **mes-DBAF**.
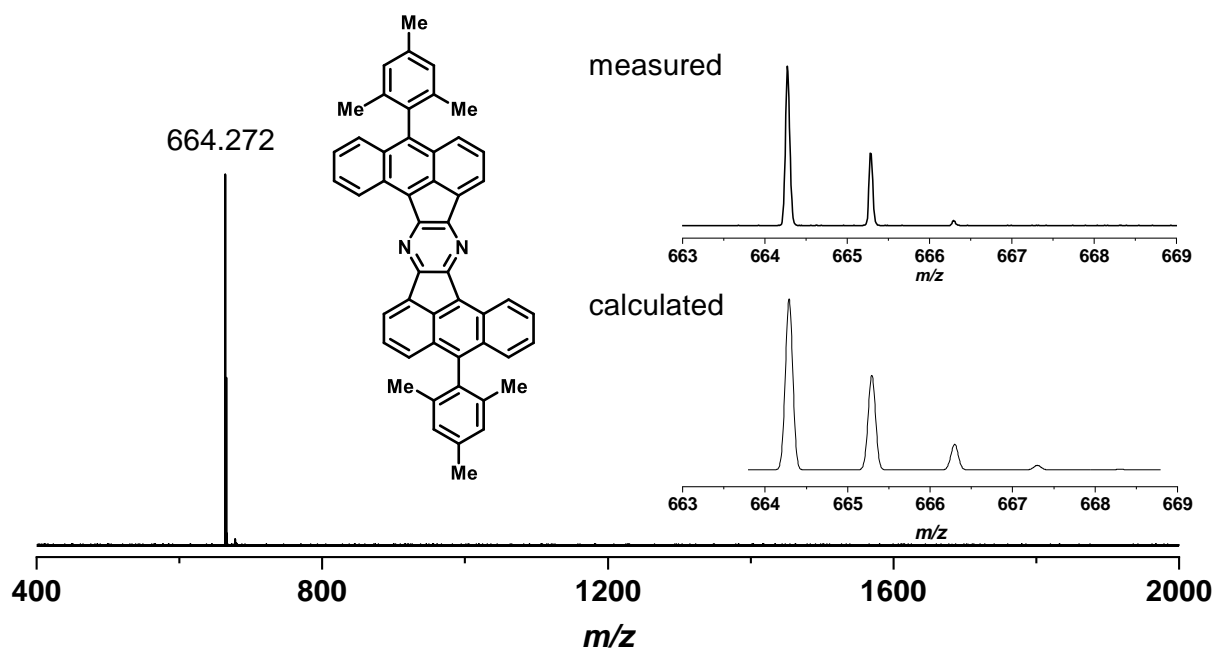
Figure S61: MALDI-TOF mass spectrum (pos. DCTB) of **mes-DBAF-N₂**.

6. UV/vis and Fluorescence Spectrometry
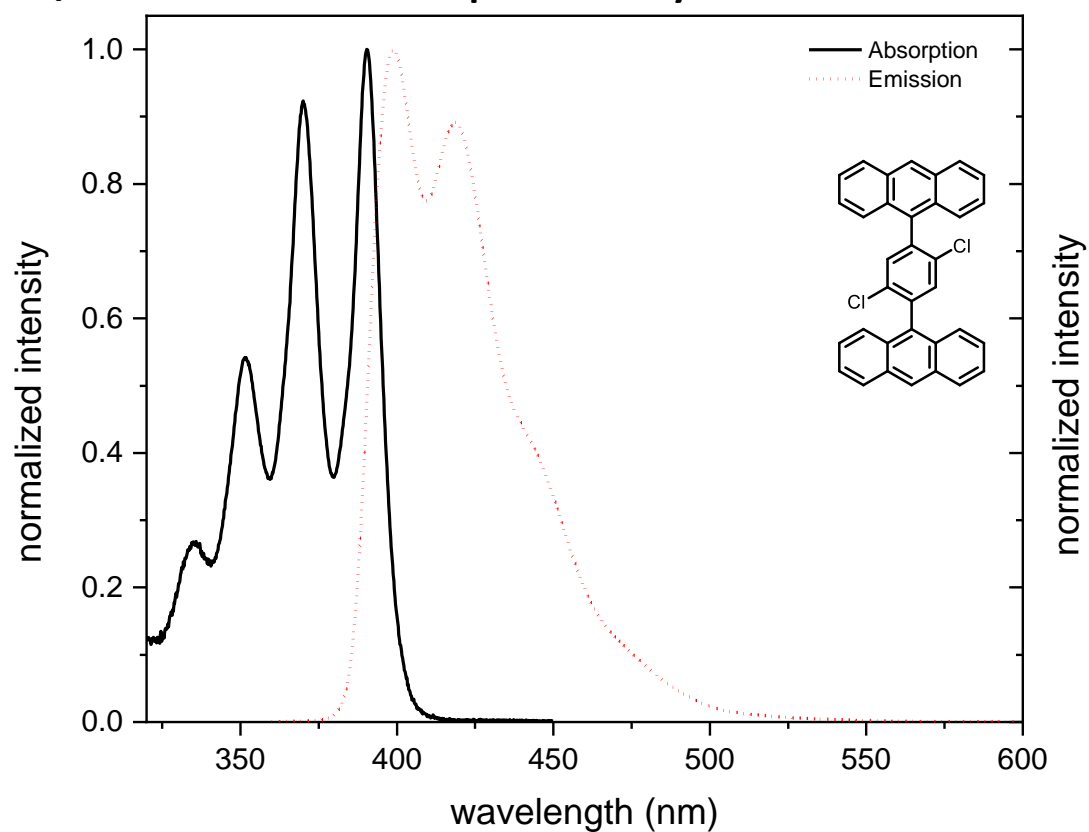
Figure S62: UV/vis (black) and emission (red) spectra of compound **5** measured in oDCB at room temperature.
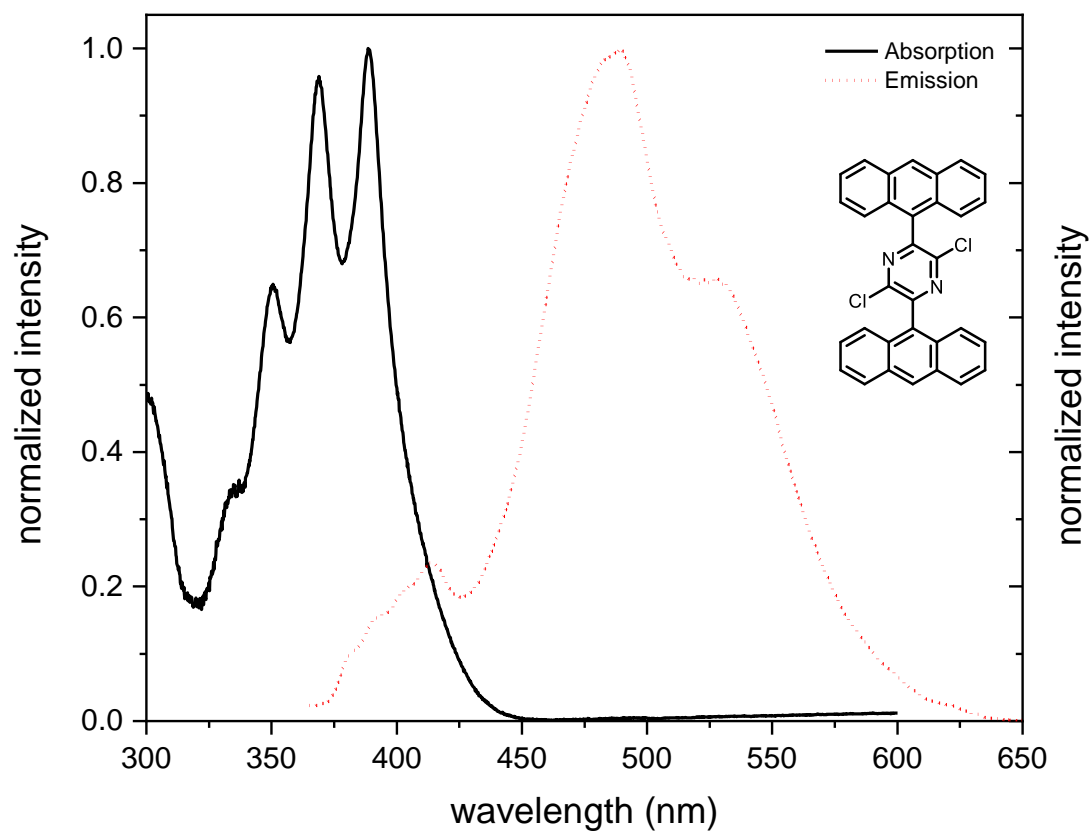
Figure S63: UV/vis (black) spectra of compound **6** measured in CH_2Cl_2 at room temperature.
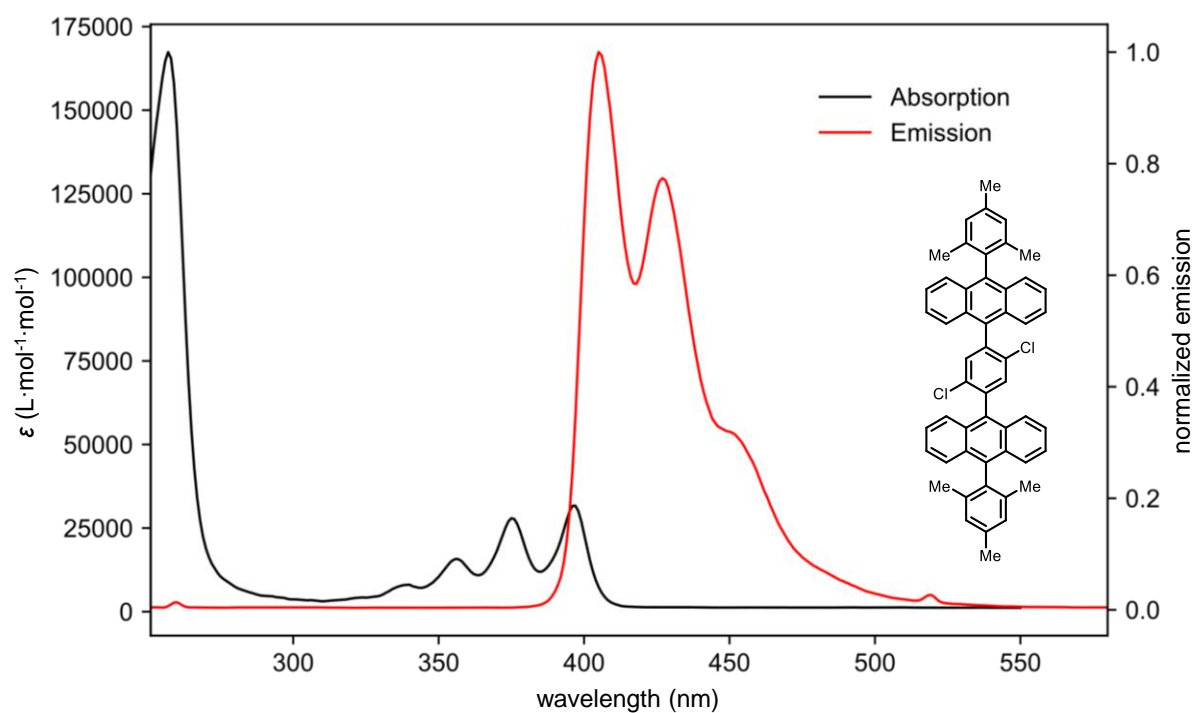
Figure S64: UV/vis (black) and emission (red) spectra of compound **7** measured in CH$_2$Cl$_2$ at room temperature.
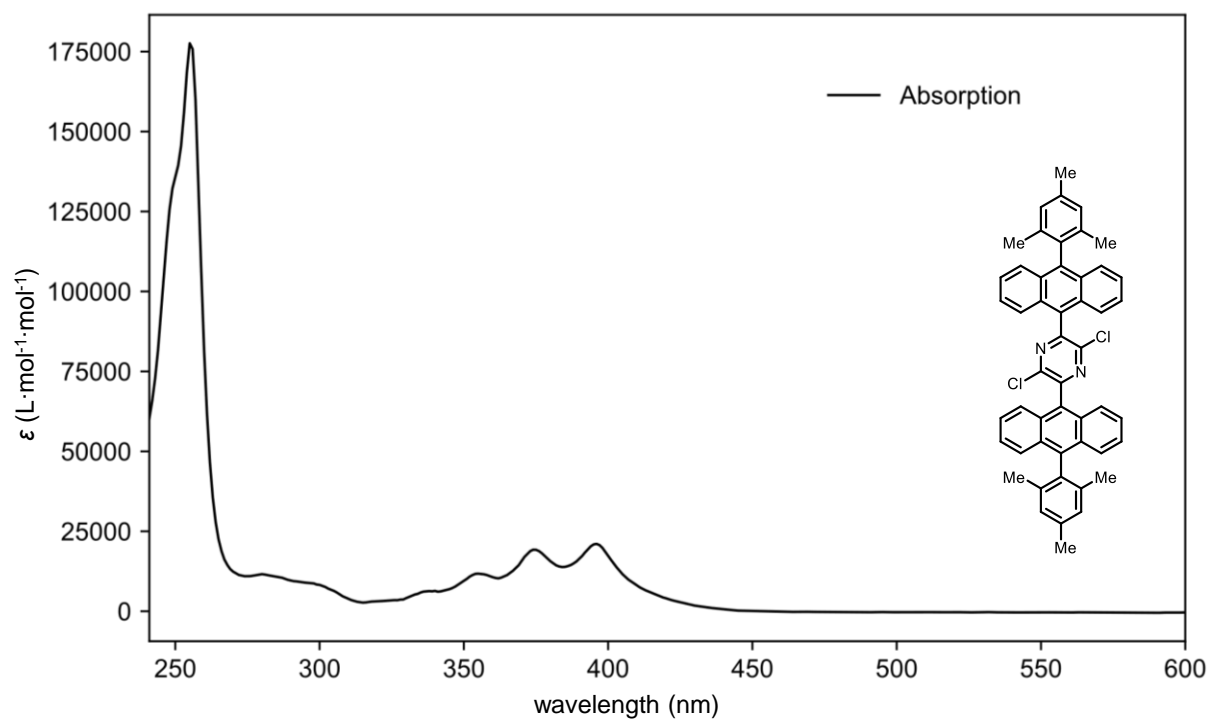
Figure S65: UV/vis (black) spectra of compound **8** measured in CH$_2$Cl$_2$ at room temperature.
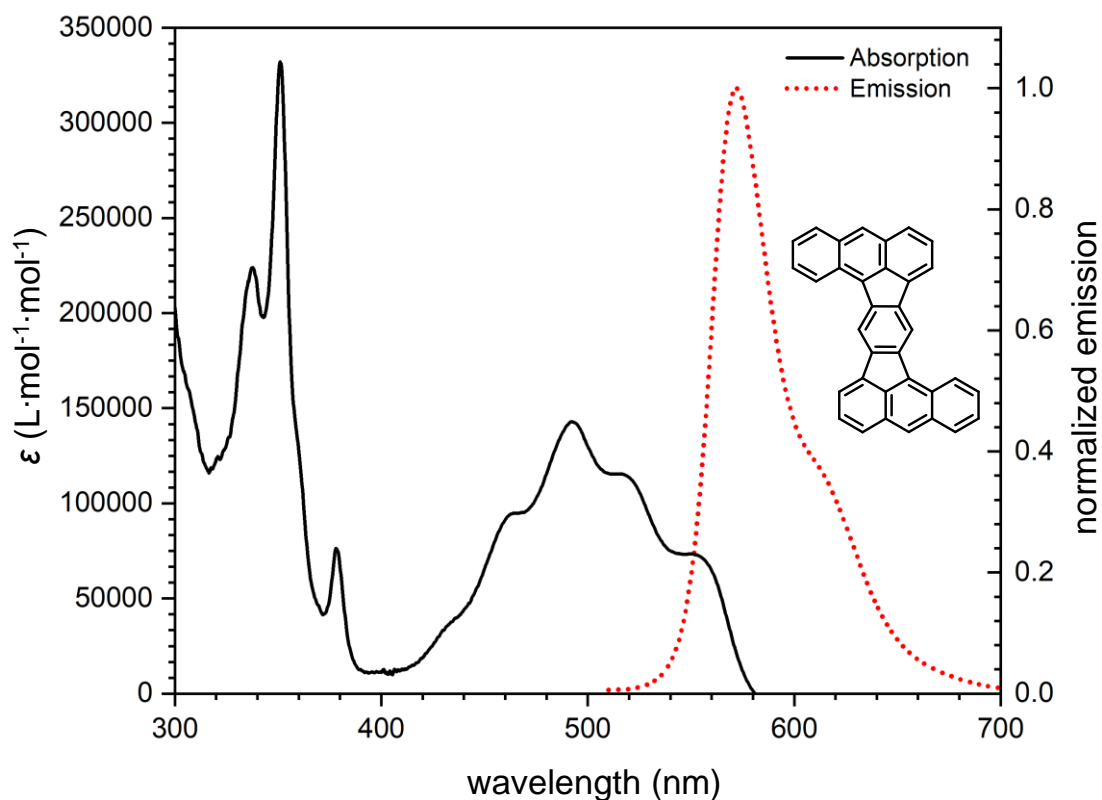
Figure S66: UV/vis (black) and emission (red, dotted) spectra of compound **DBAF** measured in oDCB at room temperature.
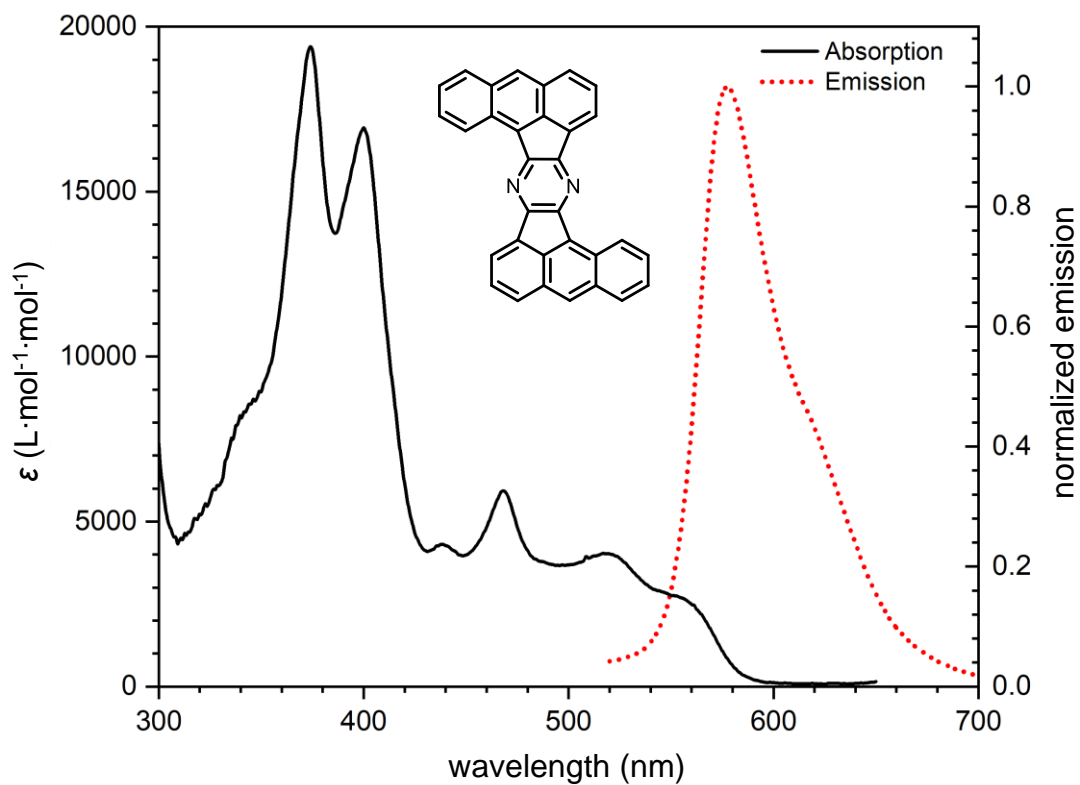
Figure S67: UV/vis (black) and emission (red, dotted) spectra of compound **DBAF-N₂** measured in oDCB at room temperature.
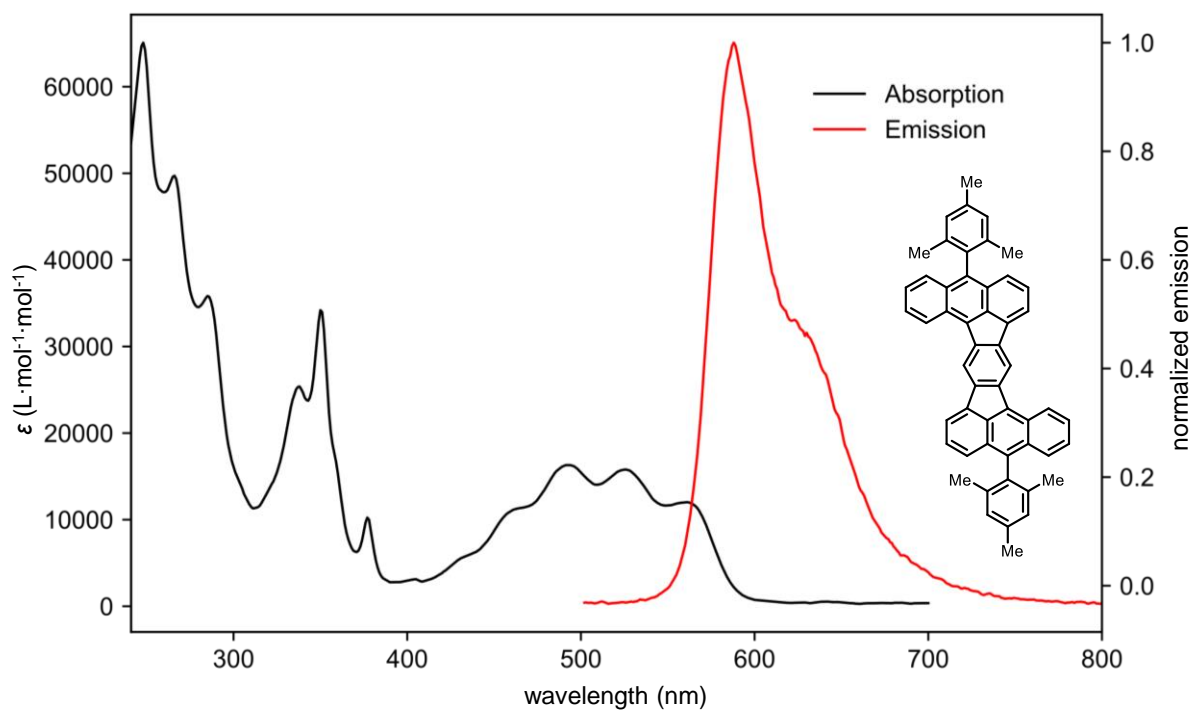
Figure S68: UV/vis (black) and emission (red) spectra of compound **mes-DBAF** measured in CH_2Cl_2 at room temperature.
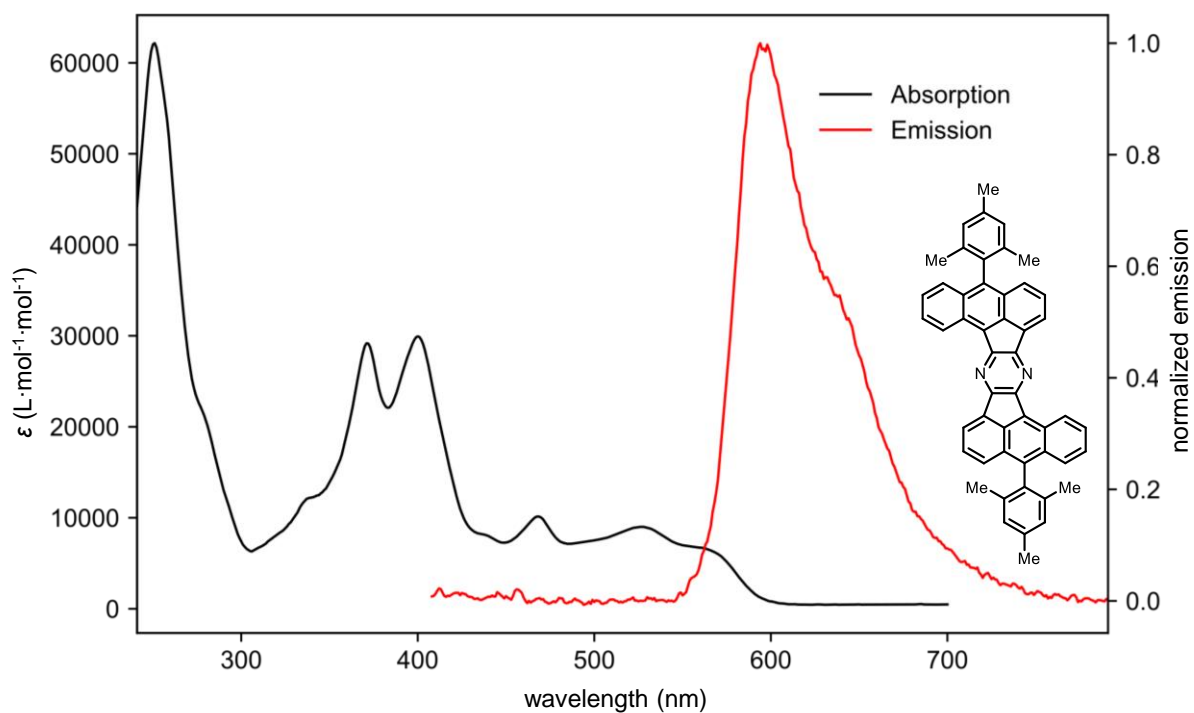
Figure S69: UV/vis (black) and emission (red) spectra of compound **mes-DBAF-N₂** measured in CH_2Cl_2 at room temperature.

7. Crystallographic Data

7.1. Compound 5

Crystals of **5** suitable for single crystal X-ray diffraction were obtained by thermal recrystallization from oDCB.
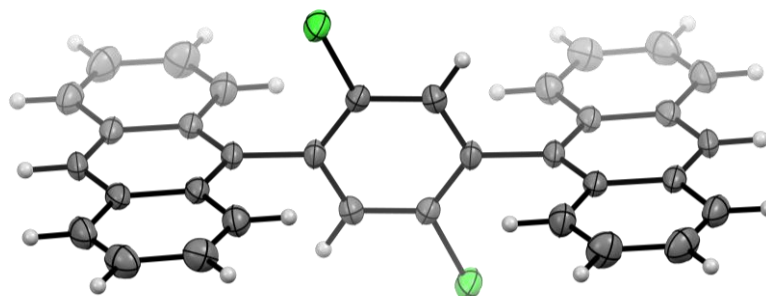
CCDC-number	2353527
Empirical formula	$C_{34}H_{20}Cl_2$
Formula weight	499.40
Temperature	200(2) K
Wavelength	0.71073 Å
Crystal system	monoclinic
Space group	$P2_1/n$
Z	2
Unit cell dimensions	a = 11.3543(14) Å α = 90 deg.
	b =7.0091(9) Å β =91.237(3) deg.
	c = 14.5933(18) Å γ = 90 deg.
Volume	1161.1(3) Å^3
Density (calculated)	1.43 g/cm^3
Absorption coefficient	0.30 mm^{-1}
Crystal shape	prism
Crystal size	0.155 x 0.120 x 0.038 mm^3
Crystal colour	yellow
Theta range for data collection	2.2 to 28.4 deg.
Index ranges	-15≤h≤14, -9≤k≤8, -19≤l≤19
Reflections collected	12148
Independent reflections	2667 (R(int) = 0.0539)
Observed reflections	1862 (I > 2σ(I))
Absorption correction	Semi-empirical from equivalents
Max. and min. transmission	0.96 and 0.92
Refinement method	Full-matrix least-squares on F^2
Data/restraints/parameters	2667 / 0 / 163
Goodness-of-fit on F^2	1.04
Final R indices (I>2sigma(I))	R1 = 0.047, wR2 = 0.092
Largest diff. peak and hole	0.30 and -0.26 eÅ^{-3}

7.2. Compound 6

Crystals of **6** suitable for single crystal X-ray diffraction were obtained by vapour phase diffusion of hexane in into a saturated chloroform solution of **6**.

CCDC-number	2353528
Empirical formula	$C_{32}H_{18}Cl_2N_2$
Formula weight	501.38
Temperature	200(2) K
Wavelength	1.54178 Å
Crystal system	monoclinic
Space group	$P2_1/n$
Z	2
Unit cell dimensions	a =8.4735(5) Å α = 90 deg.
	b =8.1885(3) Å β =94.305(5) deg.
	c = 16.7772(10) Å γ = 90 deg.
Volume	1160.81(11) Å^3
Density (calculated)	1.43 g/cm^3
Absorption coefficient	2.71 mm^{-1}
Crystal shape	plank
Crystal size	0.062 x 0.025 x 0.010 mm^3
Crystal colour	yellow
Theta range for data collection	6.0 to 68.9 deg.
Index ranges	-9≤h≤10, -5≤k≤9, -20≤l≤17
Reflections collected	11856
Independent reflections	2051 (R(int) = 0.1363)
Observed reflections	1259 (I > 2σ(I))
Absorption correction	Semi-empirical from equivalents
Max. and min. transmission	1.00 and 1.00
Refinement method	Full-matrix least-squares on F^2
Data/restraints/parameters	2051 / 157 / 173
Goodness-of-fit on F^2	1.01
Final R indices (I>2sigma(I))	R1 = 0.048, wR2 = 0.095
Largest diff. peak and hole	0.17 and -0.20 eÅ^{-3}

7.3.   Compound 7

Crystals of **7** suitable for single crystal X-ray diffraction were obtained by evaporation of a saturated CDCl$_3$ solution of **7**.
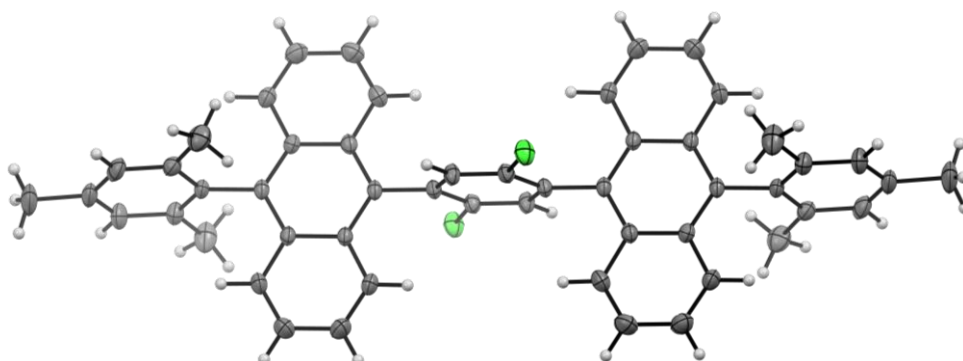
CCDC-number	2353529
Empirical formula	$C_{54}H_{42}Cl_8$
Formula weight	974.47
Temperature	200(2) K
Wavelength	0.71073 Å
Crystal system	triclinic
Space group	P $\overline{1}$
Z	1
Unit cell dimensions	a =8.4307(5) Å α =101.3934(17) deg.
	b =8.8836(5) Å β =100.9581(16) deg.
	c = 16.8457(10) Å γ = 103.7267(16) deg.
Volume	1163.68(12) Å^3
Density (calculated)	1.39 g/cm^3
Absorption coefficient	0.52 mm^{-1}
Crystal shape	plate
Crystal size	0.230 x 0.062 x 0.028 mm^3
Crystal colour	colourless
Theta range for data collection	2.4 to 31.1 deg.
Index ranges	-12≤h≤12, -12≤k≤12, -23≤l≤24
Reflections collected	25481
Independent reflections	7120 (R(int) = 0.0531)
Observed reflections	4428 (I > 2σ(I))
Absorption correction	Semi-empirical from equivalents
Max. and min. transmission	0.96 and 0.92
Refinement method	Full-matrix least-squares on F^2
Data/restraints/parameters	7120 / 0 / 283
Goodness-of-fit on F^2	1.03
Final R indices (I>2sigma(I))	R1 = 0.056, wR2 = 0.125
Largest diff. peak and hole	0.77 and -0.80 eÅ^{-3}

7.4.   Compound 8

Crystals of **8** suitable for single crystal X-ray diffraction were obtained by evaporation of a saturated CDCl₃ solution of **8**.

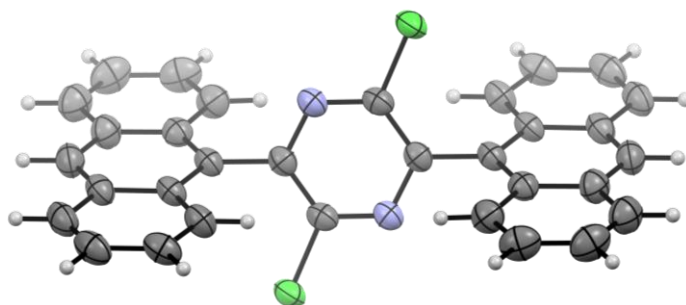| CCDC-number	2353530	
Empirical formula	$C_{52}H_{40}Cl_8N_2$	
Formula weight	976.46	
Temperature	200(2) K	
Wavelength	0.71073 Å	
Crystal system	triclinic	
Space group	P $\overline{1}$	
Z	1	
Unit cell dimensions	a =8.3208(10) Å	α = 102.240(3) deg.
	b =8.8810(11) Å	β =99.833(3) deg.
	c = 16.692(2) Å	γ =103.716(3) deg.
Volume	1138.9(2) Å³	
Density (calculated)	1.42 g/cm³	
Absorption coefficient	0.53 mm⁻¹	
Crystal shape	plate	
Crystal size	0.108 x 0.052 x 0.010 mm³	
Crystal colour	colourless	
Theta range for data collection	1.3 to 27.0 deg.	
Index ranges	-10≤h≤10, -11≤k≤11, -21≤l≤21	
Reflections collected	20391	
Independent reflections	4907 (R(int) = 0.0713)	
Observed reflections	3003 (I > 2σ(I))	
Absorption correction	Semi-empirical from equivalents	
Max. and min. transmission	0.96 and 0.92	
Refinement method	Full-matrix least-squares on F²	
Data/restraints/parameters	4907 / 0 / 283	
Goodness-of-fit on F²	1.02	
Final R indices (I>2sigma(I))	R1 = 0.054, wR2 = 0.105	
Largest diff. peak and hole	0.43 and -0.58 eÅ⁻³	

7.5. DBAF

Crystals of **DBAF** suitable for single crystal X-ray diffraction were obtained by thermal recrystallization from oDCB.

CCDC-number	2353531
Empirical formula	$C_{34}H_{18}$
Formula weight	426.48
Temperature	200(2) K
Wavelength	1.54178 Å
Crystal system	monoclinic
Space group	$P2_1/n$
Z	2
Unit cell dimensions	a = 7.8885(4) Å α = 90 deg.
	b = 12.3614(6) Å β = 98.462(4) deg.
	c = 10.6250(5) Å γ = 90 deg.
Volume	1024.80(9) Å³
Density (calculated)	1.38 g/cm³
Absorption coefficient	0.60 mm⁻¹
Crystal shape	prism
Crystal size	0.048 x 0.036 x 0.020 mm³
Crystal colour	red
Theta range for data collection	5.5 to 68.5 deg.
Index ranges	$-9 \leq h \leq 5$, $-12 \leq k \leq 14$, $-10 \leq l \leq 12$
Reflections collected	8017
Independent reflections	1856 (R(int) = 0.0414)
Observed reflections	1216 (I > 2σ(I))
Absorption correction	Semi-empirical from equivalents
Max. and min. transmission	0.99 and 0.91
Refinement method	Full-matrix least-squares on F^2
Data/restraints/parameters	1856 / 0 / 154
Goodness-of-fit on F^2	1.05
Final R indices (I>2sigma(I))	R1 = 0.050, wR2 = 0.114
Largest diff. peak and hole	0.19 and -0.17 eÅ⁻³

7.6. DBAF-N$_2$

Crystals of **DBAF-N$_2$** suitable for single crystal X-ray diffraction were obtained by sublimation at a kugelrohr apparatus (< 1·10^{-3} mbar, 300 °C).
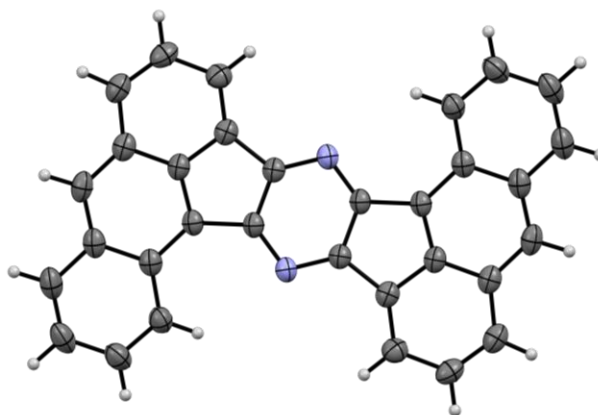
CCDC-number	2353532
Empirical formula	C$_{32}$H$_{16}$N$_2$
Formula weight	428.47
Temperature	200(2) K
Wavelength	0.71073 Å
Crystal system	monoclinic
Space group	P2$_1$/n
Z	2
Unit cell dimensions	a = 10.8037(16) Å α = 90 deg.
	b = 5.7081(9) Å β = 100.465(2) deg.
	c = 16.724(3) Å γ = 90 deg.
Volume	1014.2(3) Å^3
Density (calculated)	1.40 g/cm^3
Absorption coefficient	0.08 mm^{-1}
Crystal shape	irregular
Crystal size	0.267 x 0.043 x 0.037 mm^3
Crystal colour	orange
Theta range for data collection	2.5 to 28.4 deg.
Index ranges	-14≤h≤14, -7≤k≤7, -22≤l≤22
Reflections collected	10502
Independent reflections	2476 (R(int) = 0.0442)
Observed reflections	1697 (I > 2σ(I))
Absorption correction	Semi-empirical from equivalents
Max. and min. transmission	0.96 and 0.86
Refinement method	Full-matrix least-squares on F^2
Data/restraints/parameters	2476 / 0 / 154
Goodness-of-fit on F^2	1.07
Final R indices (I>2sigma(I))	R1 = 0.053, wR2 = 0.135
Largest diff. peak and hole	0.20 and -0.16 eÅ^{-3}

7.7. mes-DBAF
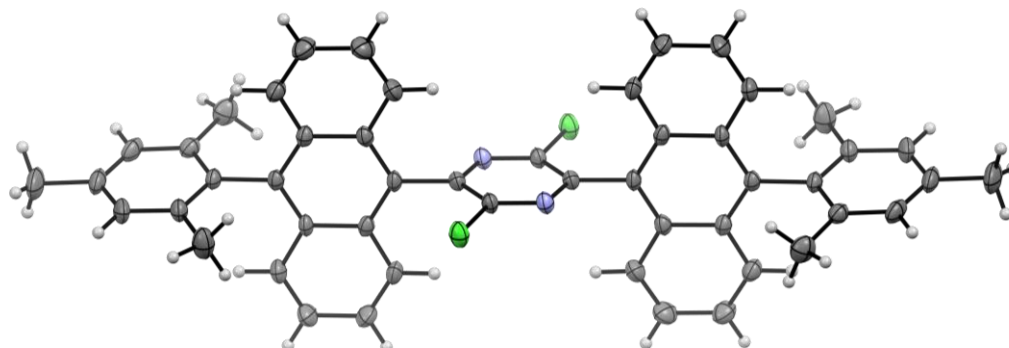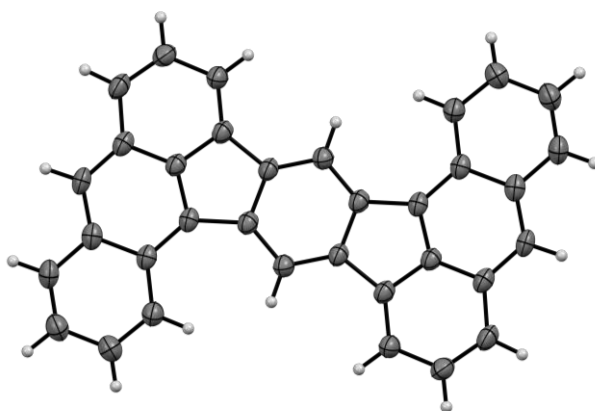
Crystals of **mes-DBAF** suitable for single crystal X-ray diffraction were obtained by evaporation of a saturated $CDCl_3$ solution of **mes-DBAF**.
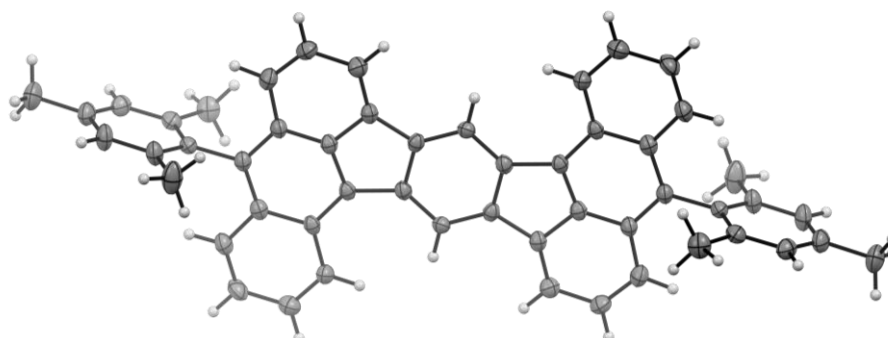
CCDC-number	2353533
Empirical formula	$C_{54}H_{40}Cl_6$
Formula weight	901.56
Temperature	200(2) K
Wavelength	0.71073 Å
Crystal system	monoclinic
Space group	$P2_1/n$
Z	2
Unit cell dimensions	a = 9.1598(15) Å α = 90 deg.
	b = 20.446(3) Å β = 104.773(4) deg.
	c = 12.1314(18) Å γ = 90 deg.
Volume	2196.9(6) Å^3
Density (calculated)	1.36 g/cm^3
Absorption coefficient	0.43 mm^{-1}
Crystal shape	column
Crystal size	0.143 x 0.031 x 0.015 mm^3
Crystal colour	red
Theta range for data collection	2.0 to 22.7 deg.
Index ranges	$-9 \leq h \leq 9$, $-22 \leq k \leq 22$, $-13 \leq l \leq 13$
Reflections collected	17113
Independent reflections	2952 (R(int) = 0.0946)
Observed reflections	1780 (I > 2σ(I))
Absorption correction	Semi-empirical from equivalents
Max. and min. transmission	0.96 and 0.88
Refinement method	Full-matrix least-squares on F^2
Data/restraints/parameters	2952 / 342 / 291
Goodness-of-fit on F^2	1.01
Final R indices (I>2sigma(I))	R1 = 0.058, wR2 = 0.128
Largest diff. peak and hole	0.42 and -0.43 eÅ^{-3}

7.8.   mes-DBAF-N$_2$

Crystals of **mes-DBAF-N$_2$** suitable for single crystal X-ray diffraction were obtained by vapor phase diffusion of hexane in into a saturated chloroform solution of **mes-DBAF-N$_2$**.
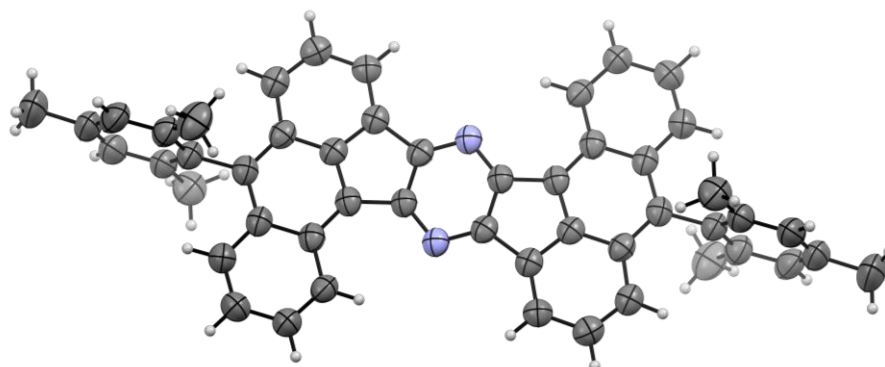
CCDC-number	2353534
Empirical formula	C$_{51}$H$_{37}$Cl$_3$N$_2$
Formula weight	784.17
Temperature	200(2) K
Wavelength	1.54178 Å
Crystal system	triclinic
Space group	P $\bar{1}$
Z	2
Unit cell dimensions	a =7.5160(3) Å α =94.217(3) deg.
	b = 15.7823(6) Å β =96.767(3) deg.
	c = 17.4357(6) Å γ =101.960(3) deg.
Volume	1998.99(13) Å^3
Density (calculated)	1.30 g/cm^3
Absorption coefficient	2.37 mm^{-1}
Crystal shape	needle
Crystal size	0.180 x 0.027 x 0.010 mm^3
Crystal colour	red
Theta range for data collection	2.6 to 68.6 deg.
Index ranges	-5≤h≤9, -18≤k≤15, -21≤l≤20
Reflections collected	29825
Independent reflections	7124 (R(int) = 0.0424)
Observed reflections	4564 (I > 2σ(I))
Absorption correction	Semi-empirical from equivalents
Max. and min. transmission	0.99 and 0.87
Refinement method	Full-matrix least-squares on F^2
Data/restraints/parameters	7124 / 138 / 548
Goodness-of-fit on F^2	1.04
Final R indices (I>2sigma(I))	R1 = 0.076, wR2 = 0.187
Largest diff. peak and hole	0.37 and -0.42 eÅ^{-3}

8. Quantum Chemical Calculation

8.1. Frontier Molecular Orbitals

Calculations were performed using Gaussian 16, manipulation of obtained results were performed using Gaussview.[S11] The Frontier Molecular Orbitals Calculation of frontier molecular orbitals was achieved by generating a formatted checkpoint file after single point calculation using DFT-methods (u-B3LYP/6-31G(d,p))[S12-22] with an isosurface value of 0.02.

8.2. Transfer Integrals and Theoretical Mobilities

Fragment based non-adiabatic molecular dynamics (NAMD) simulations were performed using the fewest switches surface hopping algorithm (FSSH), implemented in a local version of GROMACS 4.6[S23] The methodology details are described in Ref. S24. This computational approach is based on the partitioning of the crystal super-cell into classical and quantum regions. The propagation of the excess charge carrier is restricted in the quantum chemical (QM) region, while the remainder of the crystal is treated with molecular mechanics (MM). The wave function of the charge carrier, ψ, is expressed as the linear combination of frontier orbitals of the fragments (HOMO/LUMO), ϕ_m, in the QM zone.

$$\psi = \sum_A \sum_{m \in A} a_m |\phi_m >$$

Fragmentation of the QM zone makes it possible to use a coarse-grained model Hamiltonian matrix where the diagonal elements represent site energies (HOMO/LUMO energies of the fragments) and the off-diagonal elements are couplings between two fragments J. The corresponding Hamiltonian matrix elements, $H_{mn} = <\phi_m | H | \phi_n>$, are computed using the nonself-consistent variant of the density functional tight-binding method (DFTB) as discussed in ref S25. Moreover, it is found that using an uniform scaling factor results in an accuracy comparable to high-level ab initio methods.[26] Therefore, in the present work, the DFTB electronic couplings, J, were scaled by a factor of 1.54 and 1.79 for hole and electron transport, respectively. Charge carriers wave function is propagated using time dependent Schrödinger equation (TDSE) coupled to the classical motion of the nuclei. Quantum forces cause a relaxation in the geometry of the molecular fragment, resulting in a modification of the site energy H_{mm}. In Marcus theory, this relaxation is characterized by the inner-sphere relaxation parameter λ. When one site is charged, the site energy decreases by λ. To account

for the charge relaxation effect on the electronic system, the on-site energy Hmm is reduced by a pre-calculated parameter, weighted by the charge occupation on site m. We refer to this method as implicit relaxation (IR). Details of this approach outlined in ref S23. The charge carrier mobility is calculated using Einstein Smoluchowski relation $\mu = eD/k_BT$ where e is the elementary charge, k_B is the Boltzmann factor and T is the absolute temperature. The diffusion coefficient, D, is calculated by

$$D = \frac{1}{2n} \lim_{t \to \infty} \frac{dMSD(t)}{dt}$$

where n is the dimensionality (n = 1 for 1D system) and mean square displacement of the charge carrier, MSD, is defined as

$$MSD(t) = \frac{1}{N_{\text{traj}}} \sum_{l}^{N_{\text{traj}}} \sum_{A} (x_A(t)^{(l)} - x_0^l)^2 P(t)^{(l)}(t)$$

where $x_A(t)^l$ and $P(t)^{(l)}$ are the center of mass of molecule A and corresponding charge population along the trajectory l, respectively. $x_0^{\wedge}\ l$ is the center of charge at $t = 0$.

It has been demonstrated that this method can accurately reproduce experimental results.15 Below, we detail the NAMD simulations. [23]

Super-cell structures of the investigated molecular crystals were generated based on crystallographic data from experiments, expanded in various directions to make the simulation boxes. The resulting structures were equilibrated using an NVT ensemble at 300 K with a Nose-Hoover thermostat[S27] for 1 ns and a time step of 2 fs. The General Amber Force Field (GAFF)[S28] was employed for these simulations. Atomic partial charges were obtained through restrained electrostatic potential (RESP)[S29] fitting, calculated by the Hartree-Fock (HF) method with a 6-311G(p,d) basis set.[S30] The molecular geometries were optimized using Density Functional Theory (DFT) with the B3LYP functional and the 6-311G(p,d) level of theory, implemented in Gaussian 16.[S31]

Subsequently, a production MD simulation was conducted for 1 ns with a 2 fs time step, sampling initial super-cell coordinates every 100 fs for the FSSH simulation. For each initial super-cell geometry, NAMD simulations were conducted for 1 ps with a 0.1 fs time step.[24-26]

The reorganization energy of the molecules was computed using DFT with B3LYP and ωB97xd functionals and a 6-31G(d,p) basis set, utilizing Gaussian 16 software.[S31] Average hole/electron transfer integrals <J> were calculated for 100,000 structures sampled from the NAMD simulation of the corresponding crystal over 100 ps with a 1 fs time step. In this simulation, a dimer in the relevant direction was included in the QM zone, with the charge localized on one of the monomers. The transfer integral calculations are detailed in Ref. S25 and S26. Table S1 shows the reorganization energies(RE) together with average coupling values <J>.

Table S1: Reorganization Energy (RE) and Average Hole/Electron coupling <J> of the π stack directions. All the values are in meV.

	Hole			Electron		
	RE (B3LYP)	RE(ωB97xd)	<J>	RE (B3LYP)	RE(ωB97xd)	<J>
DBAF	153	336	20±14	117	214	-46±30
DBAF-N$_2$	167	370	-70±24	105	182	54±18
mes-DBAF	161	346	3±2	123	222	11±5
mes-DBAF-N$_2$	176	381	-19±11	110	245	21±13

NAMD simulations of hole/electron transfer were conducted for the one-dimensional QM zone in crystals with the highest transfer integral values. For **DBAF**: 50 and **DBAF-N$_2$**: 85, **mes-DBAF**: 15, **mes-DBAF-N$_2$**: 35 molecules (from the corresponding π-stacked packing direction) were selected to constitute the QM zone. Table S2 shows the calculated mobility with different reorganization energies.

Table S2: Hole and electron mobility. All the values are in cm^2/Vs.

	Hole		Electron	
	FSSH-IR (B3LYP)	FSSH-IR (ωB97xd)	FSSH-IR (B3LYP)	FSSH-IR (ωB97xd)
DBAF	0.31	0.00	6.70	1.87
DBAF-N$_2$	14.41	0.58	23.65	5.46
mes-DBAF	0.00	0.00	0.53	0.00
mes-DBAF-N$_2$	0.07	0.00	0.95	0.00

9. Device Fabrication and Analysis

Organic thin-film transistors (TFTs) were fabricated on 125-μm-thick flexible polyethylene naphthalate (PEN) substrates (Inabata Europe GmbH, Düsseldorf, Germany). The TFTs were fabricated either in the inverted staggered (bottom-gate, top-contact) or in the inverted coplanar (bottom-gate, bottom-contact) device architecture.[S31] To define the gate electrodes, aluminum (Al) with a thickness of 25 nm was deposited by thermal evaporation in vacuum through a polyimide shadow mask (CADiLAC Laser, Hilpoltstein, Germany).[S32] The film thickness of the vacuum-deposited films was monitored using a quartz crystal microbalance. The surface of the Al gate electrodes was briefly exposed to oxygen plasma and subsequently functionalized with a self-assembled monolayer (SAM) of n-tetradecylphosphonic acid (PCI Synthesis, Newburyport, MA, U.S.A.) to form a hybrid AlO_x/SAM gate dielectric with a thickness of 8 nm and a unit-area capacitance of 0.7 μF/cm^2.[S33] For the TFTs fabricated in the staggered (top-contact) device architecture, the next process step is the deposition of the organic-semiconductor layer, followed by the deposition of the source and drain contacts. The organic semiconductor (**DBAF** or **DBAF-N$_2$**) was deposited by thermal sublimation in vacuum through a polyimide shadow mask and has a nominal thickness of 30 nm. During the semiconductor deposition, the substrate was held at a temperature of 60 or 80 °C. To define the source and drain contacts, gold (Au) with a thickness of 30 nm was deposited by thermal evaporation in vacuum through a polyimide shadow mask. For the TFTs fabricated in the coplanar (bottom-contact) device architecture, the source and drain contacts were deposited prior to the organic semiconductor. In this case, the surface of the source and drain contacts was functionalized with a chemisorbed monolayer of pentafluorobenzenethiol (PFBT; TCI Deutschland GmbH, Eschborn, Germany) by immersing the substrates into a 10 mM ethanol solution of PFBT for 5 h, with the purpose of minimizing the contact resistance of the TFTs.[S31] In the last process step, the organic semiconductor was deposited by thermal sublimation in vacuum through a polyimide shadow mask, with a nominal thickness of 30 nm. The TFTs have a channel length of 30 μm and a channel width of 100 μm. The current-voltage characteristics of the TFTs were recorded using a manual probe station connected to an Agilent 4156C Semiconductor Parameter Analyzer. All measurements were performed in ambient air at room temperature. From the measured transfer characteristics, the effective charge-carrier mobilities were extracted using the equation $I_D = \mu_{eff} \cdot C_{diel} \cdot W \cdot (V_{GS} - V_{th})^2/(2 \cdot L)$, where I_D is the

drain current, μ_{eff} is the effective charge-carrier mobility, C_{diel} is the unit-area gate-dielectric capacitance (0.7 µF/cm^2), W is the channel width (100 µm), V_{GS} is the gate-source voltage, V_{th} is the threshold voltage, and L is the channel length (30 µm). [S34] The measured current-voltage characteristics of the TFTs and atomic force microscopy (AFM images of the vacuum-deposited organic-semiconductor films are shown in Figures S70-74.

Figure S70: Electrical characteristics of a **DBAF** TFT fabricated in the inverted staggered (bottom-gate, top-contact) device architecture, with the substrate held at a temperature of 60 ºC during the semiconductor deposition. The effective charge-carrier mobility is 0.3 cm^2/Vs

Figure S71: Electrical characteristics of a **DBAF** TFT fabricated in the inverted staggered (bottom-gate, top-contact) device architecture, with the substrate held at a temperature of 80 ºC during the semiconductor deposition. The effective charge-carrier mobility is 0.4 cm^2/Vs.

Figure S72: Electrical characteristics of a **DBAF** TFT fabricated in the inverted coplanar (bottom-gate, bottom-contact) device architecture, with the substrate held at a temperature of 60 ºC during the semiconductor deposition. The effective charge-carrier mobility is 0.3 cm2/Vs.
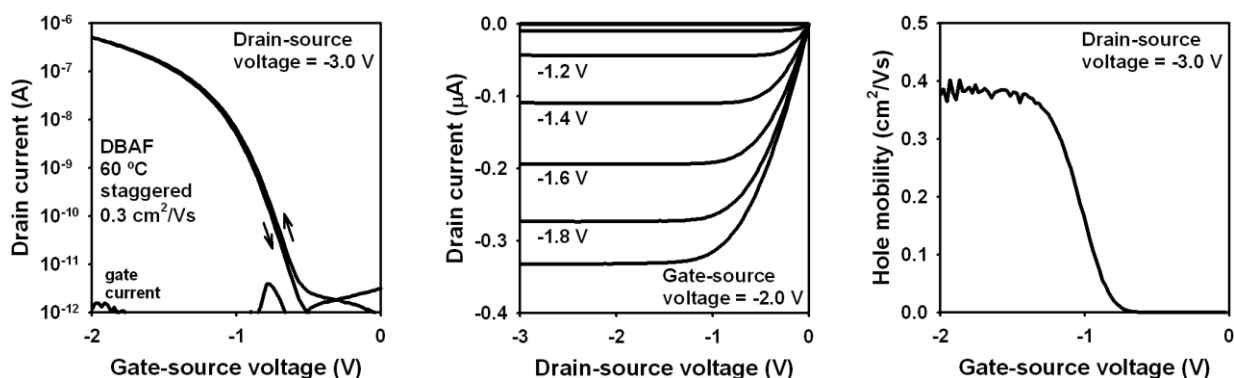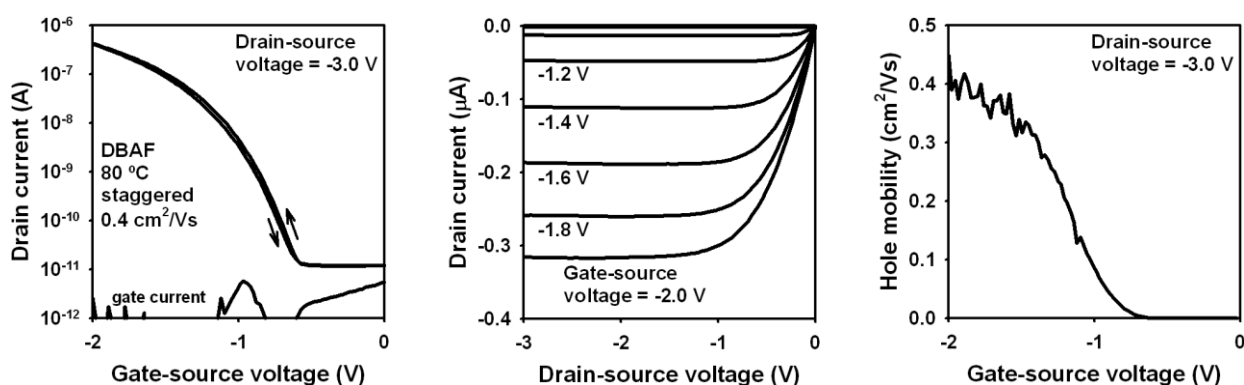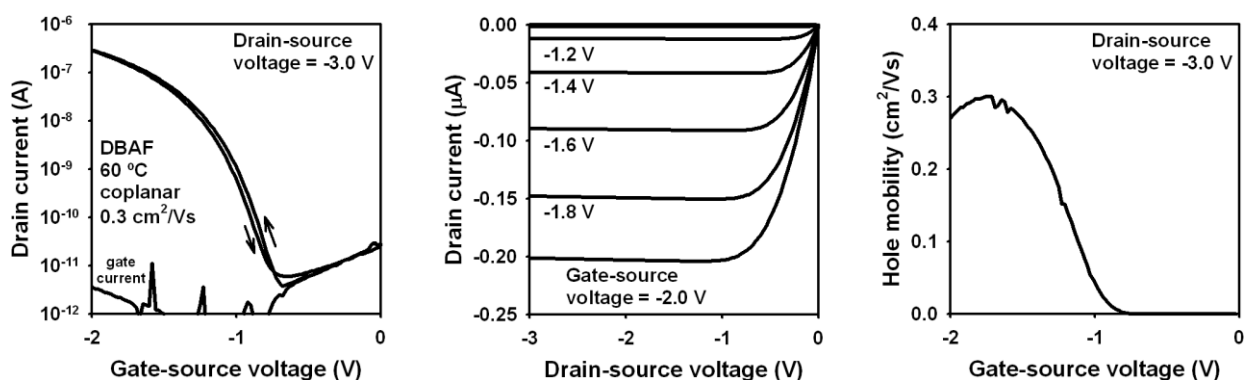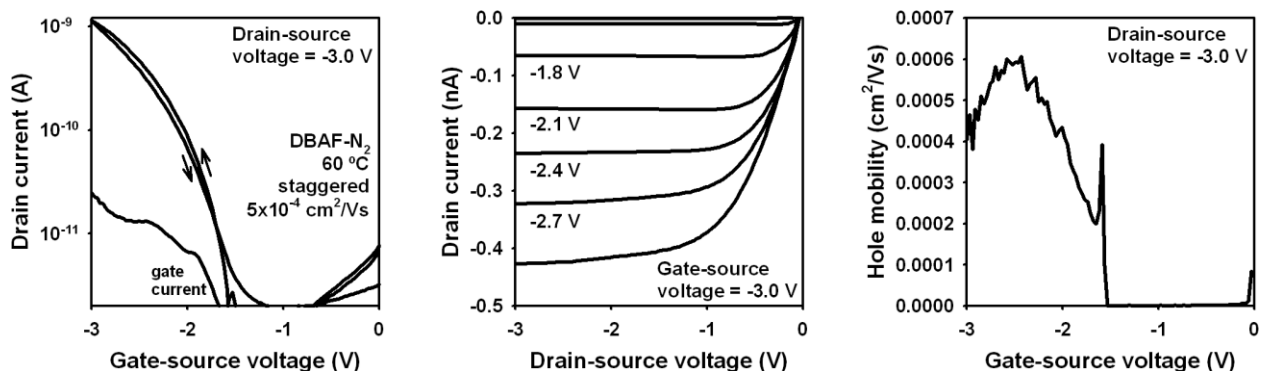
Figure S73: Electrical characteristics of a **DBAF-N₂** TFT fabricated in the inverted staggered (bottom-gate, top-contact) device architecture, with the substrate held at a temperature of 60 ºC during the semiconductor deposition. The effective charge-carrier mobility is 5×10^{-4} cm²/Vs.

Table S1: Summary of the effective charge-carrier mobilities extracted from the measured current-voltage characteristics of the TFTs.

semiconductor	device architecture	substrate temperature during semiconductor deposition	
		60 °C	80 °C
DBAF	staggered	0.3 cm²/Vs	0.4 cm²/Vs
	coplanar	not tested	0.3 cm²/Vs
DBAF-N₂	staggered	5×10^{-4} cm²/Vs	not tested
	coplanar	not tested	not tested

Figure S74: Atomic force microscopy (AFM) amplitude images of a **DBAF** film deposited with the substrate held at a temperature of 60 ºC (left), of a **DBAF** film deposited with the substrate held at a temperature of 80 ºC (center), and of a **DBAF-N₂** film deposited with the substrate held at a temperature of 60 ºC (right).

10. References

S1. H. W. H. Lai, Y. C. Teo and Y. Xia, Functionalized Rigid Ladder Polymers from Catalytic Arene-Norbornene Annulation Polymerization, *ACS Macro Lett.*, 2017, **6**, 1357-1361.

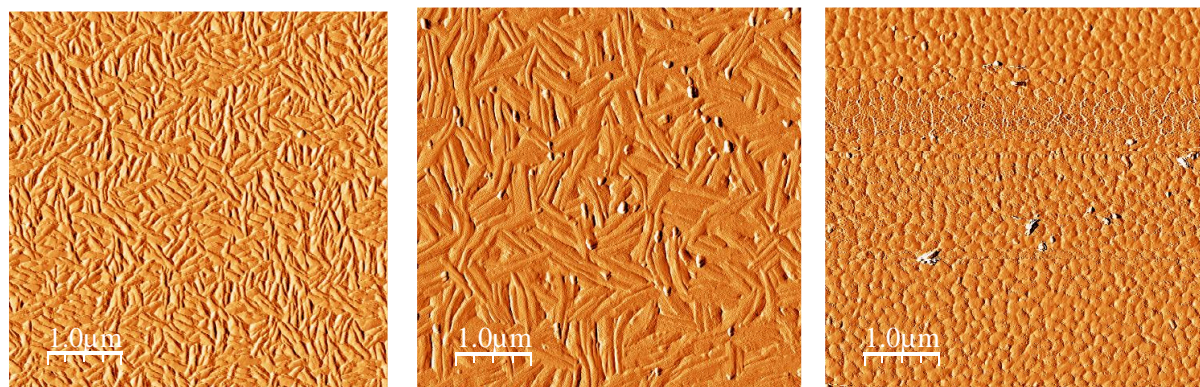S2. P. Meti, E.-S. Lee, J.-W. Yang and Y.-D. Gong, Regioselective synthesis of dipyrrolopyrazine (DPP) derivatives via metal free and metal catalyzed amination and investigation of their optical and thermal properties, *RSC Adv.*, 2017, **7**, 18120-18131.

S3. N. D. Shapiro, V. Rauniyar, G. L. Hamilton, J. Wu and F. D. Toste, Asymmetric additions to dienes catalysed by a dithiophosphoric acid, *Nature*, 2011, **470**, 245-249.

S4. C. H. E. Chow, H. Phan, X. Zhang and J. Wu, Sulfur-Doped (Dibenzo)heptazethrene and (Dibenzo)octazethrene Diradicaloids, *J. Org. Chem.*, 2020, **85**, 234-240.

S5. L. Valenta, M. Mayländer, P. Kappeler, O. Blacque, T. Šolomek, S. Richert and M. Juríček, Trimesityltriangulene: a persistent derivative of Clar's hydrocarbon, *Chem.Commun.* 2022, **58**, 3019-3022.

S6. C. Würth, M. Grabolle, J. Pauli, M. Spieles and U. Resch-Genger, Relative and absolute determination of fluorescence quantum yields of transparent samples, *Nat. Protocols*, 2013, **8**, 1535-1550.

S7. J. Koziskova, F. Hahn, J. Richter and J. Kožíšek, Comparison of different absorption corrections on the model structure of tetrakis(μ2-acetato)-diaqua-di-copper(II), *Acta Chim. Slov.* 2016, **9**, 136-140.

S8. G. Sheldrick, SHELXT - Integrated space-group and crystal-structure determination, *Acta Crystallograp. A*, 2015, **71**, 3-8.

S9. G. Sheldrick, Crystal structure refinement with SHELXL, *Acta Crystallograph. C*, 2015, **71**, 3-8.

S10. J. Lubben, C. M. Wandtke, C. B. Hubschle, M. Ruf, G. M. Sheldrick and B. Dittrich, Aspherical scattering factors for SHELXL - model, implementation and application, *Acta Crystallograph. A*, 2019, **75**, 50-62.

S11. M. J. Frisch, G. W. Trucks, H. B. Schlegel, G. E. Scuseria, M. A. Robb, J. R. Cheeseman, G. Scalmani, V. Barone, G. A. Petersson, H. Nakatsuji, X. Li, M. Caricato, A. V. Marenich, J. Bloino, B. G. Janesko, R. Gomperts, B. Mennucci, H. P. Hratchian, J. V. Ortiz, A. F. Izmaylov, J. L. Sonnenberg, Williams, F. Ding, F. Lipparini, F. Egidi, J. Goings, B. Peng, A. Petrone, T. Henderson, D. Ranasinghe, V. G. Zakrzewski, J. Gao, N. Rega, G. Zheng, W. Liang, M. Hada, M. Ehara, K. Toyota, R. Fukuda, J. Hasegawa, M. Ishida, T. Nakajima, Y. Honda, O. Kitao, H. Nakai, T. Vreven, K. Throssell, J. A. Montgomery Jr., J. E. Peralta, F. Ogliaro, M. J. Bearpark, J. J. Heyd, E. N. Brothers, K. N. Kudin, V. N. Staroverov, T. A. Keith, R. Kobayashi, J. Normand, K. Raghavachari, A. P. Rendell, J. C. Burant, S. S. Iyengar, J. Tomasi, M. Cossi, J. M. Millam, M. Klene, C. Adamo, R. Cammi, J. W. Ochterski, R. L. Martin, K. Morokuma, O. Farkas, J. B. Foresman and D. J. Fox, Gaussian 16, Revision B.01/C.01, Gaussian Inc., Wallingford, CT, 2016

S12. R. Ditchfield, W. J. Hehre and J. A. Pople, Self-Consistent Molecular-Orbital Methods. IX. An Extended Gaussian-Type Basis for Molecular-Orbital Studies of Organic Molecules, *J. Chem. Phys.*, 1971, **54**, 724-728.

S13.   W. J. Hehre, R. Ditchfield and J. A. Pople, Self-Consistent Molecular Orbital Methods. XII. Further Extensions of Gaussian-Type Basis Sets for Use in Molecular Orbital Studies of Organic Molecules, *J. Chem. Phys.*, 1972, **56**, 2257-2261.

S14.   P. C. Hariharan and J. A. Pople, The influence of polarization functions on molecular orbital hydrogenation energies, *Theor. Chim. Acta*, 1973, **28**, 213-222.

S15.   J. D. Dill and J. A. Pople, Self-consistent molecular orbital methods. XV. Extended Gaussian-type basis sets for lithium, beryllium, and boron, *J. Chem. Phys.*, 1975, **62**, 2921-2923.

S16.   J. S. Binkley and J. A. Pople, Self-consistent molecular orbital methods. XIX. Split-valence Gaussian-type basis sets for beryllium, *J. Chem. Phys.*, 1977, **66**, 879-880.

S17.   M. M. Francl, W. J. Pietro, W. J. Hehre, J. S. Binkley, M. S. Gordon, D. J. DeFrees and J. A. Pople, Self-consistent molecular orbital methods. XXIII. A polarization-type basis set for second-row elements, *J. Chem. Phys.*, 1982, **77**, 3654-3665.

S18.   M. S. Gordon, J. S. Binkley, J. A. Pople, W. J. Pietro and W. J. Hehre, Self-consistent molecular-orbital methods. 22. Small split-valence basis sets for second-row elements, *J. Am. Chem. Soc.*, 1982, **104**, 2797-2803.

S19.   S. H. Vosko, L. Wilk and M. Nusair, Accurate spin-dependent electron liquid correlation energies for local spin density calculations: a critical analysis, *Can. J. Phys.* 1980, **58**, 1200-1211.

S20.   C. Lee, W. Yang and R. G. Parr, Development of the Colle-Salvetti correlation-energy formula into a functional of the electron density, *Phys. Rev. B*, 1988, **37**, 785-789.

S21.   A. D. Becke, Density-functional thermochemistry. I. The effect of the exchange-only gradient correction, *J. Chem. Phys.* 1992, **96**, 2155-2160.

S22.   A. D. Becke, Density-functional thermochemistry. III. The role of exact exchange, *J. Chem. Phys.* 1993, **98**, 5648-5652.

S23.   S. Roosta, F. Ghalami, M. Elstner and W. Xie, Efficient Surface Hopping Approach for Modeling Charge Transport in Organic Semiconductors, *J. Chem. Theory Comput.* 2022, **18**, 1264-1274.

S24.   W. Xie, D. Holub, T. Kubař and M. Elstner, Performance of Mixed Quantum-Classical Approaches on Modeling the Crossover from Hopping to Bandlike Charge Transport in Organic Semiconductors, *J. Chem. Theory Comput.* 2020, **16**, 2071-2084.

S25.   A. Heck, J. J. Kranz, T. Kubař and M. Elstner, Multi-Scale Approach to Non-Adiabatic Charge Transport in High-Mobility Organic Semiconductors, *J. Chem. Theory Comput.* 2015, **11**, 5068-5082.

S26.   A. Kubas, F. Gajdos, A. Heck, H. Oberhofer, M. Elstner and J. Blumberger, Electronic couplings for molecular charge transfer: benchmarking CDFT, FODFT and FODFTB against high-level ab initio calculations. II, *Phys. Chem. Chem. Phys.* 2015, **17**, 14342-14354.

S27.   D. J. Evans and B. L. Holian, The Nose–Hoover thermostat, *J. Chem. Phys.* 1985, **83**, 4069-4074.

S28.   J. Wang, R. M. Wolf, J. W. Caldwell, P. A. Kollman and D. A. Case, Development and testing of a general amber force field, *J. Comput. Chem.* 2004, **25**, 1157-1174.

S29.   U. C. Singh and P. A. Kollman, An approach to computing electrostatic charges for molecules, *J. Comput. Chem.* 1984, **5**, 129-145.

S30.   G. A. Petersson, A. Bennett, T. G. Tensfeldt, M. A. Al-Laham, W. A. Shirley and J. Mantzaris, A complete basis set model chemistry. I. The total energies of closed-shell atoms and hydrides of the first-row elements, *J. Chem. Phys.* 1988, **89**, 2193-2218.

S31.   J. W. Borchert, B. Peng, F. Letzkus, J. N. Burghartz, P. K. L. Chan, K. Zojer, S. Ludwigs and H. Klauk, Small contact resistance and high-frequency operation of flexible low-voltage inverted coplanar organic transistors, *Nat. Commun.* 2019, **10**, 1119.

S32.   M. Geiger, R. Acharya, E. Reutter, T. Ferschke, U. Zschieschang, J. Weis, J. Pflaum, H. Klauk and R. T. Weitz, Effect of the Degree of the Gate-Dielectric Surface Roughness on the Performance of Bottom-Gate Organic Thin-Film Transistors, *Adv. Mater. Interfaces* 2020, **7**, 1902145.

S33.   M. Geiger, M. Hagel, T. Reindl, J. Weis, R. T. Weitz, H. Solodenko, G. Schmitz, U. Zschieschang, H. Klauk and R. Acharya, Optimizing the plasma oxidation of aluminum gate electrodes for ultrathin gate oxides in organic transistors, *Sci. Rep*, 2021, **11**, 6382.

S34.   H. Klauk, Organic thin-film transistors, *Chem. Soc. Rev.*, 2010, **39**, 2643-2666.